A DIGITAL-OPTICAL HYBRID CORRELATOR

R. A. Meyer, et al

Johns Hopkins University

Prepared for:

Naval Ordnance Systems Command

September 1972

TG 1193A
SEPTEMBER 1972
Copy No. 178

AD751695

Technical Memorandum

A DIGITAL-OPTICAL HYBRID CORRELATOR

R. A. MEYER
D. G. GRANT
J. L. QUEEN

THE JOHNS HOPKINS UNIVERSITY ■ APPLIED PHYSICS LABORATORY

DOCUMENT CONTROL DATA - R & D

Security classification of title, body of abstract and indexing annotation must be entered when the overall report is classified)

1. ORIGINATING ACTIVITY (Corporate author)	2a. REPORT SECURITY CLASSIFICATION
The Johns Hopkins University Applied Physics Lab.	Unclassified
8621 Georgia Avenue	2b. GROUP
Silver Spring, Maryland 20910	

3. REPORT TITLE

A Digital-Optical Hybrid Correlator

4. DESCRIPTIVE NOTES (Type of report and inclusive dates)

Technical Memorandum

5. AUTHOR(S) (First name, middle initial, last name)

R. A. Meyer, D. G. Grant, and J. L. Queen

6. REPORT DATE	7a. TOTAL NO. OF PAGES	7b. NO. OF REFS
September 1972	~~129~~ 130	10

8a. CONTRACT OR GRANT NO.	9a. ORIGINATOR'S REPORT NUMBER(S)
N00017-72-C-4401	
b. PROJECT NO.	TG 1193A
c.	9b. OTHER REPORT NO(S) (Any other numbers that may be assigned this report)
d.	

10. DISTRIBUTION STATEMENT

Approved for public release; distribution unlimited.

11. SUPPLEMENTARY NOTES	12. SPONSORING MILITARY ACTIVITY
Details of illustrations in this document may be better studied on microfiche.	Naval Ordnance Systems Command

13. ABSTRACT

A Digital-Optical Hybrid Correlator with the capability of processing pulse doppler and wideband radar signals has been developed based on the correlation properties of an optical phased array. This hybrid system retains the flexibility of digital technology for signal storage and registration, and the speed of coherent optical technology for performing the signal correlation. Two phased-array modulators have been developed. The Membrane Light Modulator is a mirror whose surface can be deflected in localized areas by electrostatic forces. The multichannel crystal modulator employs the electro-optic properties of lithium tantalate to achieve phase modulation. Both modulators have been used to perform optical phased-array beam steering. Pulse doppler and wideband radar signals have been processed by the hybrid correlator. The system's capability to perform two-dimensional correlation of frequency diversity radar waveforms has been demonstrated.

DD FORM 1473
1 NOV 65

14.	KEY WORDS					

Radar signal processing
Optics
Radar
Light modulators
Electro-optics
Phased array antennas
Correlation properties
Optical beam steering
Pulse doppler radar waveforms
Wideband radar waveforms

TG 1193A
SEPTEMBER 1972

Technical Memorandum

A DIGITAL-OPTICAL HYBRID CORRELATOR

R. A. MEYER
D. G. GRANT
J. L. QUEEN

iii

CONTENTS

Preceding page blank

ILLUSTRATIONS

1. INTRODUCTION

Many radar environments require the use of large
time-bandwidth transmissions. To process these wave-
forms by strictly electronic means is prohibitive because
of excessive cost and size. The Fourier transforming
properties of a coherent optical system and the success
of photographic-film optical processors in mapping opera-
tions have stimulated the search for optical modulators
that are suitable for the large time-bandwidth radar
signal-processing requirements of surface weapon con-
trol systems where processing delays must be held to the
order of milliseconds. Optical processors based on
ultrasonic modulators have been demonstrated, but are
restricted because of limitations in integration time (set
by propagation time in the acoustic media). Using the
correlation properties of an optical phased array, a hy-
brid digital-optical system has been designed which em-
ploys digital shift registers for the signal storage and
registration, and coherent optics for the two-dimensional
correlation. Such a system maintains the flexibility of
digital technology and the speed of optical technology.

Two high-speed phased array modulators have
been developed under the auspices of the Applied Physics
Laboratory for use with the Digital-Optical Hybrid Cor-
relator. The Membrane Light Modulator (developed by
the Perkin-Elmer Corporation, Norwalk, Connecticut)
is a mirror whose surface can be deflected in localized
areas by electrostatic forces. The multichannel crystal
modulator (fabricated by the Isomet Corporation,
Palisades Park, New Jersey) employs the electro-optic
properties of lithium tantalate to obtain phase modulation.
Both modulators have been used successfully in a one-
dimensional beam steering mode. One-dimensional cor-
relation of pulse doppler and linear-step FM waveforms
has been successfully achieved using the hybrid correlator

in an off-line window mode. Two-dimensional beam steering with the Membrane Light Modulator has been successfully performed demonstrating the capability of performing two-dimensional correlation with the hybrid correlator.

While the system has been operated in an off-line mode, it can be directly tied into a suitable radar to be used in the real-time window mode. The two electro-optic modulators and current digital input and memory devices are suitable for use in on-line processing of search mode wideband radar signals with no delay other than that required to accumulate the echoes. However, a suitable means is not currently available to output the answers form such a two-dimensional signal processor. Suitable devices do exist for one-dimensional signal processing (i.e., pulse-doppler, linear-step FM).

2. DESCRIPTION OF THE OPTICAL PHASE MODULATORS

The signal-processing capabilities of an optical phased array have stimulated the search for high-speed, two-dimensional optical light modulators. Two phased-array modulators have been designed and will be described in this section.

MEMBRANE LIGHT MODULATOR

The Membrane Light Modulator (MLM) is a mirror whose surface can be deflected in localized areas by electrostatic forces. A diagram of the physical structure of the MLM developed for the Applied Physics Laboratory by the Perkin-Elmer Corporation (Norwalk, Connecticut) is shown in Fig. 1. The complete device is fabricated on one face of a 6-mm-thick optical flat. A thin chromium-gold film is vacuum deposited onto this glass substrate and then etched into 100 stripes 40 μm wide and on 50-μm centers to form the electrode structure. This area is covered with a thin protective layer of silicon monoxide (SiO) that protects against electrical breakdown. A second layer of SiO about 1.5 μm thick is applied which contains 10 000 individual cylindrical wells in a 100-by-100 array. As shown in Fig. 2, the rows of the array are aligned with the chromium-gold stripes of the electrode structure. The wells are 37.5 μm in diameter and are on 50-μm centers in both directions. The next layer is a collodion membrane approximately 0.1 μm thick. The membrane is coated with a thin layer of antimony which serves as a conducting, reflecting surface.

The antimony acts as a common electrical ground for all of the elements. When a voltage is applied to one of the electrodes all of the elements in the row deflect

- 3 -

ILLUMINATION

ANTIMONY FILM 0.03 μm

COLLOOION MEMBRANE 0.1 μm

50 μm

50 μm

37 μm

0.1 μm

40 μm

CHROMIUM-GOLO
ELECTROOE

SILICON MONOXIOE
SUPPORTING STRUCTURE
1.5 μm

6 mm GLASS
SUBSTRATE
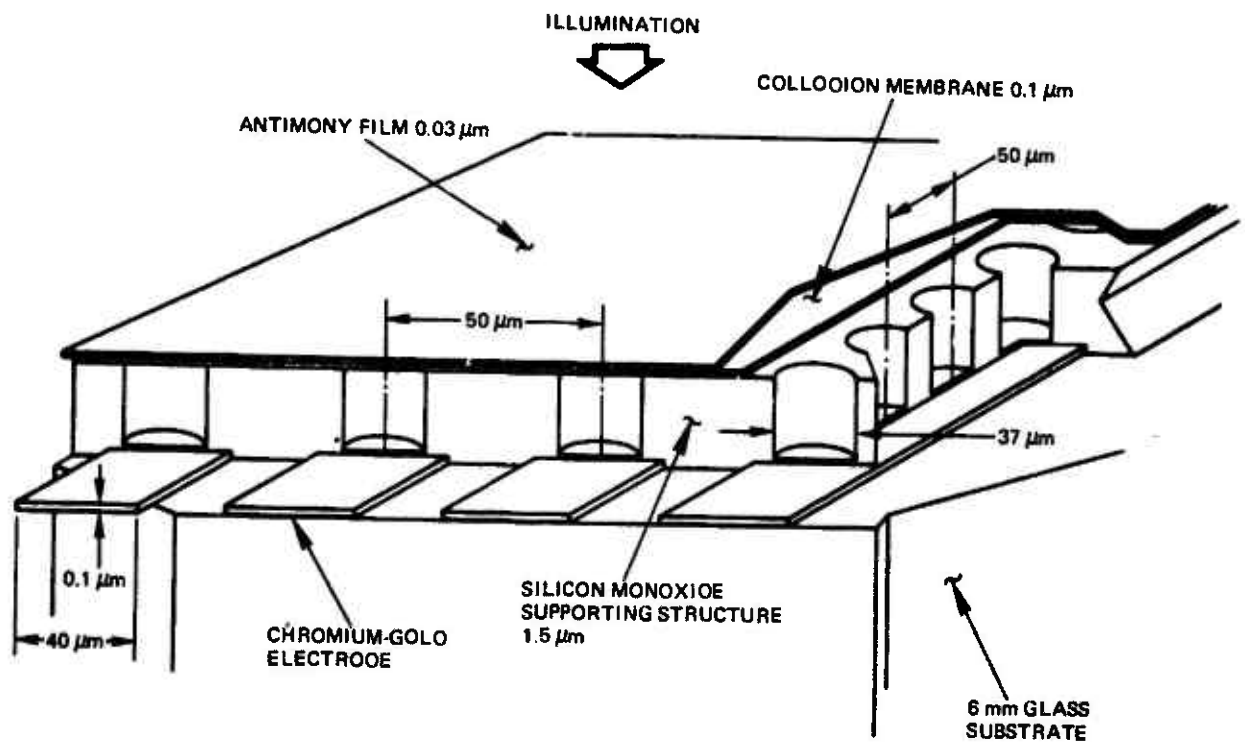
Fig. 1   CROSS-SECTIONAL VIEW OF THE MEMBRANE LIGHT MODULATOR
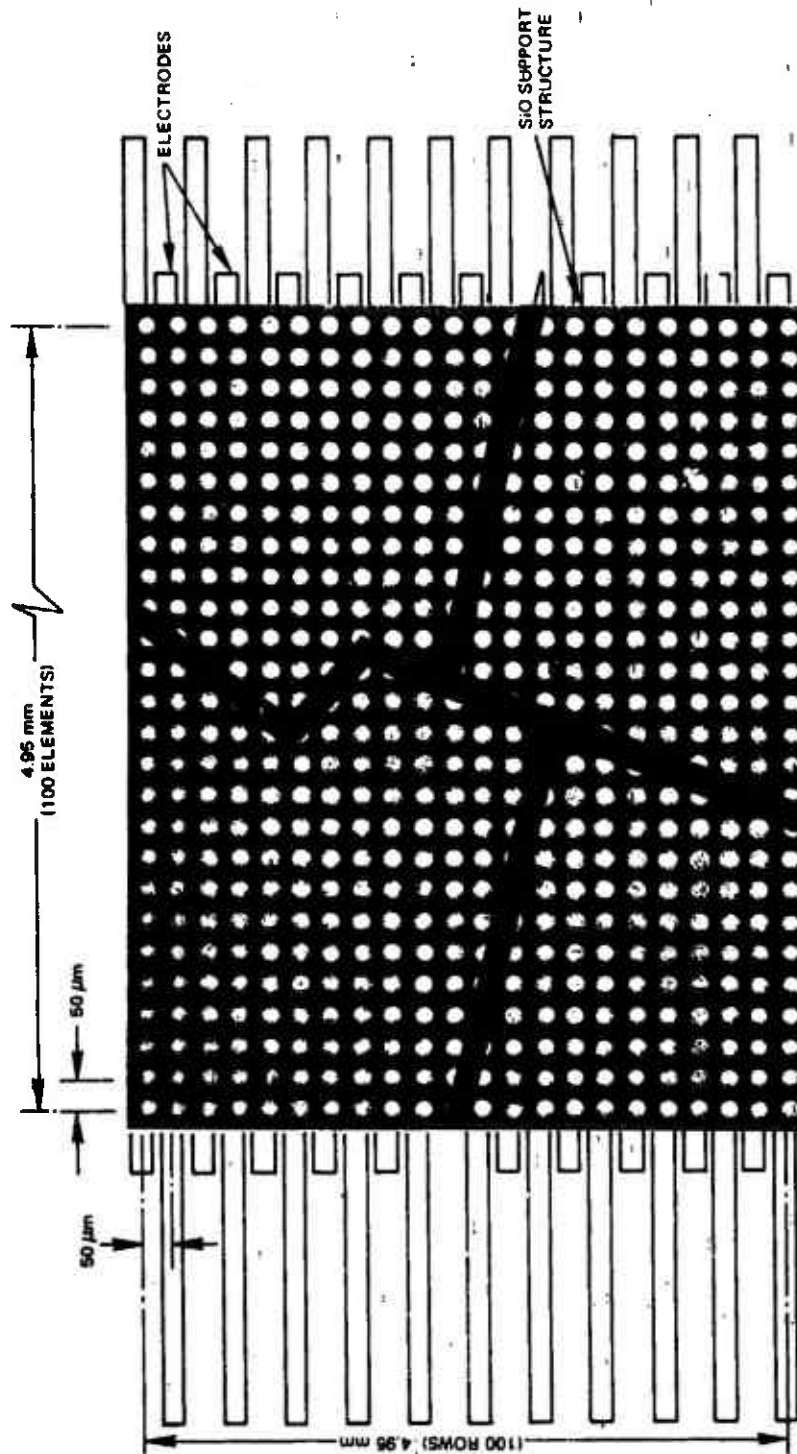
Fig. 2 ELEMENT ARRAY PATTERN OF THE MEMBRANE LIGHT MODULATOR

into the wells due to the electrostatic force. The shape of the deflected modulator elements is approximately parabolic (Fig. 3) and the phase of the light reflected off an individual element can be described by:

$$\varphi(r) \approx \varphi_0 \left(1 - \frac{r^2}{R_0^2} \right), \tag{1}$$

where φ_0 is the peak phase reflected off the center of a modulator element, r is the polar coordinate originating from the center of the element, and R_0 is the radius of the element.

In order to approach flat or "piston-like" phase modulation (and also to eliminate the light reflected off the area between the elements), the parabolic elements are masked such that only the light from the central area of the modulator elements is used. This is accomplished by imaging the modulator (at unity magnification) onto an opaque mask that consists of a two-dimensional array of circular apertures located on the same centers as the modulator elements (Fig. 4).

Assuming perfect imaging, the average phase across a mask aperture can be determined by the equation:

$$\varphi_{AV} = \frac{\int_0^R \varphi_0 \left(1 - \frac{r^2}{R_0^2} \right) 2\pi r\, dr}{\int_0^R 2\pi r\, dr}$$

$$= \varphi_0 \left(1 - \frac{R^2}{2 R_0^2} \right), \tag{2}$$

where φ_{AV} is the average phase across the mask apertures, R_0 is the radius of the modulator element, and R is the
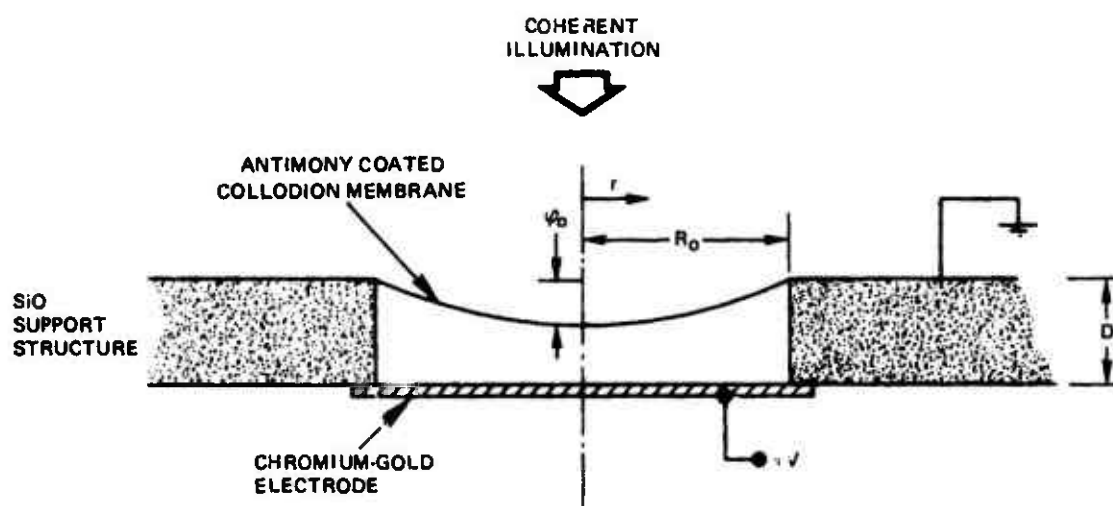
Fig. 3   CROSS-SECTIONAL VIEW OF A DEFLECTED MLM ELEMENT
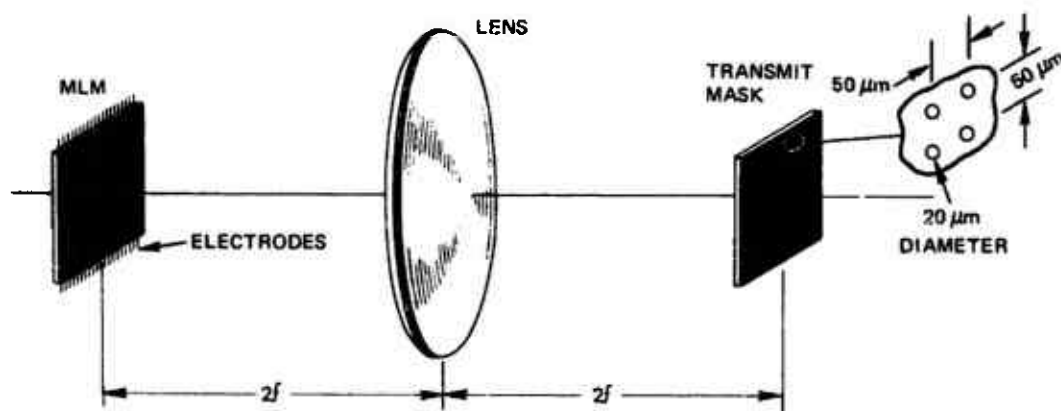
Fig. 4   MLM IMAGED ONTO TRANSMIT MASK AT UNITY MAGNIFICATION

radius of the mask apertures. As the aperture diameter is decreased, the average phase (φ_{AV}) approaches the peak phase (φ_{O}) and therefore the light transmitted through the mask appears more like a piston modulator. However, the total power decreases as the aperture diameter decreases. As a compromise between these two factors, 20-μm-diameter apertures are used (20 μm is approximately one-half the diameter of the modulator elements). The average phase across the 20-μm apertures is:

$$\varphi_{AV} = \frac{7}{8}\varphi_{o} \,. \tag{3}$$

The peak phase reflected off a modulator element is a function of the voltage applied to the electrodes. For small deflections, the peak phase is approximately proportional to the square of the voltage applied:

$$\varphi_{o} \approx kV^2 \,, \tag{4}$$

where

$$k \propto \frac{2\pi}{\lambda}\left(\frac{\epsilon R_{o}^2}{8TD^2}\right),$$

ϵ = the permittivity of the air in the well,

R_{o} = the radius of the well,

D = the depth of the well,

T = the tension of the membrane (assumed to be constant for small deflections), and

λ = the wavelength of the illuminating beam.

However, for larger deflections, the peak phase is a function of higher-order powers of voltage. A more detailed description of the theoretical relationship of phase and

voltage is given in Appendix A. The modulator electronics
have been fabricated under the assumption that these higher-
order terms are negligible.

When overvoltages are applied to the modulator
elements, they "bottom out." The collodion membrane
adheres to the thin SiO protective layer over the electrode
structure. The maximum stable deflection is 44% of the
initial separation (D). If it is desired to utilize a 25% de-
flection, a further increase of only 10% in voltage will
cause instability (see Appendix A). The modulator ele-
ments were also found to bottom because of the creepage
of the membrane when moderate voltages were applied for
long periods of time. The electrical protection circuits
described in Appendix B were added to prevent the modu-
lator elements from bottoming.

In order to determine the time response character-
istics of the modulator elements, the membrane stretched
over the cylindrical wells can be considered as a drum
head having natural frequencies of vibration. The funda-
mental resonant frequency is given (Ref. 1) by:

$$f = \frac{2.4}{2\pi R_o} \frac{T}{\sigma} ,$$
(5)

where

R_o = the radius of the wells,

T = the tension of the membrane, and

σ = the mass of the membrane per unit area.

In a vacuum, the MLM surface resonates at about 2.5
MHz with a Q of about 30. If air is trapped in the wells,
the system appears stiffer because of air compression
and the resonant frequency is raised to about 3 MHz.
However, the vibration is more strongly damped.

Since the membrane permits air to diffuse through it, there will be a slow relaxation of the membrane under a steady deflecting force as the air escapes. The time required for the membrane to reach a steady-state position is in the order of 25 to 100 μs. Because of this, the modulator is operated in a vacuum when fast time response is required.

Several variations of the MLM have been designed by Perkin-Elmer on internal research and development (R&D) programs. In the self-masked modulator the transmit mask is an integral part of the modulator (Fig. 5a). The illumination is in the opposite direction of our MLM and circular holes have been etched in the opaque electrodes to provide the masking. This MLM does not require the use of an imaging lens (and therefore avoids all the alignment problems associated with it). In the Electron Beam MLM, the membrane of the self-masked modulator is coated with small circular pads — one for each modulator element (Fig. 5b). An electron gun "writes" a charge density on the pads. Since the charge at each element can be controlled independently, this version is an inherently two-dimensional device (Ref. 2).

MULTICHANNEL LITHIUM TANTALATE PHASE MODULATOR

In the past, the high voltages required for 2π phase modulation have limited the use of electro-optic crystals. This section describes a multichannel lithium tantalate phase modulator whose speed and 2π voltage are compatible with high-speed microelectronics.

A multichannel lithium tantalate phase modulator (Fig. 6) has been fabricated for the Applied Physics Laboratory by the Isomet Corporation (Palisades Park, New Jersey). The crystal is cut and polished such that the surfaces are perpendicular to the $\hat{X}_1$, $\hat{X}_2$, $\hat{X}_3$ axes (corresponding to the $\hat{a}$, $\hat{b}$, and $\hat{c}$ axes of the crystal).

- 11 -

100 ELEMENTS PER ELECTRODE

100 ELECTRODES

34 μm

50 μm

50 μm

REFLECTIVE LAYER

CIRCULAR MASK

OPAQUE LAYER

PERFORATED LAYER

METAL ELECTRODE

GLASS SUBSTRATE (1.5 mm)

POLYMER MEMBRANE

ANTI-REFLECTION LAYER

ILLUMINATION
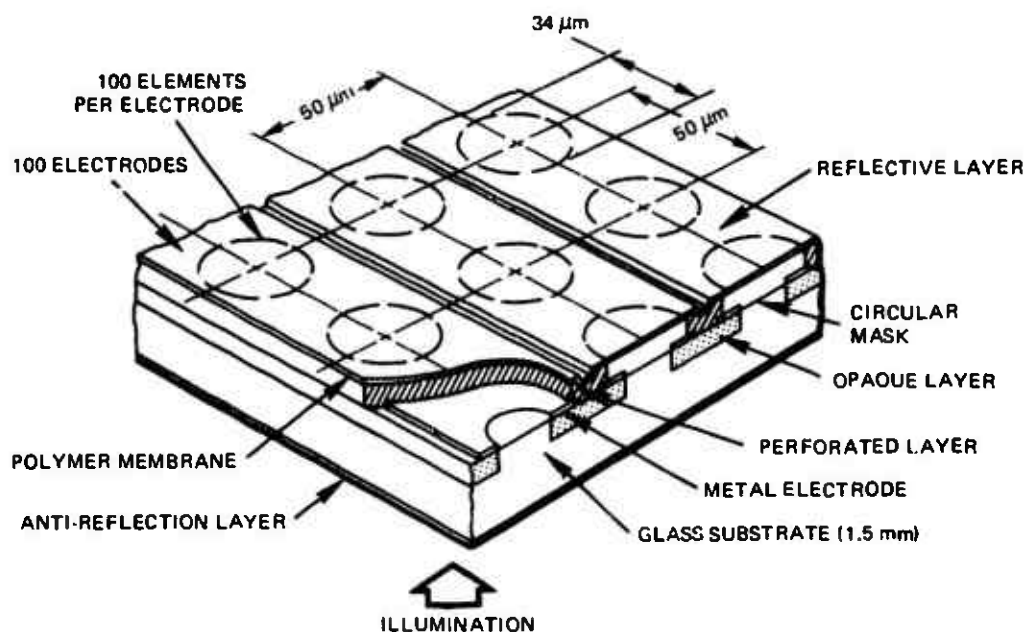
(a) CROSS-SECTIONAL VIEW OF SELF-MASKED MLM

100 ELEMENTS PER ELECTRODE

100 ELECTRODES

34 μm

50 μm

50 μm

CIRCULAR PADS

CIRCULAR MASK

OPAQUE LAYER

PERFORATED LAYER

METAL ELECTRODE

GLASS SUBSTRATE (1.5 mm)

POLYMER MEMBRANE

ANTI-REFLECTION LAYER

ILLUMINATION
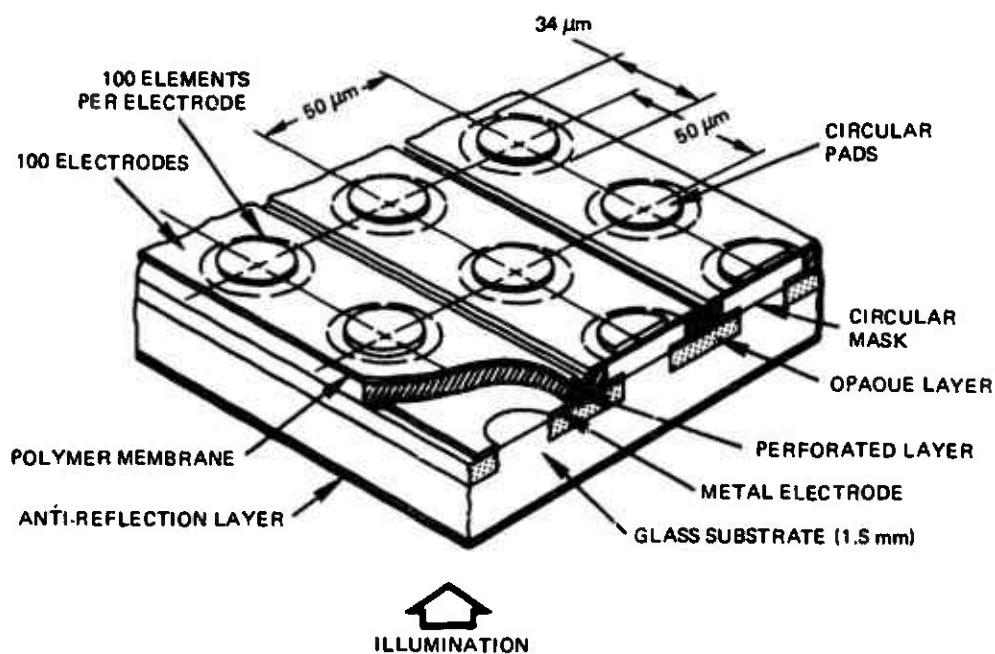
(b) CROSS-SECTIONAL VIEW OF ELECTRON BEAM MLM

Fig. 5   NEW VERSIONS OF THE MEMBRANE LIGHT MODULATOR
(COURTESY OF PERKIN–ELMER CORPORATION)
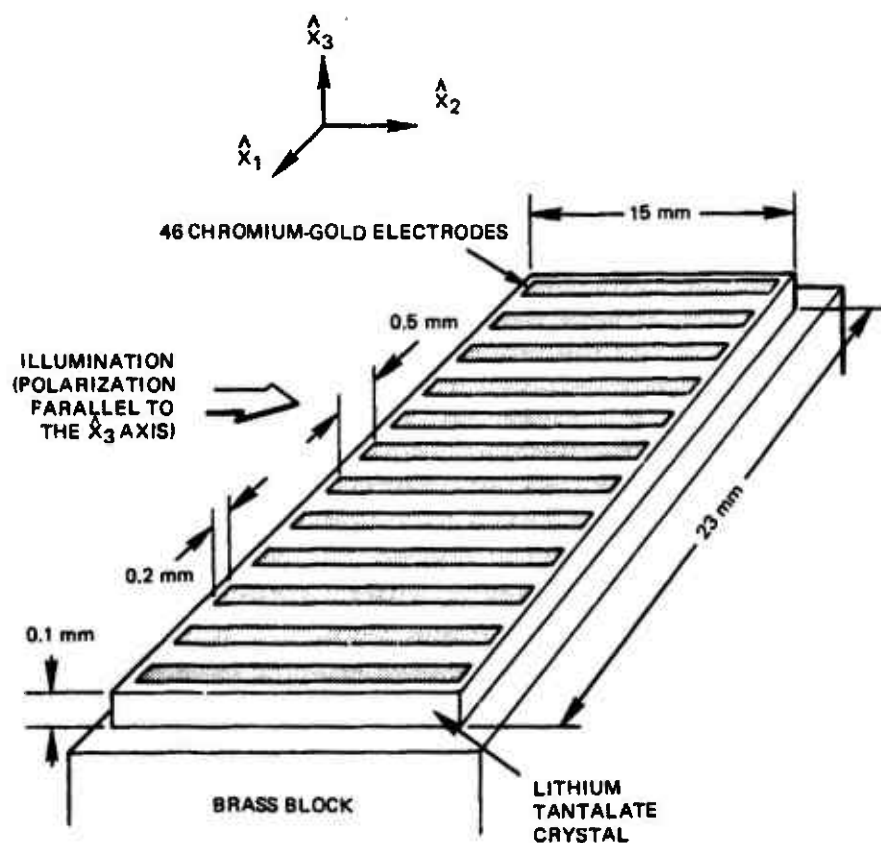
Fig. 6   MULTICHANNEL LITHIUM TANTALATE PHASE MODULATOR

The bottom surface of the crystal (perpendicular to the X_3 axis) is coated with a thin layer of chromium-gold which acts as a common electrical ground. This surface is then bonded to a brass block whose thermal expansion coefficients are approximately equal to those of lithium tantalate so that strain is not induced in the crystal due to thermal expansion. The brass block also acts as a mechanical clamp to inhibit changes in the crystal refractive indices due to the piezoelectric and photoelastic effects (Ref. 3). A thin layer of chromium-gold is deposited on the top surface of the crystal and etched into 46 parallel electrodes 0.2-mm wide and on 0.5-mm centers. These electrodes are parallel to the $\hat{X}_2$ axis of the crystal.

The electro-optic properties of single domain lithium tantalate have been well documented (Ref. 4). Lithium tantalate is uniaxial and remains uniaxial (without a rotation of the principal axes) when an electric field is applied parallel to the $\hat{X}_3$ axis (Ref. 6). Coherent light polarized parallel to either the $\hat{X}_1$ or $\hat{X}_3$ axes and propagating along the $\hat{X}_2$ axis will remain linearly polarized as an electric field is applied which is parallel to the $\hat{X}_3$ axis. The crystal exhibits birefringence (both natural and induced) and therefore light which is not polarized parallel to the $\hat{X}_1$ or $\hat{X}_3$ axis will in general become elliptically polarized.

When a voltage is applied to one of the electrodes of the phase modulator described above, the electric field under the central area of the electrode is approximately parallel to the $\hat{X}_3$ axis. Assuming that the field is uniform, the light which propagates under the electrode will be retarded in phase (due to the linear electro-optic effect) by an amount:

$$_3\Delta\varphi_3 \approx \frac{-\pi \, \ell_2 \, n_3^3 \, r_{33} \, V_3}{\lambda \ell_3} \, , \tag{6}$$

for light polarized parallel to the $\hat{X}_3$ axis, and:

$$_1\Delta\varphi_3 \approx \frac{-\pi \, \ell_2 \, n_1^3 \, r_{13} \, V_3}{\lambda \ell_3} \,, \qquad (7)$$

for light polarized parallel to the $\hat{X}_1$ axis, where

ℓ_2 = the length of the crystal in the $\hat{X}_2$ direction (15 mm),

ℓ_3 = the thickness of the crystal in the $\hat{X}_3$ direction (0. 10 mm),

n_3 = the natural index of refraction for light polarized parallel to the $\hat{X}_3$ axis (2. 180),

n_1 = the natural index of refraction for light polarized parallel to the $\hat{X}_1$ axis (2. 175),

r_{33} = a linear electro-optic coefficient (3. 0 x 10^{-9} cm/V),

r_{13} = a linear electro-optic coefficient (6. 9 x 10^{-10} cm/V),

λ = the wavelength of illuminating beam (6328 Å), and

V_3 = the voltage applied to the electrode.

From these equations it can be seen that the voltage required for 2π phase modulation is dependent on the length-to-thickness ratio (ℓ_2/ℓ_3) of the modulator elements. For the present modulator dimensions, approximately 27 volts is required for a complete 2π phase modulation when the light is polarized parallel to the $\hat{X}_3$ axis, and approximately 120 volts is required when the light is polarized parallel to the $\hat{X}_1$ axis. In order to be within the voltage range of high-speed transistor electronics, the illuminating polarization of the crystal modulator was chosen to be parallel to the $\hat{X}_3$ axis.

- 15 -

The electric field distribution is nonuniform and also not parallel to the $\hat{X}_3$ axis at positions which are not near the center area under the electrodes due to the electric field "fringing" effects. Therefore, light which propagates along these parts of the crystal will not be uniformly phase modulated and also will become elliptically polarized. A mask is used to block the light from all but the central areas under the electrodes. The present mask consists of a linear array of 100-by-100-μm apertures located on the same centers as the electrodes (Fig. 7).

The relative dielectric constant (ϵ_r) along the $\hat{X}_3$ axis for lithium tantalate is 43 (Ref. 4), and therefore the effective capacitance of the elements (which limits the frequency response of the modulator) is approximately 10 pF.

Measurements on the masked modulator indicate that approximately 32 volts is required for 2π phase modulation and that the modulation follows a linear voltage law.

With no voltages applied to the crystal electrodes, phase distortion of an illuminating plane wave has been observed at the output surface of the crystal. This phase distortion (caused by nonuniformities of the crystal) can be compensated by applying appropriate voltages to the modulator electrodes.

The present crystal modulator has 46 continguous useful independent elements. There are several problems associated with attempting to increase the number of elements in the array. For 2π phase voltages which are compatible with high speed transistor electronics, the length-to-thickness ratio of the modulator elements (l_2/l_3 in Eq. (6)) must be large. The difficulty in fabricating thin crystals has limited the crystal lengths to approximately 25 mm (for 0.1 mm thickness). A higher density of electrodes on the present crystal will not result in a satisfactory modulator. If the electrodes are located on closer centers, the cross talk between elements

- 16 -
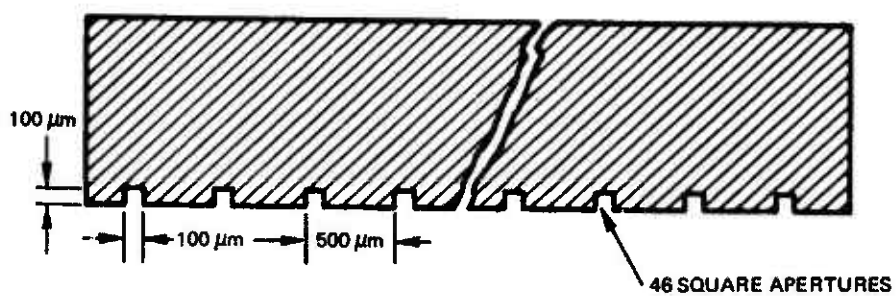
Fig. 7   TRANSMIT MASK FOR 46 CHANNEL CRYSTAL PHASE MODULATOR

(the field under one electrode due to a voltage applied to an adjacent electrode) becomes high. If the width of the electrode is decreased, the electric field "fringing" effects becomes a limiting factor because the useful area where the field is uniform becomes smaller.

An attempt has been made to use two 25-mm crystals mounted end to end in order to make a longer array. However, the axes of these crystals could not be aligned with each other. Even if the crystal axes could be aligned, the physical length of the array (50 mm) would require a high quality transform lens in order to avoid distortion in the transform plane.

A more detailed discussion of the electro-optic effect and the derivation of Eqs. (6) and (7) are given in Appendix C.

3. BEAM-STEERING PROPERTIES OF AN OPTICAL PHASED-ARRAY ANTENNA

For many years, phased-array antennas have been used in radar to perform two-dimensional electronic beam steering at microwave frequencies. With the development of optical phased arrays, this electronically controlled beam-steering technique can now be extended to optical wavelengths. In this section, the beam-steering properties of an optical phased array will be briefly described. A more detailed description is given in Appendix D.

Consider first a linear array of coherent iso-tropic light sources in the front focal plane of a "perfect" lens (Fig. 8). The spatial Fourier transform (or antenna pattern) of this array exists in the back focal plane of the lens and is described by the equation:

$$U_a(\xi, \eta) = \sum_{m=1}^{M} A_m \exp(j\varphi_m) \exp\left[-j \frac{2\pi}{\lambda f} \left(m - \frac{M+1}{2}\right) \Delta X \xi\right], \quad (8)$$

where $U_a(\xi, \eta)$ = the complex light distribution in the Fourier transform plane (note that U is independent of η for this one-dimensional array),

M = the number of point radiators,

A_m = the amplitude of the mth radiator,

φ_m = the relative phase of the mth radiator,

ΔX = the center spacing of the elements,

λ = the wavelength of the illumination, and

f = the focal length of the lens.

- 19 -
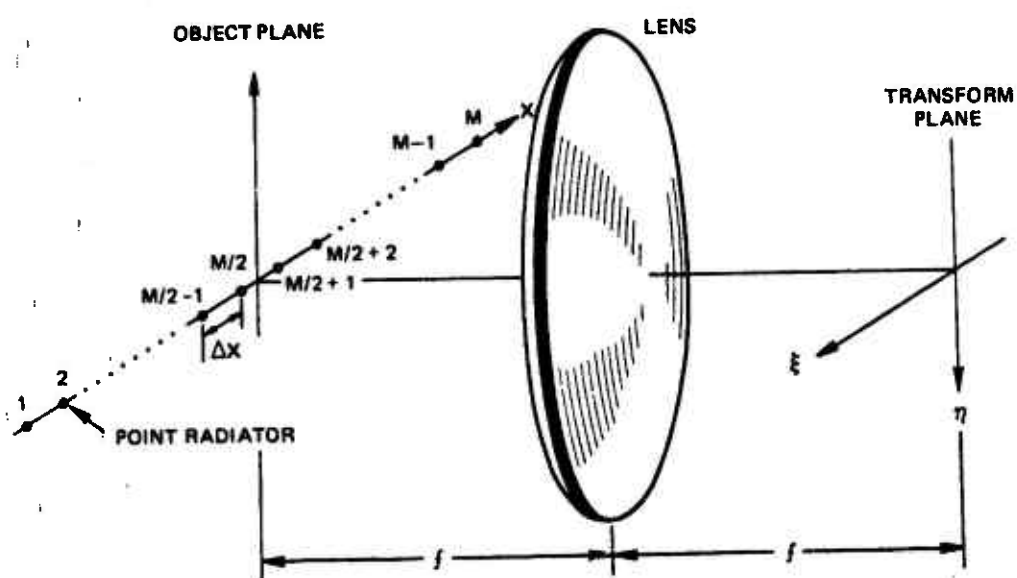
Fig. 8   LINEAR ARRAY OF M EQUALLY SPACED ISOTROPIC RADIATORS IN THE
FRONT FOCAL PLANE OF A LENS

When the radiators are of the same amplitude and phase, this equation reduces to:

$$U_a(\xi) = A \frac{\sin\left[(M\pi\Delta X\xi)/\lambda f\right]}{\sin\left[(\pi\Delta X\xi)/\lambda f\right]} . \tag{9}$$

The power in the transform plane is given by:

$$|U_a(\xi)|^2 = U_a(\xi)U_a^*(\xi)$$

$$= A^2 \frac{\sin^2\left[(M\pi\Delta X\xi)/\lambda f\right]}{\sin^2\left[(\pi\Delta X\xi)/\lambda f\right]} . \tag{10}$$

A plot of Eq. (10) for six point radiators (M = 6) is shown in Fig. 9. The grating lobes (or ambiguity peaks) of the pattern occur when both the numerator and denominator vanish simultaneously. This occurs whenever:

$$\xi = \frac{K\lambda f}{\Delta X} , \tag{11}$$

where $K = 0, \pm 1, \pm 2, \ldots$ These peaks represent the ambiguities of the transform pattern.

The relative power at the peaks is proportional to $M^2 A^2$, and their width (from the peak to the first zero) is:

$$\Delta\xi = \frac{\lambda f}{M\Delta X} . \tag{12}$$

Consider the case where a linear phase slope of p cycles exists across the array. The phase of the mth element is defined by

$$\varphi_m = \frac{2\pi m}{M} p . \tag{13}$$

- 21 -
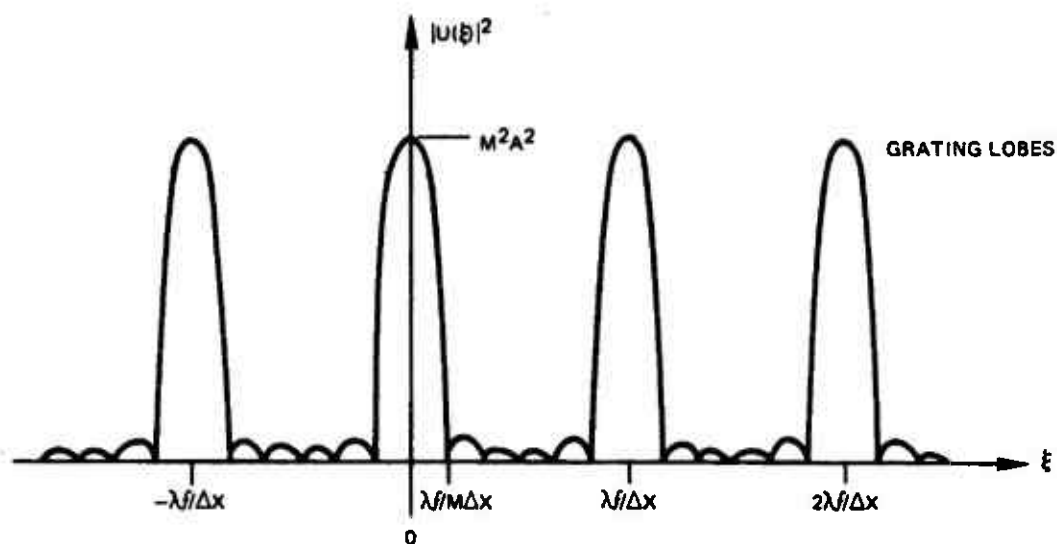
Fig. 9 TRANSFORM PATTERN FOR A LINEAR ARRAY OF
6 EQUALLY SPACED ISOTROPIC RADIATORS (M = 6)

When this is substituted into Eq. (8), the result is

$$U_a(\xi) = A \frac{\sin[(M\pi\Delta X\xi)/\lambda f - \pi p]}{\sin[(\pi\Delta X\xi)/\lambda f - \pi p/M]} . \tag{14}$$

This equation has a peak whenever:

$$\xi = (K + \frac{p}{M})\frac{\lambda f}{\Delta X} , \tag{15}$$

where $K = 0, \pm 1, \pm 2, \ldots$

This pattern has the same shape as Fig. 9 except that now the peaks are shifted along the ξ axis by $p(\frac{\lambda f}{M\Delta X})$. Therefore, the location of the peaks on the ξ axis is proportional to the phase slope across the array. Using the Rayleigh resolution criteria (that the peak of one beam be in the null of an adjacent beam), there are M resolvable beam positions between the ambiguities.

A similar analysis can be used to determine the pattern of a two-dimensional array of isotropic radiators. Consider an M-by-N array of isotropic radiators where the spacing of the elements in the X direction is ΔX and the spacing of the elements in the Y direction is ΔY (Fig. 10). The two-dimensional array pattern has the form:

$$U_a(\xi,\eta) = \sum_{m=1}^{M} \sum_{n=1}^{N} A_{mn} \exp(j\varphi_{mn}) \exp\left(-j\frac{2\pi}{\lambda f}((m - \frac{M+1}{2})\Delta X\xi + (n - \frac{N+1}{2})\Delta Y\eta)\right). \tag{16}$$

When the radiators are of the same amplitude and phase, the power in the transform plane is described by

$$|U_a(\xi,\eta)|^2 = A^2 \left[\frac{\sin[(M\pi\Delta X\xi)/\lambda f]}{\sin[(\pi\Delta X\xi)/\lambda f]}\right]^2 \left[\frac{\sin[(N\pi\Delta Y\eta)/\lambda f]}{\sin[(\pi\Delta Y\eta)/\lambda f]}\right]^2 . \tag{17}$$

- 23 -

OPTICAL
PHASED
ARRAY
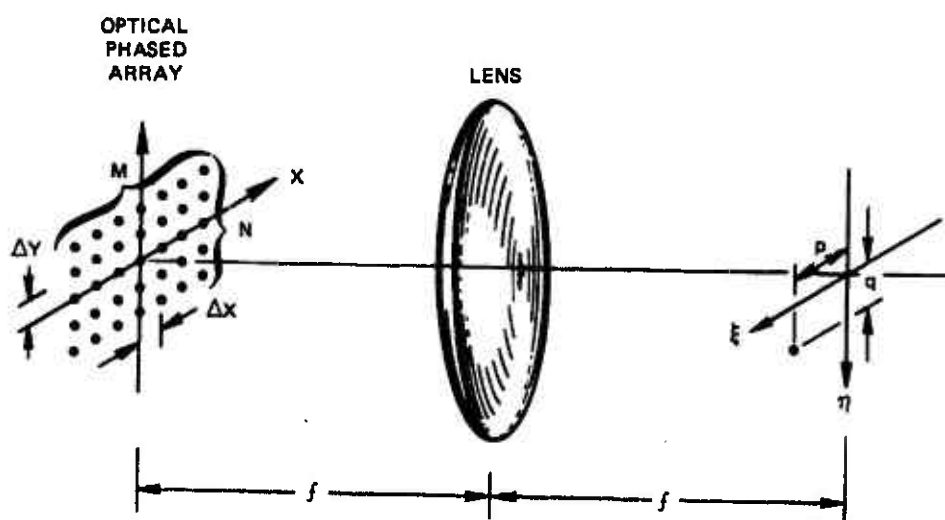
LENS

Fig. 10 TWO-DIMENSIONAL OPTICAL PHASED ARRAY
IN THE FRONT FOCAL PLANE OF A LENS

Figure 11 shows the width (from null to null) and spacing of the grating lobes. (For simplicity, the sidelobes have not been included.) The widths of the lobes (from the peak to the first null) in the ξ and η directions are:

$$\Delta\xi = \frac{\lambda f}{M\Delta X} , \quad \text{and}$$

$$\Delta\eta = \frac{\lambda f}{N\Delta Y} . \tag{18}$$

The relative power of the peaks is proportional to $M^2 N^2 A^2$.

Consider now a linear two-dimensional phase slope across the array where the phase of the (m, n) element is described by

$$\varphi_{mn} = \frac{2\pi m}{M} p + \frac{2\pi n}{N} q . \tag{19}$$

The plane of constant phase is tilted such that there are p cycles of phase across the array in the X direction and q cycles of phase across the array in the Y direction. Substituting Eq. (19) into Eq. (16), the resulting power in the transform plane is described by:

$$|U_a(\xi,\eta)|^2 = A^2 \left[\frac{\sin\left[(M\pi\Delta X\xi)/\lambda f - \pi p\right]}{\sin\left[(\pi\Delta X\xi)/\lambda f - \pi p/M\right]} \right]^2 \left[\frac{\sin\left[(N\pi\Delta Y\eta)/\lambda f - \pi q\right]}{\sin\left[(\pi\Delta Y\eta)/\lambda f - \pi q/N\right]} \right]^2 \tag{20}$$

The pattern takes the same shape as Fig. 11 except that the peaks are now shifted along the ξ axis by $p\left(\frac{\lambda f}{M\Delta X}\right)$ and along the η axis by $q\left(\frac{\lambda f}{N\Delta Y}\right)$. Therefore, the location of the peaks in the (ξ,η) plane indicates the two-dimensional phase slope across the array.
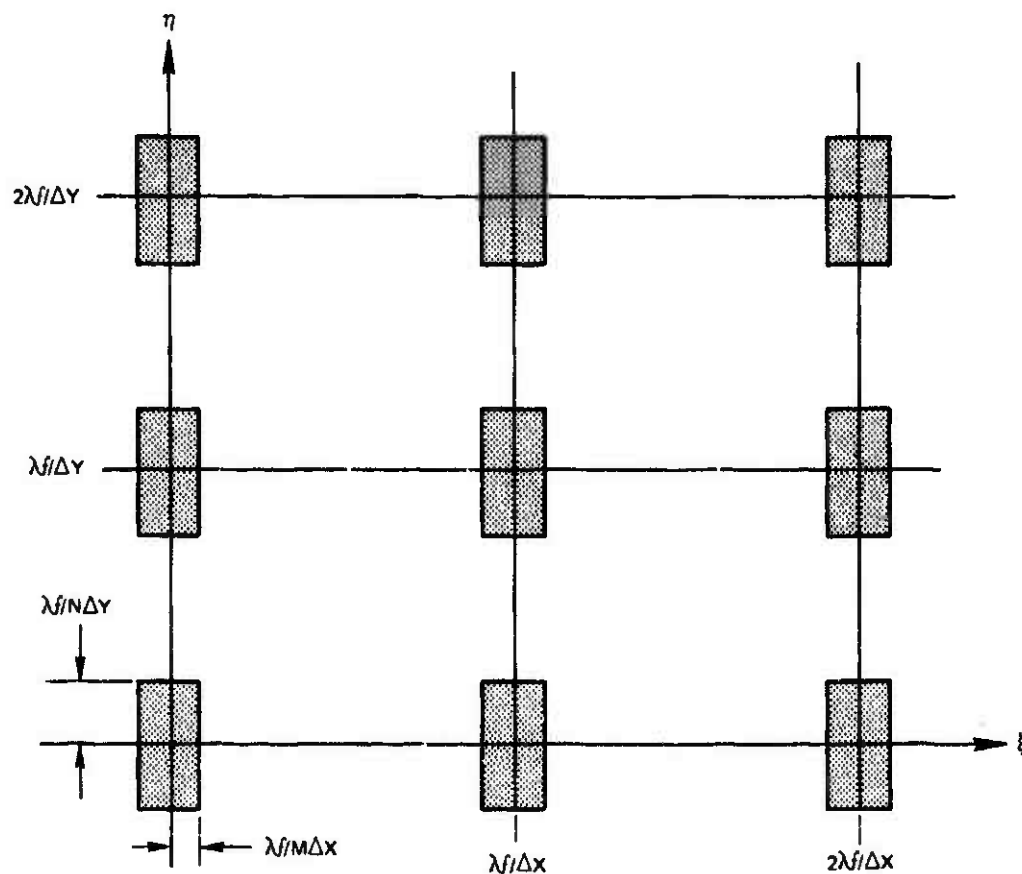
Fig. 11   GRATING LOBE STRUCTURE FOR M-BY-N TWO-DIMENSIONAL
ARRAY OF ISOTROPIC RADIATORS

Again using the Rayleigh resolution criteria, there
are M resolvable beam positions in the ξ direction and
N resolvable beam positions in the η direction. This
results in a total of M times N resolution cells in the
two-dimensional area between the grating lobes.

4. ELECTRONICS

The electronics required for performing optical beam steering with the Membrane Light Modulator (and later, with a slight modification, the crystal modulator) will be described in this section. The use of these electronics for performing radar signal processing will be discussed in Section 8.

In order to perform beam steering with a phased-array antenna, the appropriate linear phase slope must be applied across the array (as discussed in Section 3). The MLM electronics shown in Fig. 12 generates the voltages for each row of the MLM that is required to steer the beam. For a given beam position, the appropriate digital voltage value for each row of the MLM is generated by either the Beam Position Generator (BPG) or by a digital computer. These voltage values are accurate to 6 bits. Paper tape can be used to store the computer-generated voltage values.

Two levels of registers (input and storage) are used. One set of data is held in the storage registers (one 6-bit register per MLM row) while a new set of data is loaded into the input registers. When the input registers are completely loaded, the new set of data is transferred in parallel into the storage registers. The outputs of the storage registers are directly connected to the MLM electrodes via the D/A converters and amplifiers.

The computer-generated words (and also the paper-tape words) are loaded sequentially into the input registers. The BPG-generated words can be loaded sequentially. To provide for fast beam stepping, the BPG generated words can also be loaded into the input registers in a quasi-parallel mode that consists of
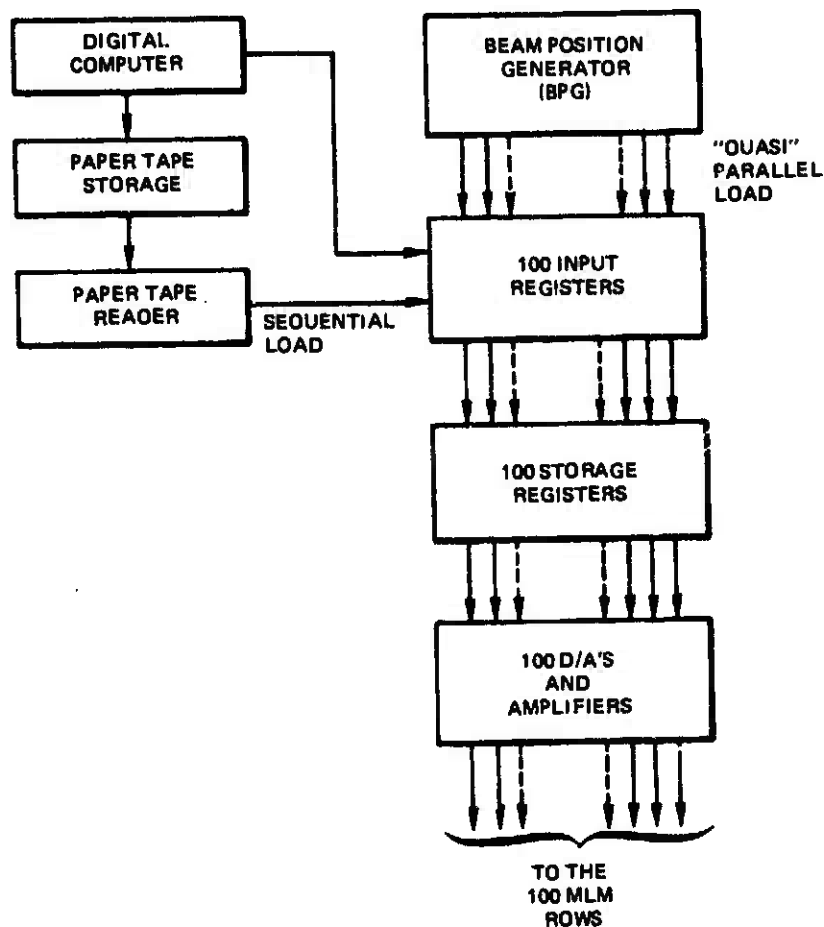
Fig. 12 BLOCK DIAGRAM OF THE HYBRID CORRELATOR ELECTRONICS

parallel groups of 8 channels (with 4 channels remaining for the last group). The 8 channels within a group are loaded in sequence. In this manner, all 100 channels are loaded with 8 clock pulses rather than the 100 clock pulses required in a purely sequential operation.

Since the phase of the light reflected by the MLM elements is proportional to the square of the voltages applied to the elements, the BPG and the computer must first generate the phase slope required for a particular beam position, and then take the square root of these values in order to obtain the relative voltages required. The phase slopes are generated modulo 2π phase.

With 100 elements in the MLM, there are 100 resolvable beam positions between ambiguities (using the Rayleigh criterion). The computer can be used to generate the voltages required for these 100 beam positions. The computer is also used to generate the voltages for two-dimensional beam steering with the thinned MLM arrays (discussed in Section 6). The computer is also used to determine the phases and MLM voltages of the radar pulses (discussed in Section 8). The computer output can either be loaded directly into the MLM input registers or stored on paper tape.

The number 100 is difficult to work with in a digital simulator, so for the purpose of the BPG electronics, the unambiguous region between grating lobes is divided into 128 beam positions. These 128 positions are defined as the unit beam positions and can be further subdivided into fractional positions of 1/2, 1/4, and 1/8.

The BPG has several modes of operation. In the free-running mode, the MLM is stepped continuously through all the beam positions in unit or fractional (1/2, 1/4, or 1/8) steps. The stepping speed is controlled by the basic clock frequency. The minimum time per step is limited by the digital logic to approximately 2 μs. In

- 31 -

the selected beam position mode, the simulator free runs
until it reaches the selected beam position and then stops.
Provisions have been made to allow digital noise to be
added from an external source to the BPG-generated phase
words.

The computer is used to generate the voltage values
required for beam steering with the multi-channel lithium
tantalate phase modulator. A slight modification of the
output amplifiers is required in order to compensate for
the different 2π voltages of the MLM (84 volts) and the
crystal (32 volts). The voltages required to compensate
for the phase distortion across the crystal (discussed in
Section 2) are included in these computer calculations.
Although the BPG has not been used for beam steering with
the crystal, it could be used if the square root operation
(which is required for the MLM) were removed and the
appropriate phase compensation offsets added.

A detailed description of the simulator electronics
is given in Appendix B.

5. ONE-DIMENSIONAL OPTICAL BEAM STEERING

Both the Membrane Light Modulator and the multi-channel crystal modulator have been used to perform one-dimensional phased-array optical beam steering. The optical configuration for these two modulators are different and will be described in this section. The one-dimensional beam steering results for the two modulators will also be given.

MLM BEAM STEERING

A schematic of the optical configuration for one-dimensional beam steering with the MLM is shown in Fig. 13. A He-Ne laser (6328 Å) is used as the coherent light source. Conventional collimating optics expand the laser beam and illuminate the MLM. A beam splitter is used to direct the light. The light which reflects off the MLM is imaged via the beam splitter and lens onto the transmit mask at unity magnification. (The purpose of the transmit mask was discussed in Section 2.) The alignment of the transmit mask and the modulator image is very critical. A slight error in magnification of the image or position of the mask will result in a poor masking of the modulator elements. As described in Appendix E, unity magnification is the best choice for simplification of the alignment procedure.

The image of the masked MLM exists in the front focal plane of the transform lens, and the spatial Fourier transform of the light transmitted through the mask exists in the back focal plane (output plane).

The light intensity in the output plane is read by a scanning mirror readout system. The mirror scans a projected image of the transform pattern across a slit

- 33 -
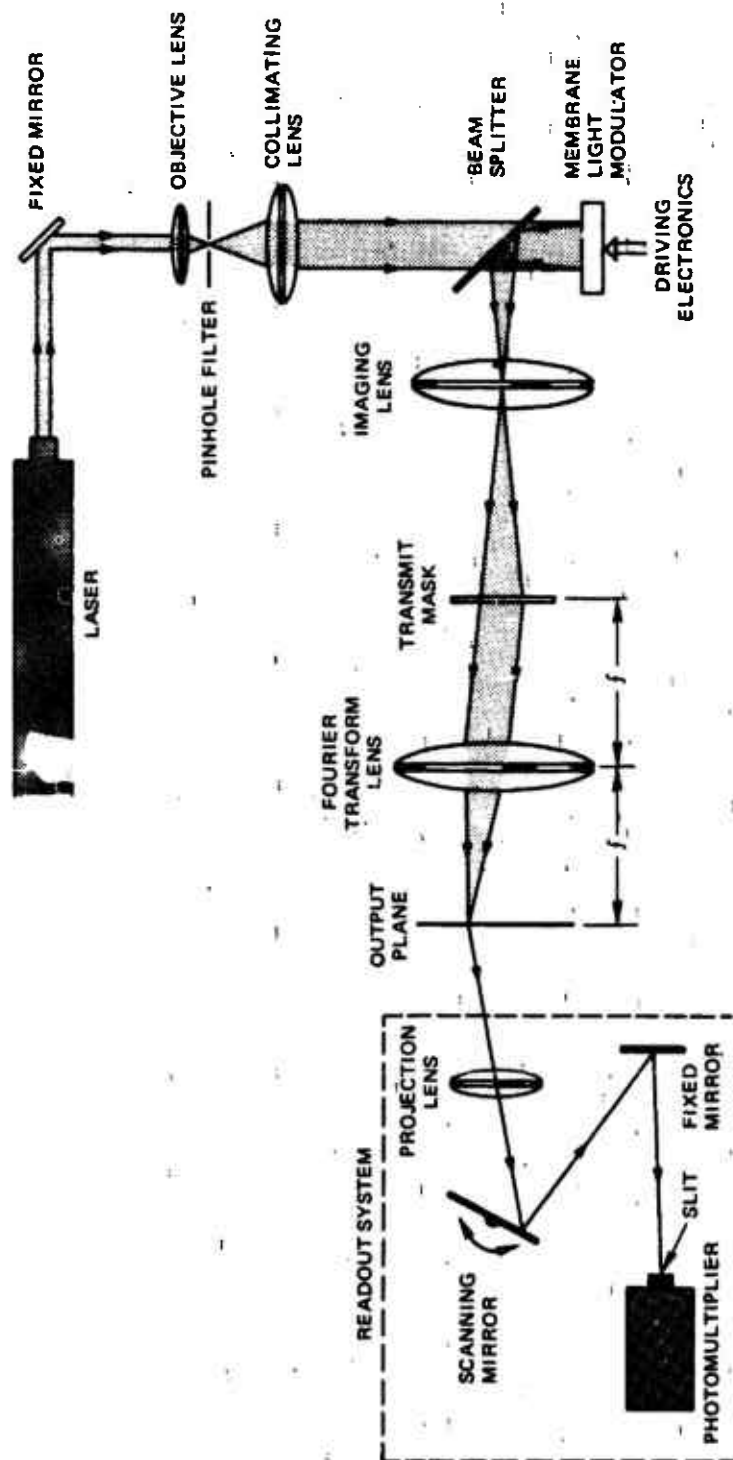
Fig. 13 SCHEMATIC OF THE OPTICAL CONFIGURATION FOR ONE-DIMENSIONAL SIGNAL PROCESSING WITH THE MLM

in front of the photomultiplier so that the current output of the photomultiplier as a function of time corresponds to the intensity of the light in the transform pattern as a function of the position along the scan. The photomultiplier output is displayed on an oscilloscope.

Since all the elements along one row of the MLM are controlled by a single electrode, linear phase slopes (using the full array) can be obtained only in a direction perpendicular to the electrodes (which corresponds to the X direction in the input plane since the electrodes have been aligned to be parallel to the Y axis). Therefore one-dimensional beam steering occurs along the ξ axis in the transform plane. The masked MLM elements have a finite size, and therefore Eq. (20) (which describes the transform pattern for an array of point radiators) must be multiplied by the element pattern. The transform of a uniformly illuminated circular aperture is the familiar Airy pattern, and therefore the power in the transform plane for the masked MLM array can be approximated by:

$$|U(\xi,\eta)|^2 = C \left[\frac{J_1(R\rho)}{R\rho}\right]^2 \left[\frac{\sin\left[(M\pi\Delta X\xi)/\lambda f - \pi p\right]}{\sin\left[(\pi\Delta X\xi)/\lambda f - \pi p/M\right]}\right]^2 \left[\frac{\sin\left[M\pi\Delta X\eta/\lambda f\right]}{\sin\left[\pi\Delta X\eta/\lambda f\right]}\right]^2 . \quad (21)$$

where R $\quad$ = the radius of the mask apertures (20 μm),

$\rho \quad = \frac{2\pi}{\lambda f}(\xi^2 + \eta^2)^{\frac{1}{2}}$, and (for the MLM)

M = N = 100 and

$\Delta X = \Delta Y = 50\ \mu$m.

A photograph of the transform pattern for the masked MLM is shown in Fig. 14a. (The transform pattern is rotated by 45° corresponding to the actual orientation of the MLM array, which is at 45°.) Figure 14b is a plot of the intensity along the ξ axis (marked A-A in

(a) PHOTOGRAPH OF THE MLM TRANSFORM PATTERN

(b) INTENSITY ALONG THE ξ AXIS OF THE MLM TRANSFORM PATTERN
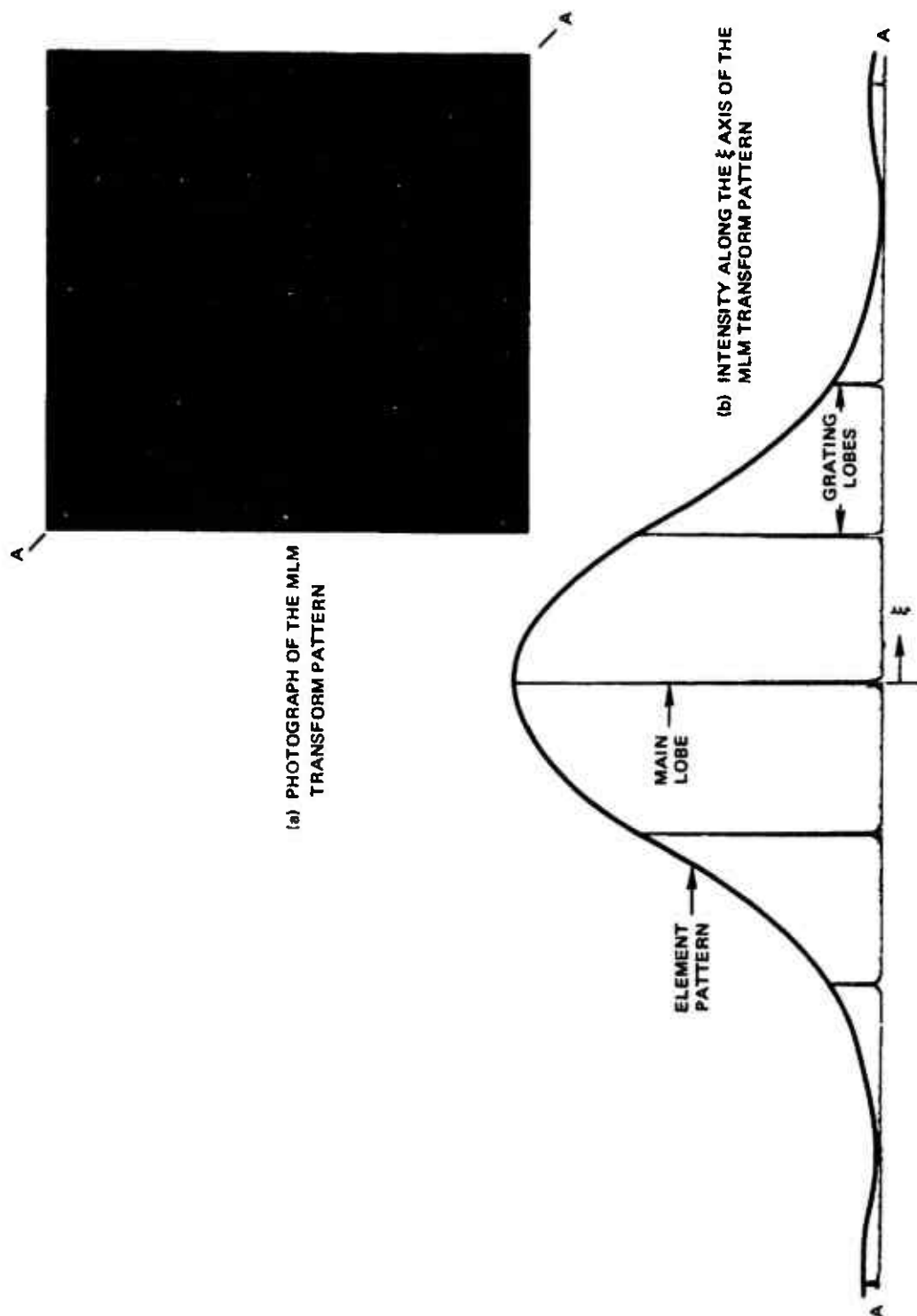
Fig. 14   MLM TRANSFORM PATTERN

the figure). From Eq. (21), there are seven grating lobes under the main lobe of the element pattern. The distance between the grating lobes represents the distance the beam can be steered unambiguously.

A photograph of the main grating lobe on an expanded scale is shown in Fig. 15. A diode is used as the load for the photomultiplier in order to approximate a logarithmic amplifier. The theoretical intensities of the sidelobes relative to the main lobe can be obtained from Eq. (21). Table 1 compares the theoretical intensities of the sidelobes to those measured. As can be seen, the measured values compare favorably with the theoretical values.

Table 1

Comparison of Theoretical and Measured Sidelobe
Intensities for MLM

Lobe	Theoretical Intensity (dB)	Measured Intensity (dB)
Center Lobe (reference)	0	0
First Sidelobe	-13.2	-13.2
Second Sidelobe	-17.7	-17.6
Third Sidelobe	-20.8	-20.2

Due to the frequency response of the diode-photomultiplier combination and also the finite size of the slit in front of the photomultiplier, the nulls in Fig. 15 are not a good representation of the actual nulls achieved in the transform pattern.

Since the MLM has 100 independent rows (M = 100), there are 100 Rayleigh beam positions between the grating lobes. Figure 16 shows several adjacent Rayleigh beam positions. Notice that the peak of one beam occurs in the first null of the adjacent beam position (satisfying the Rayleigh resolution criteria). The intensity at the crossing
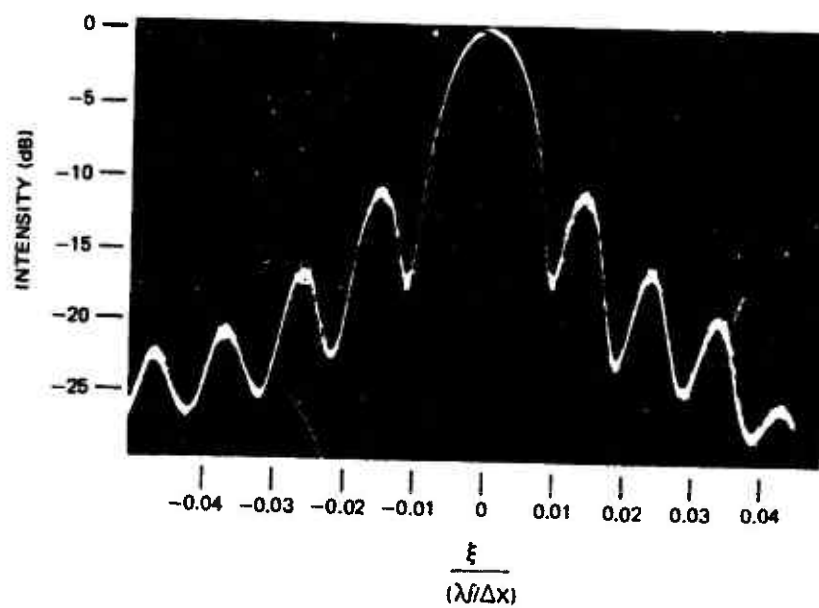
Fig. 15   CENTRAL GRATING LOBE OF THE MLM TRANSFORM PATTERN
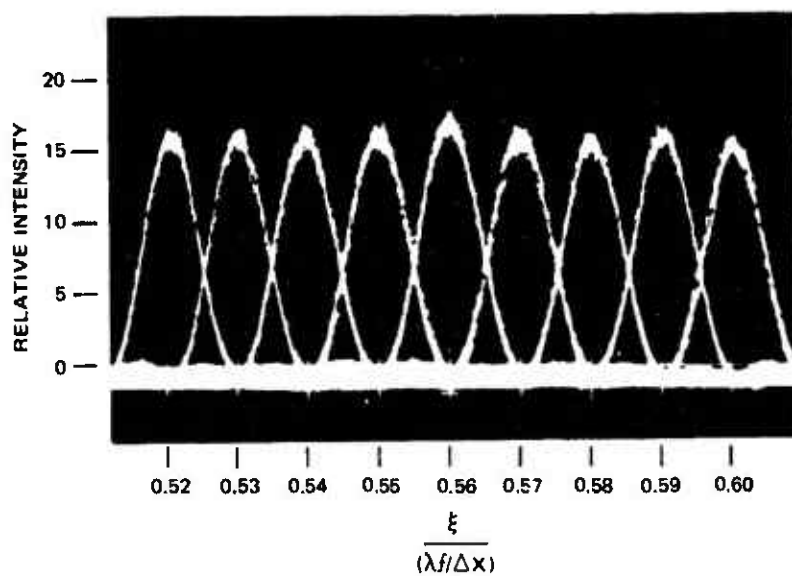
Fig. 16 MLM ONE-DIMENSIONAL BEAM-STEERING RESULTS SHOWING SEVERAL ADJACENT RAYLEIGH BEAM POSITIONS SUPERIMPOSEO ON ONE PHOTO-GRAPH

point is observed to be 4 dB below the intensity of the
peak of one of the beams (obeying Eq. (21)). If a 3-dB
beamwidth were used as the resolution criteria, 113
beam positions could be resolved between the ambiguities.

A photograph of all 100 beam positions is shown in
Fig. 17. The averaged envelope follows the Airy disk
element pattern. However, a large variation of the peak
intensity from one beam position to the next is observed.
(This is especially evident for beam position number 0.)
This is because the element pattern varies with voltage.
When no voltage is applied to the modulator elements,
the wavefront illuminating the circular mask apertures
is flat, and the transform pattern is the Airy pattern.
However, when a voltage is applied, the modulator ele-
ments deflect as paraboloids. The wavefront illuminat-
ing the individual mask apertures now appears parabolic.
This results in a widening of the main lobe of the element
pattern and also a lowering of the peak intensity (along
boresight). The larger the applied voltage, the greater
the effect since the wavefront is more parabolic. The
theoretical intensity on boresight as a function of peak
phase (for 20 μm diameter mask apertures) is plotted
in Fig. 18. By applying the same voltage to all the MLM
electrodes, the variation of intensity on boresight as a
function of the peak phase can be measured. These mea-
surements are also plotted in Fig. 18. Up to around
$3\pi/4$ phase, the theoretical and empirical curves are
approximately the same. However, beyond $3\pi/4$ phase
the measured intensity on boresight drops very quickly.
This is attributed to abberations in the imaging lens.
The theoretical plot in Fig. 18 was made assuming a
perfect lens of infinite aperture (a point impulse re-
sponse function for the lens). For a perfect lens with a
finite aperture, the impulse response function is a sym-
metric Airy pattern. For an $f/4$ lens, the theoretical
intensity versus phase curve has been found to follow
fairly close to the infinite aperture curve for all phase
modulations. The impulse response function for the imaging
lens in the system (which is $f/4.8$) has been measured and

- 40 -
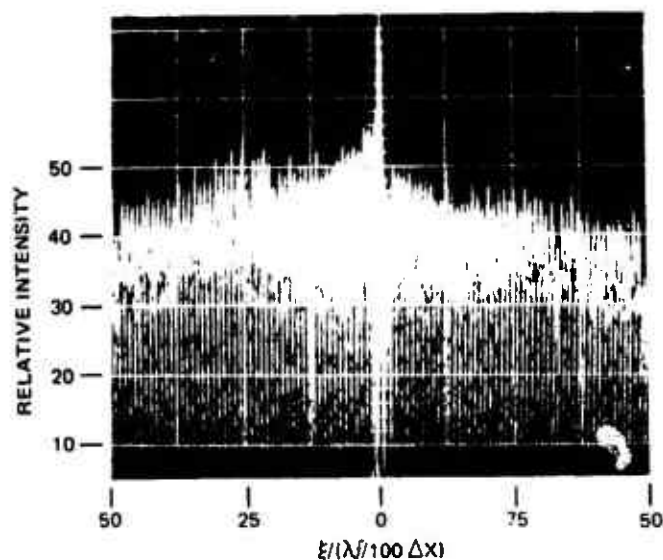
NOTE: FOR PHOTOGRAPHIC REASONS, THE 0 LEVEL HAS BEEN
SHIFTED 1 CM BELOW THE BOTTOM SCALE LINE. THE
AMBIGUITY SPACING CORRESPONDS TO 8 CM. THE
BORESIGHT BEAM (AT $\xi = 0$) HAS BEEN CENTERED ON
THE PHOTOGRAPH

Fig. 17   THE 100 RAYLEIGH BEAM POSITIONS OF THE MLM
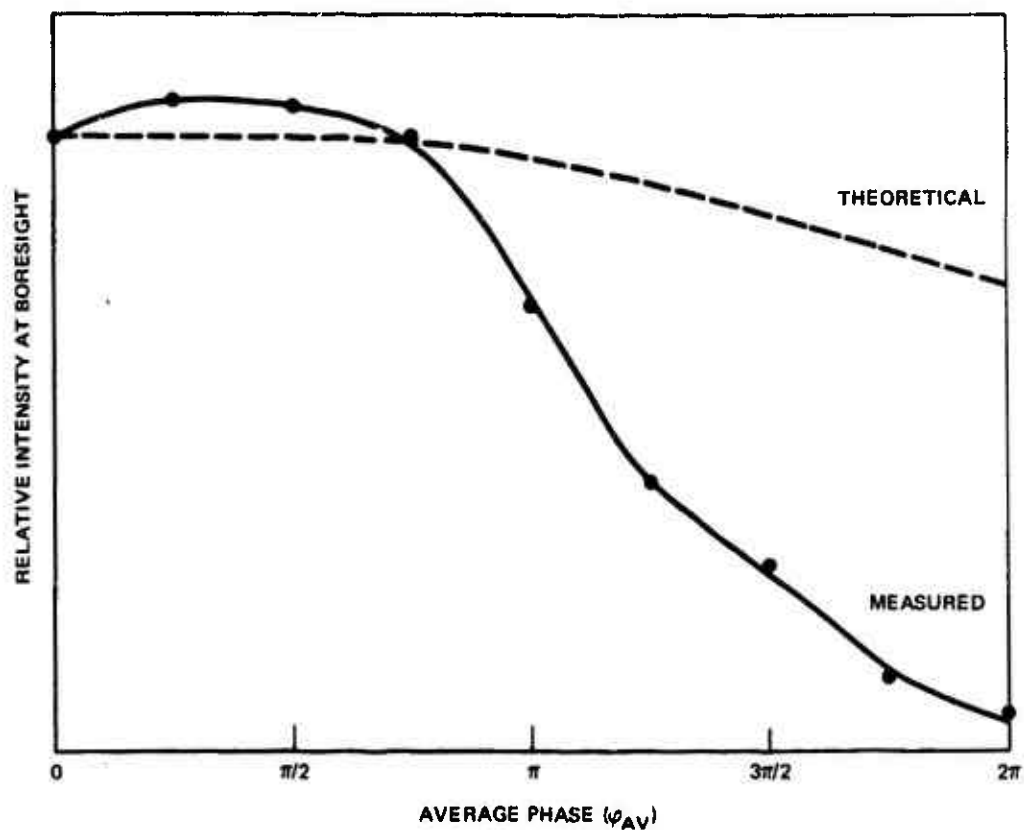
Fig. 18   INTENSITY AT BORESIGHT OF THE MLM TRANSFORM PATTERN AS A
FUNCTION OF THE AVERAGE PHASE ACROSS THE MLM ELEMENTS

is shown in Fig. 19. The fact that this is an imperfect lens
(as evident from the asymmetrical impulse response func-
tion) results in a degradation of the image and probably is
responsible for the discrepancy in the measured intensity
modulation above $3\pi/4$ phase.

CRYSTAL BEAM STEERING

A schematic of the optical configuration for one-
dimensional beam steering with the multi-channel crystal
modulator is shown in Fig. 20. A He-Ne laser (6328 Å)
is used as the coherent light source. A polarizer is used
to cancel out the depolarizing effects of the quartz-coated
mirrors. The polarization rotator is used to align the
polarization of the input beam parallel to the $\hat{X}_3$ axis of
the crystal.

Conventional spherical collimating optics expand
the beam to illuminate the crystal. Because of the rec-
tangular cross section of the crystal (0.1 by 25 mm), only
a small percentage of the circular beam is actually used.
By using cylindrical optics, the circular beam can be
compressed in one dimension such that the beam cross
section more closely corresponds to the crystal cross
section (Fig. 21). The amount of compression is pro-
portional to the ratio of the effective focal lengths of the
cylindrical lenses:

$$m = \frac{D_2}{D_1} = \frac{f_2}{f_1} . \tag{22}$$

As discussed in Section 2, a mask is required to
block the light from the areas between the modulator elec-
trodes. The present mask consists of a linear array of
100-by-100-μm apertures which are on 500-μm centers
(Fig. 22). The transmit mask is positioned within 100 μm
of the output surface of the crystal by means of a 3-axis
translator.
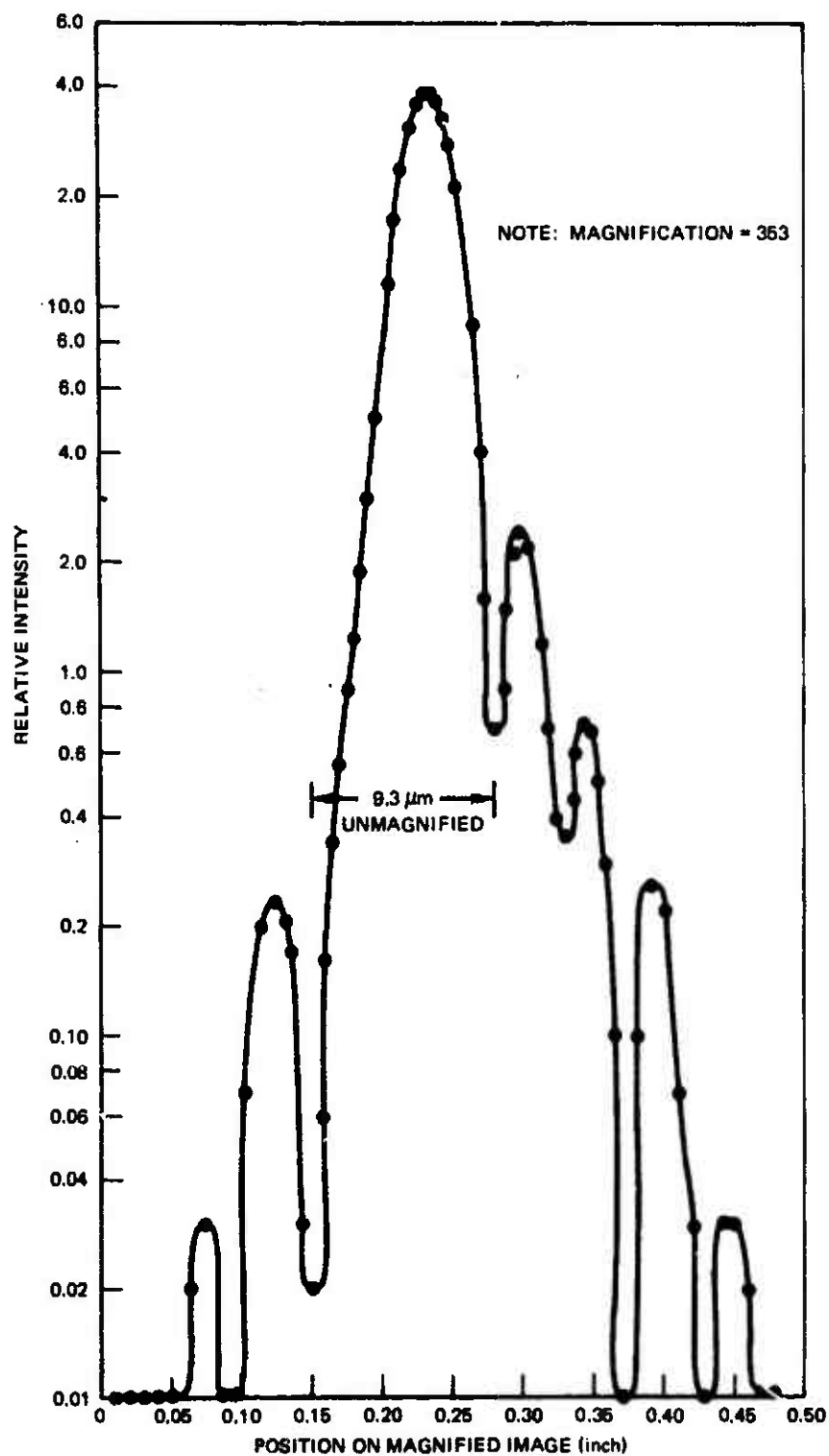
Fig. 19   MEASURED IMPULSE RESPONSE FUNCTION FOR THE MLM IMAGING LENS
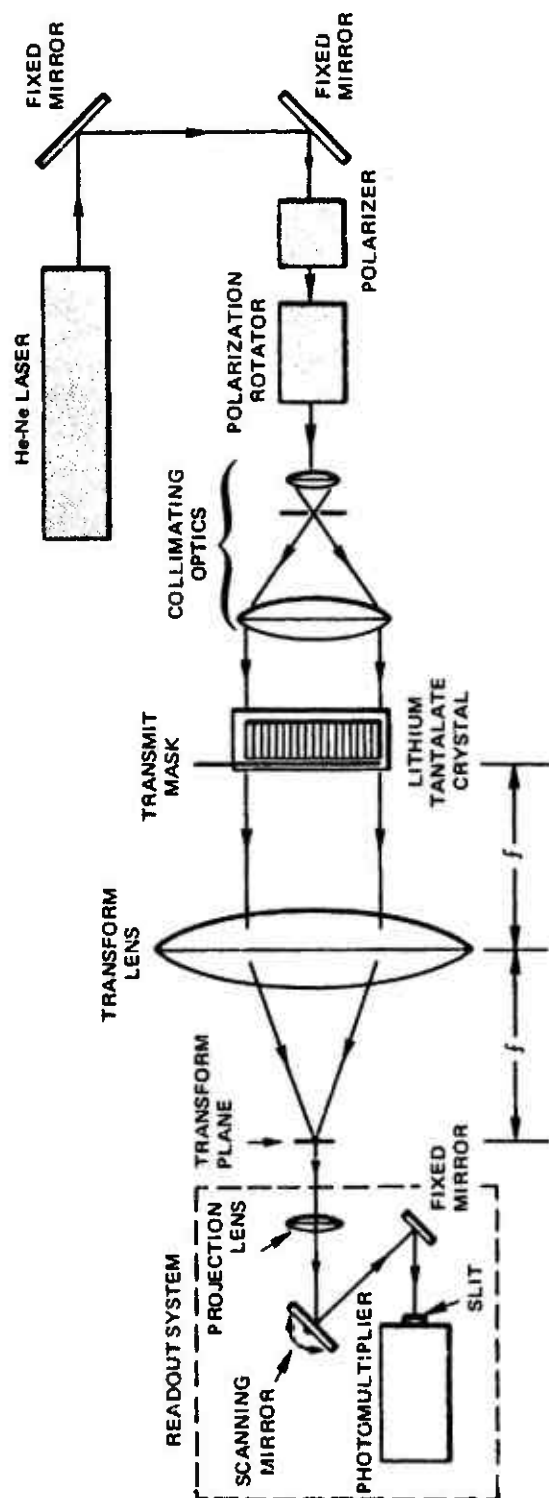
Fig. 20 OPTICAL CONFIGURATION FOR ONE-DIMENSIONAL SIGNAL PROCESSING USING THE MULTICHANNEL LITHIUM TANTALATE PHASE MODULATOR

$M = O_2/O_1 = f_2/f_1$
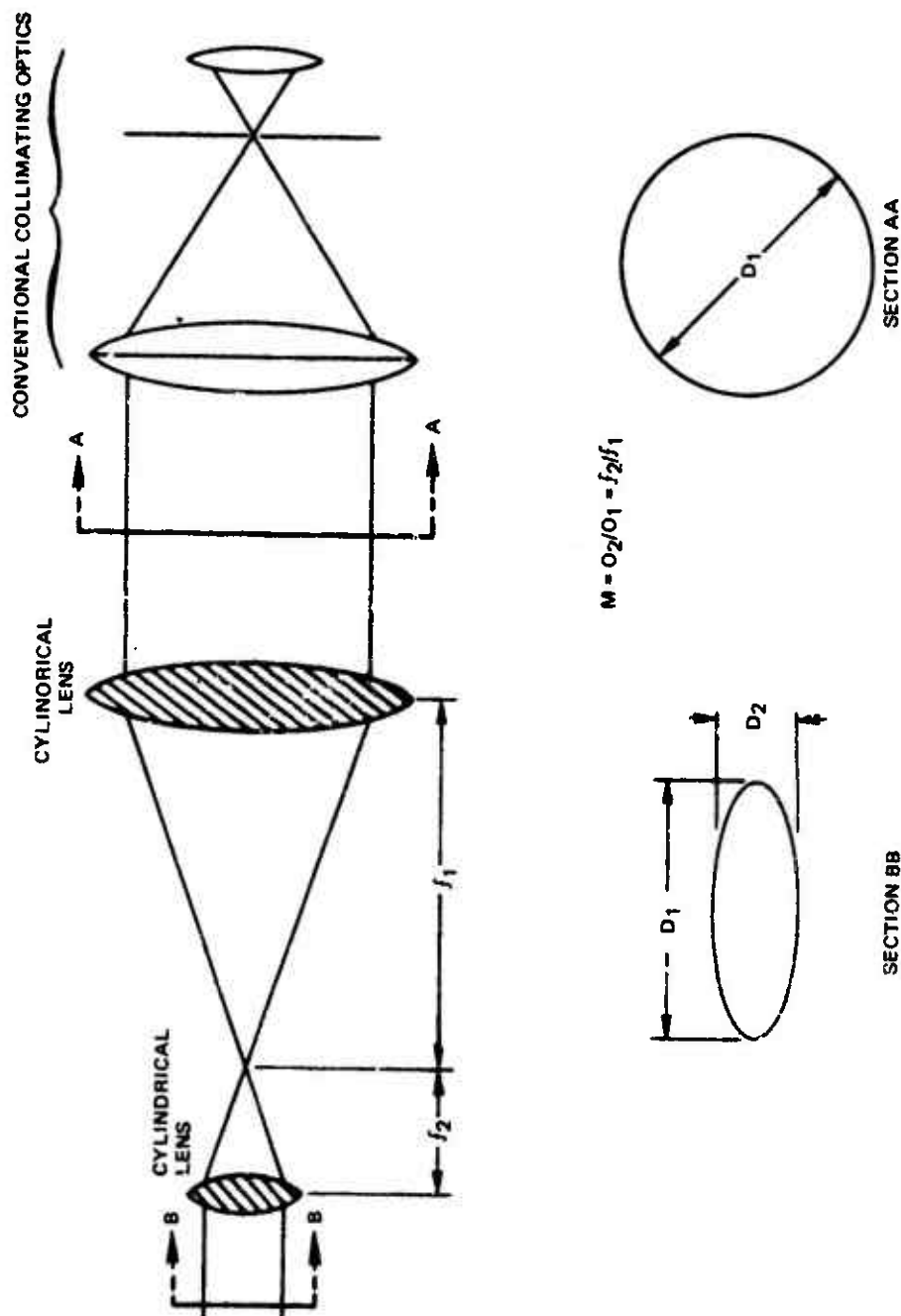
Fig. 21 THE USE OF CYLINDRICAL OPTICS TO COMPRESS THE ILLUMINATION BEAM IN ONE DIMENSION
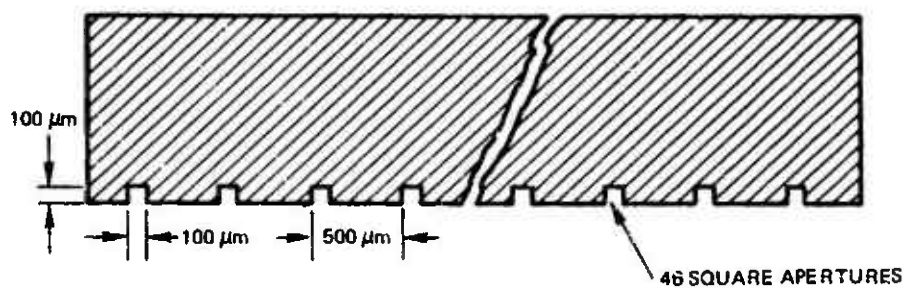
Fig. 22   TRANSMIT MASK FOR 46 CHANNEL CRYSTAL PHASE MODULATOR

The output surface of the masked crystal is located in the front focal plane of the transform lens, and the spatial Fourier transform of the array exists in the back focal plane (transform plane). The light intensity in the transform pattern is read by a scanning mirror readout system. The mirror scans a projected image of the transform past a slit in front of the photomultiplier so that the current out of the photomultiplier as a function of time corresponds to the light intensity in the transform plane as a function of the distance along the scan. The photomultiplier output is displayed on an oscilloscope.

The multi-channel crystal modulator can be considered as a linear phased-array antenna. The transform pattern of a linear array of isotropic radiators was given in Eq. (14). Since the crystal elements are rectangular, Eq. (14) must be multiplied by the element transform pattern. The power in the transform plane of the multi-channel crystal modulator is described by the equation:

$$|U(\xi,\eta)|^2 = A^2(ab)^2 \left[\frac{\sin\left(\frac{\pi a\xi}{\lambda f}\right)}{\left(\frac{\pi a\xi}{\lambda f}\right)}\right]^2 \left[\frac{\sin\left(\frac{\pi b\eta}{\lambda f}\right)}{\left(\frac{\pi b\eta}{\lambda f}\right)}\right]^2 \left[\frac{\sin\left[(M\pi\Delta X\xi)/\lambda f - \pi p\right]}{\sin\left[(\pi\Delta X\xi)/\lambda f - \pi p/M\right]}\right]^2 \quad (23)$$

where a = the width of the crystal elements in the X direction, and

b = the width of the crystal elements in the Y direction (for the present mask, a = b = 100 μm).

For the present crystal, there are 46 useful elements (M = 46), and therefore there are 46 Rayleigh beam positions between the grating lobes. A photograph of several adjacent beam positions is shown in Fig. 23. The width of the lobes obey Eq. (12) and the intensity at the crossing point between two adjacent beam positions (-4 dB) satisfies Eq. (23).
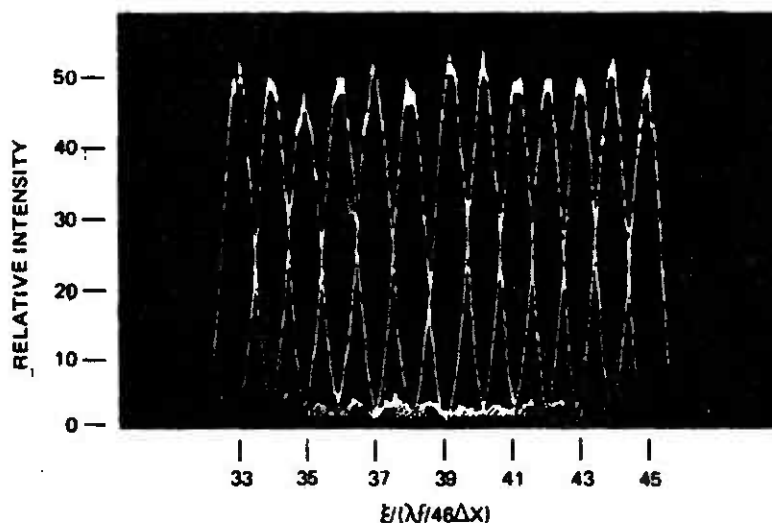
Fig. 23   ONE-DIMENSIONAL BEAM-STEERING RESULTS
USING THE MULTICHANNEL CRYSTAL MODULATOR
(SEVERAL ADJACENT RAYLEIGH BEAM POSITIONS
ARE SUPERIMPOSED ON ONE PHOTOGRAPH)

A photograph of all 46 beam positions is shown in Fig. 24. Unlike the MLM (Fig. 17), the intensity is fairly uniform for all of the beam positions. This is because the amplitude of the crystal elements is not a function of the applied phase modulation. In other words, the crystal acts as a piston modulator.

A photograph of the grating lobe structure is shown in Fig. 25. From Eq. (23), there are nine grating lobes under the main lobe of the element pattern.
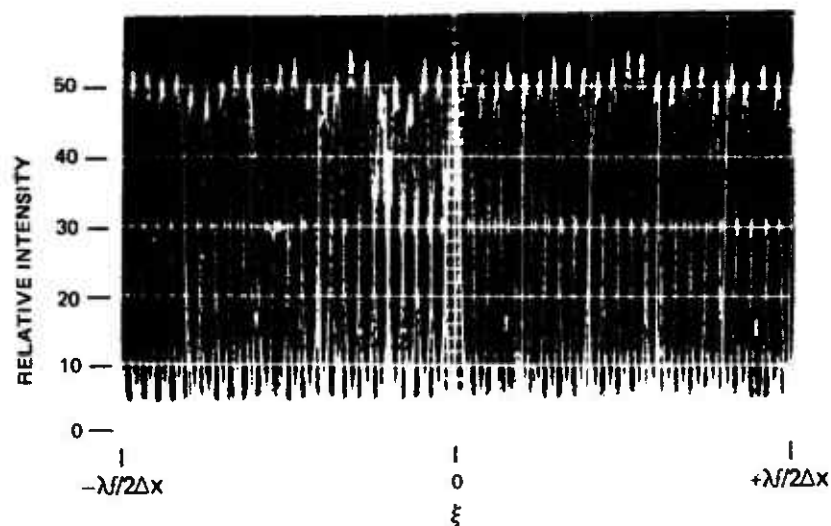
Fig. 24 RAYLEIGH BEAM POSITIONS OVER ENTIRE AMBIGUITY
INTERVAL FOR THE 46 CHANNEL CRYSTAL PHASE MODULATOR
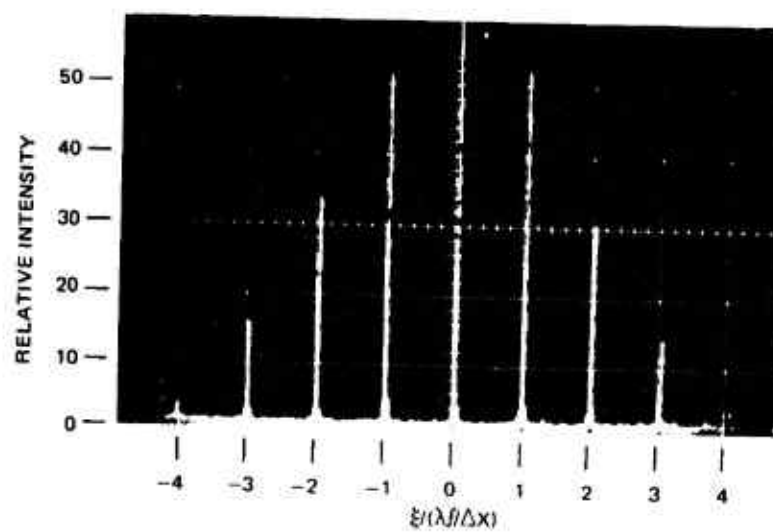
Fig. 25   GRATING LOBE STRUCTURE OF THE CRYSTAL MODULATOR
TRANSFORM PATTERN

6. TWO-DIMENSIONAL OPTICAL BEAM STEERING

As discussed in Section 3, the requirement for two-dimensional beam steering with a phased-array antenna is the capability of generating two-dimensional phase slopes across the antenna. When an appropriate optical system is employed, both the MLM and crystal modulators can be used to perform two-dimensional beam steering (in this case, only N elements are used from the N-by-N array). Two-dimensional beam steering has been successfully performed using the MLM. A description of the MLM system and results will be given in this section. Also, an optical system for performing two-dimensional beam steering with the crystal modulator will be described.

OPTICAL CONFIGURATION FOR TWO-DIMENSIONAL BEAM STEERING WITH THE MLM

Since the elements along each row of the MLM array are controlled by a single electrode, the phase of each of these elements is the same. Phase slopes parallel to the electrode structure are required in order to perform two-dimensional beam steering, and therefore only one element from each row can be used. A mask is used to block the light from all but the appropriate element. A typical mask is shown in Fig. 26a. For simplicity, a 20-by-20 array has been shown. For this example, the light is blocked from all but the first element in the first row, the eleventh element in the second row, etc. This thinned array can be used to obtain a two-dimensional tilt of the plane of equal phase as shown in Fig. 26b. The optical configuration for two dimensional beam steering with the MLM (Fig. 26c) is the same as for one-dimensional beam steering (Fig. 13) except that now the thinned array transmit mask is used. When the appropriate

(a) TRANSMIT MASK

(b) TWO-DIMENSIONAL PHASE SLOPE

(c) OPTICAL SYSTEM
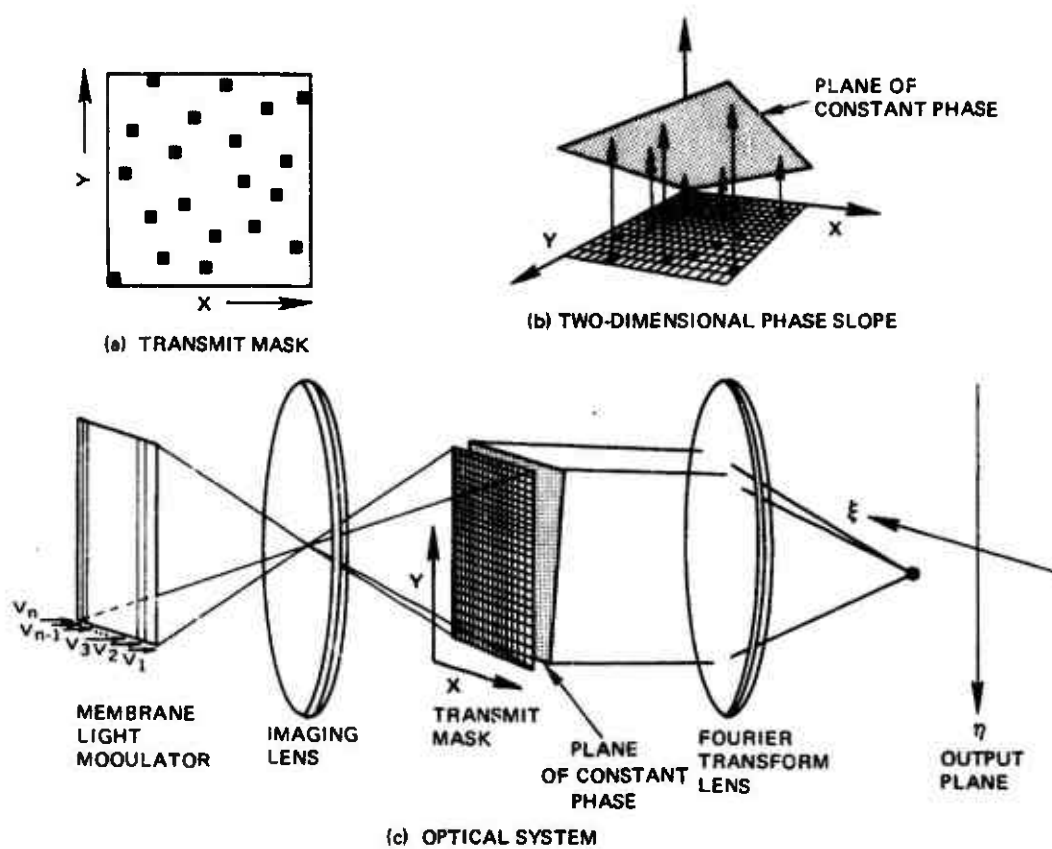
Fig. 26   TWO-DIMENSIONAL OPTICAL BEAM STEERING USING THE MLM

voltages are applied to the modulator electrodes, the beam from the thinned MLM array can be steered in two dimensions.

SELECTION OF THE ELEMENT LOCATIONS IN THE THINNED MLM ARRAYS

If independent access could be made to each element in the 100-by-100 MLM array, the beam could be steered into 10 000 Rayleigh resolvable beam positions. When the locations of the thinned array elements are chosen judiciously, this resolution of the whole array is maintained. One of the criteria used for selecting the best location of the elements in the thinned MLM array was that the resolution in the transform pattern of the entire 100-by-100 array should be maintained.

In order to avoid the observation of false beam positions, it is necessary to minimize the peak power in lobes other than the main grating lobes. The second criterion used for selecting the best location of the elements in the thinned array was that the sidelobe levels in the transform pattern should be as low as possible. For a perfect "thumbtack" response (i.e., the sidelobe power is uniformly spread over the two-dimensional ambiguity area), it can be shown that the average power in the sidelobes is approximately $1/N$ times the peak power in the main beam. For the thinned MLM array, $N = 100$ and therefore the average sidelobe level is 20 dB down from the main lobe peak. However, it is difficult to achieve a thumbtack response due to the periodicity of the array locations and the relatively small number of elements.

The lower limit of the peak sidelobe level for the thinned MLM arrays is determined by the requirement that only one element occur on each electrode. Therefore, the transform pattern along the ξ axis is described by a $(\sin \xi)/\xi$ distribution in the vicinity of the

main grating lobe. The peak intensity of the first side-lobe for this distribution is 13 dB down from the peak intensity of the main lobe. The goal therefore is to keep the peak intensity at any other point in the area between the grating lobes below this 13-dB level.

Equation (16) (which describes the transform pattern for a full two-dimensional array of point radiators) must be modified to the following form in order to describe a thinned array of isotropic radiators (ignoring a constant phase term):

$$U_a(\xi, \eta) = \sum_{m=0}^{M-1} A_m \exp(j\varphi_m) \exp\left(-jk[m\Delta X\xi + n(m)\Delta Y\eta]\right), \quad (24)$$

where $n(m)$ = the relative column location of the radiator in the mth row,

$\quad A_m$ = the amplitude of the radiator in the mth row,

$\quad \varphi_m$ = the phase of the radiator in the mth row, and

$\quad k$ = $2\pi/\lambda f$.

The transform pattern for the boresight beam of this thinned array can be found by letting the phase and amplitude of each radiator be equal (also $\Delta X = \Delta Y$ for the MLM):

$$U_a(\xi, \eta) = \sum_{m=0}^{M-1} \exp[-jk \Delta X (m\xi + n(m)\eta]. \quad (25)$$

Equation (25) can be solved in closed form for only a few simple arrangements of the input radiators. Using Eq. (25), a computer program has been written to calculate the power in the transform pattern for an arbitrary arrangement of the radiators in the thinned array. From the results of this program, the "best" orientation of the radiators can be chosen.

With a rather limited effort, no selection technique
has been found that is better than pseudo-random orienta-
tions of the elements in the thinned array. The resolution
of the entire array is maintained and the peak sidelobes
are about 10 dB down from the peak intensity of the main
lobe. Optical transmit masks for three different pseudo-
random orientations have been obtained.

A description of the technique used for selecting
the element locations for the thinned MLM arrays is given
in Appendix F.

TWO-DIMENSIONAL BEAM-STEERING RESULTS
USING THE MLM

A computer program has been written to generate
the voltages required for steering the beam of the thinned
MLM array to any place in the unambiguous transform
area. The row and column locations of the thinned array
elements and the desired locations of the MLM beam are
read into the computer program. The output from the
computer program is punched on paper tape in a format
that is compatible with the paper tape reader of the Digital-
Optical Hybrid Correlator.

Two-dimensional optical beam steering has been
performed using the three pseudo-random optical masks.
Photographs of the transform patterns for the three masks
are shown in Fig. 27. The transform pattern is at the
usual 45°, corresponding to the MLM array orientation
of 45°. The main grating lobe (the grating lobe at the cen-
ter of the element pattern) has been centered on these
photographs.

Due to the low light levels, a measurement of the
actual sidelobe levels in the transform plane could not
be made. However, several observations can be made
from the photographs of the transform pattern. First,
the light intensity in the area between the grating lobes is
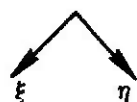
(a) RRC1 MASK

(b) RC1 MASK

Fig. 27   TRANSFORM PATTERN FOR THE THREE PSEUDO-RANDOM
TRANSMIT MASKS

- 58 -
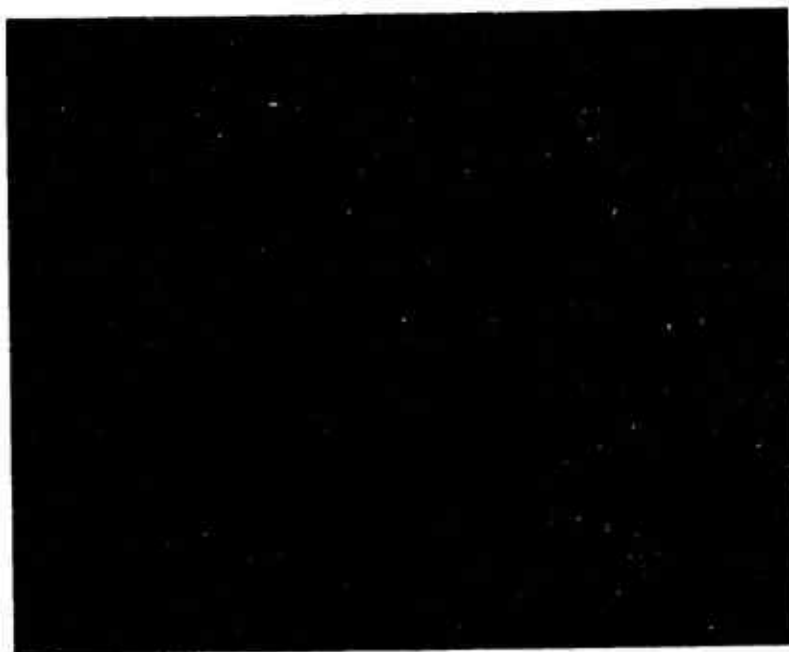
(c) R1 MASK

Fig. 27 TRANSFORM PATTERN FOR THE THREE PSEUDO-RANDOM TRANSMIT MASKS. (Cont'd)

fairly uniform and therefore approaches a thumbtack response. Also, the sidelobe patterns in the computer program plots (see Appendix F) compare very closely with the sidelobe patterns in the photographs. A dark line structure connecting the grating lobes is also evident in these photographs. This line structure corresponds to the ξ and η axes of the transform pattern (and its ambiguities) along which the transform pattern is described (in the vicinity of the grating lobes) by a $(\sin x)/x$ function. The first sidelobe of this distribution can be seen adjacent to the main grating lobes. Since the higher order sidelobes of this distribution are very low with respect to the light level in the area between the grating lobes, a dark line structure will be observed connecting the grating lobes in the ξ and η directions.

Typical beam steering results for one of the masks (Mask RRC1) are shown in Fig. 28. For this example, the beam was steered along the diagonal between the grating lobes. A number of comparisons between the steered beam and the boresight beam (when zero phase slope exists across the modulator) can be made:

1. The overall intensity in the unambiguous transform area of the steered beam is less than that of the boresight beam.

2. The intensity of the main steered lobe is lower than the intensity of the main boresight lobe.

3. The peak signal to peak sidelobe power ratio is lower in the steered beam.

4. The transform pattern of the steered beam does not look the same as the transform pattern of the boresight beam. Sidelobes occur at different places and the dark lines connecting the ambiguities are no longer as distinct.

(a) BORESIGHT BEAM POSITION
$(\xi, \eta) = (0, 0)$
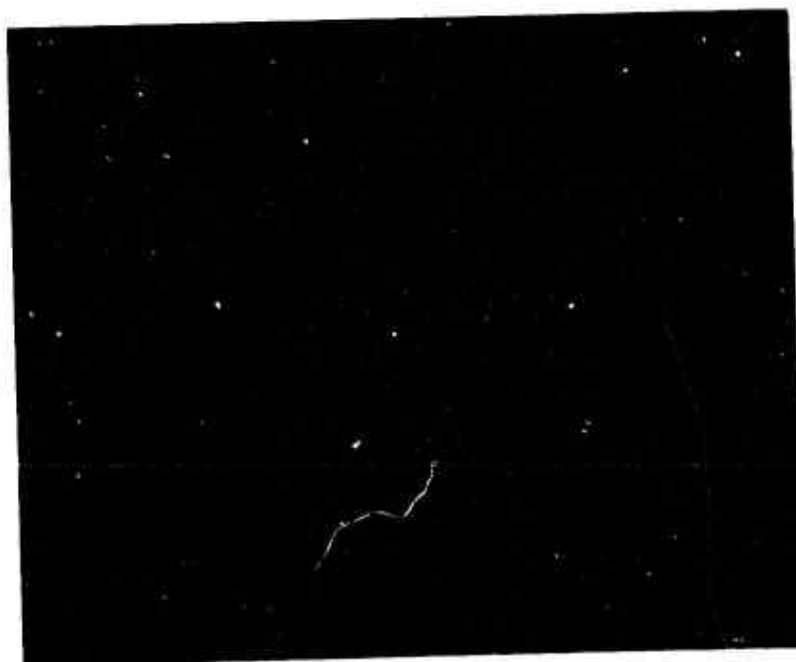
(b)   STEERED BEAM POSITION
$(\xi, \eta) = (2,2)$

NOTE: FOR THIS FIGURE, THE BEAM FROM MASK RRC1 HAS BEEN STEERED ALONG THE DIAGONAL
BETWEEN THE GRATING LOBES. THE MAIN GRATING LOBE (a) WAS CENTERED ON THE PHOTOGRAPH
AND FOR THE SUBSEQUENT PHOTOGRAPHS THE CAMERA POSITION WAS HELD RIGID.

Fig. 28   TWO-DIMENSIONAL BEAM-STEERING RESULTS USING A THINNED MLM ARRAY

- 61 -

(c) STEERED BEAM POSITION
$(\xi, \eta) = (10,10)$

(d) STEERED BEAM POSITION
$(\xi, \eta) = (25,26)$

Fig. 28   TWO-DIMENSIONAL BEAM STEERING RESULTS
USING A THINNED MLM ARRAY (cont'd)

- 62 -
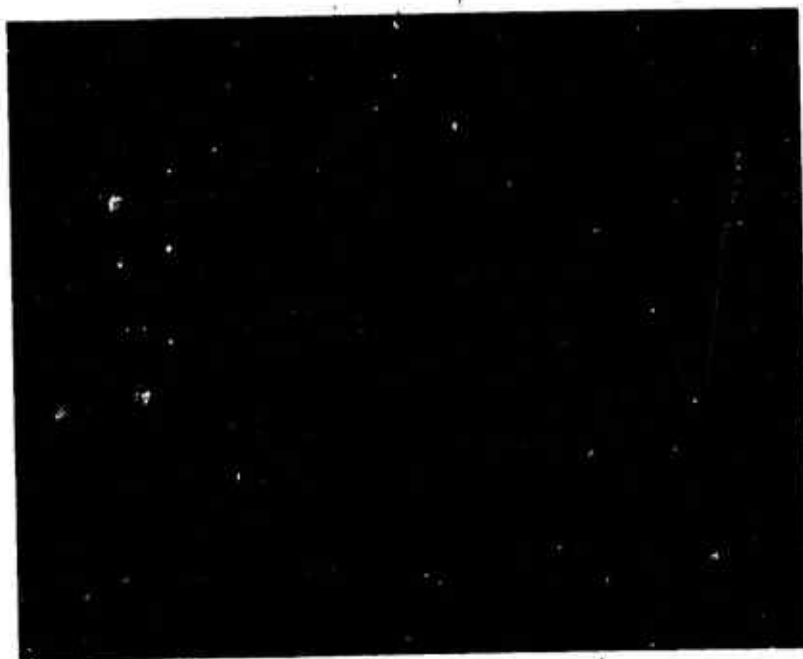
(e) STEERED BEAM POSITION
$(\xi, \eta) = (49, 49)$
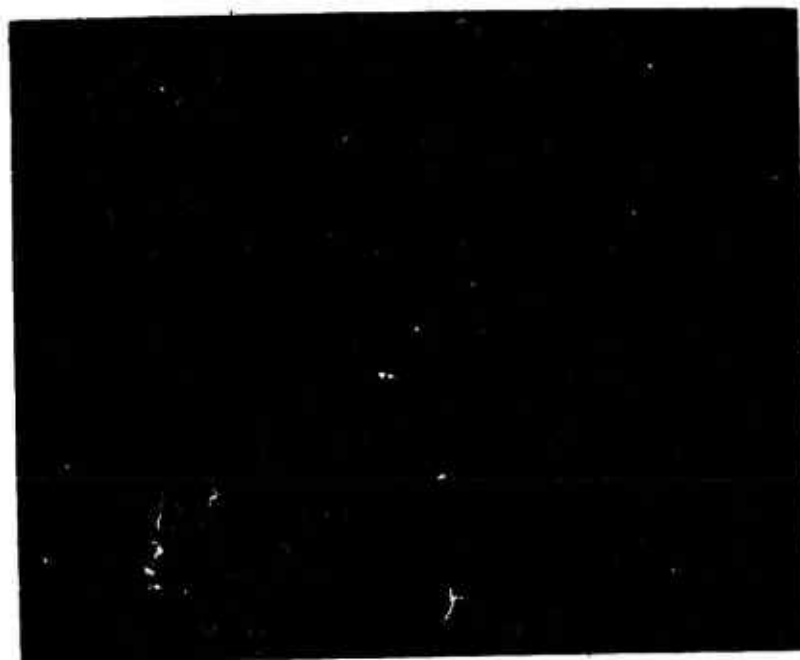
(f) STEERED BEAM POSITION
$(\xi, \eta) = (99, 99)$

Fig. 28   TWO-DIMENSIONAL BEAM STEERING RESULTS
USING A THINNED MLM ARRAY (cont'd)

5. The main lobe of the steered beam does not appear as distinct as the boresight lobe.

6. A residual boresight lobe is not noticeable when the beam is steered.

The observations listed as 1 through 5 are a result of the decreasing amplitude in the element pattern as higher voltages (phases) are applied to the MLM elements (discussed in Section 5). For a piston modulator (without this amplitude versus phase dependence), the transform pattern of the steered beam would be essentially identical to the boresight transform pattern. The observation listed as 6 above is an indication of a good alignment of the transmit mask.

TWO-DIMENSIONAL BEAM STEERING USING THE CRYSTAL MODULATOR

By using appropriate optics, a linear array of square radiators (corresponding to the masked crystal modulator) can be converted into a two-dimensional array as illustrated in Fig. 29. The array in Fig. 29a is demagnified in the X direction and magnitied in the Y direction to produce a compressed array of rectangular elements. As shown in Fig. 29b, this new array can be masked with a two-dimensional array of circular apertures in a configuration similar to the MLM. Now, thinned array masks similar to the masks designed for two-dimensional beam steering with the MLM can be used to perform two-dimensional beam steering with the crystal.

The optics required to obtain this compressed rectangular array are shown in Fig. 30. Cylindrical lenses are used to demagnify the array in the X direction by an amount:

$$m_X = \frac{l_2}{l_1} = \frac{f_2}{f_1}. \tag{26}$$

- 64 -

(a) LINEAR ARRAY OF SQUARE RADIATORS

(b) COMPRESSED ARRAY OF RECTANGULAR RADIATORS MASKED BY TWO-DIMENSIONAL ARRAY OF CIRCULAR APERTURES
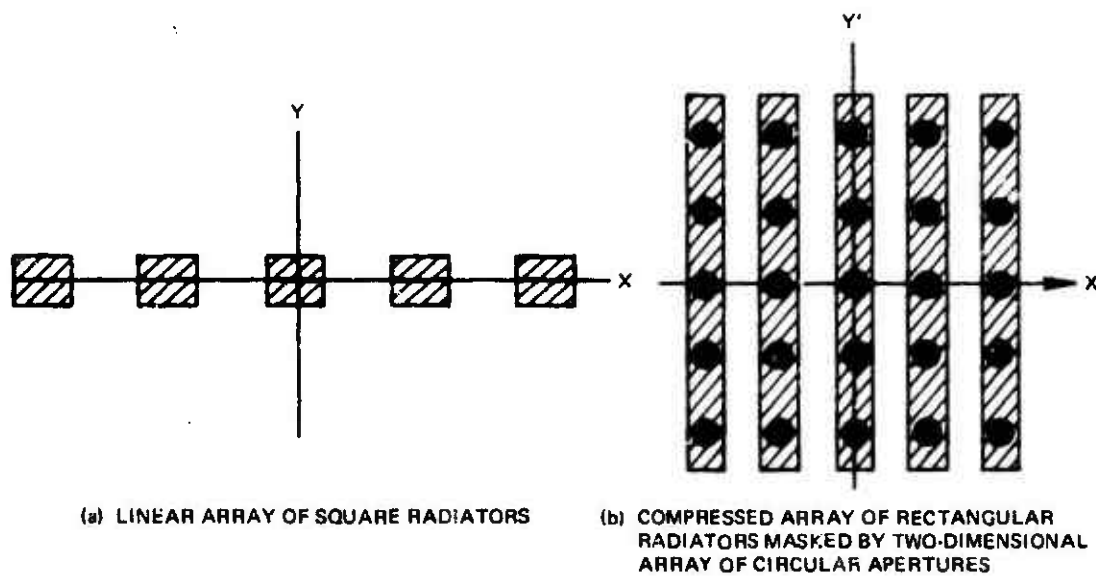
Fig. 29   CONVERSION OF A LINEAR ARRAY TO A TWO-DIMENSIONAL ARRAY

(a) TOP VIEW

$M_X = \ell_2/\ell_1 = f_2/f_1$

$M_Y = d_2/D \approx 2(1.22\lambda R/D)/D$

$\approx 5\lambda(f_1 + f_2)/D^2$

MASKED
CRYSTAL

THINNED ARRAY
MASK

(b) SIDE VIEW
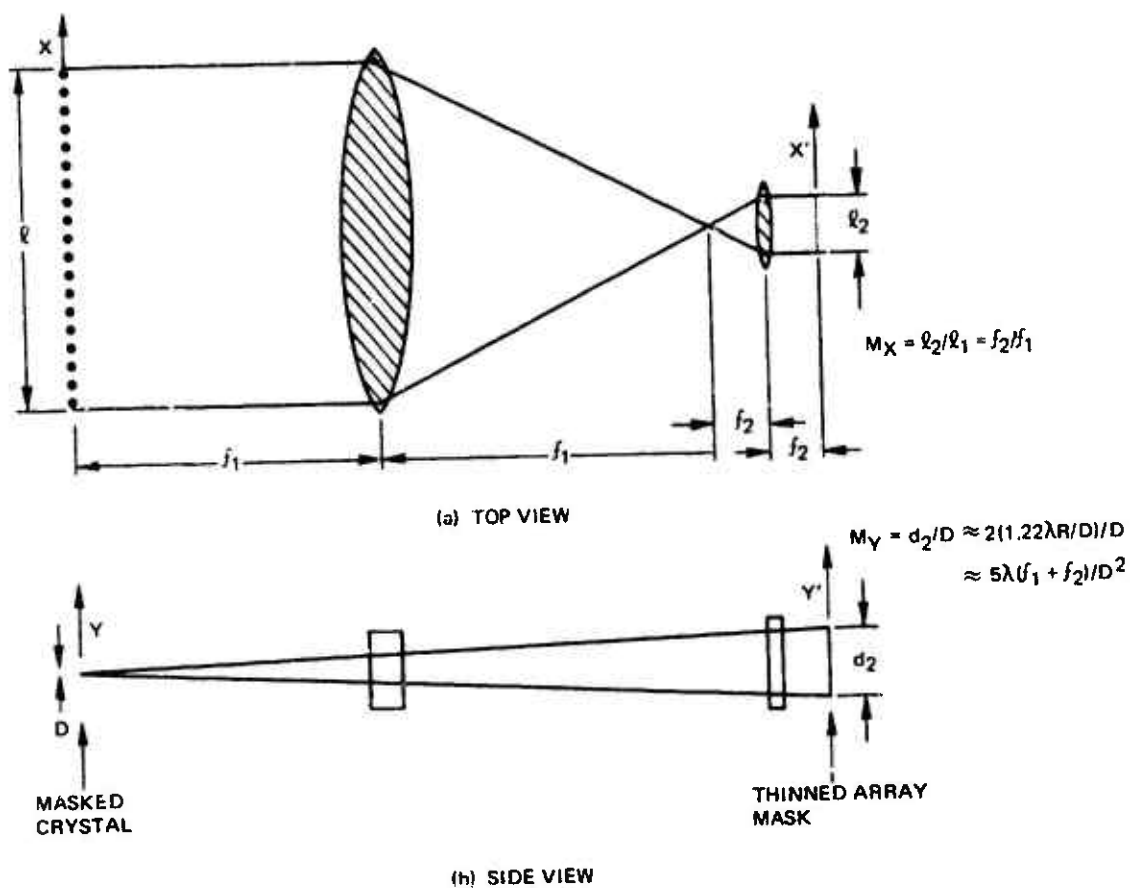
Fig. 30 ADDITIONAL OPTICS REQUIRED TO PERFORM TWO-DIMENSIONAL
BEAM STEERING WITH THE CRYSTAL MODULATOR

The natural divergence of the modulator elements results in a magnification in the Y direction of

$$m_Y = \frac{d_2}{D} \approx \frac{2(1.22 \frac{\lambda R}{D})}{D}$$

$$\approx \frac{5\lambda(f_1 + f_2)}{D^2} \, . \tag{27}$$

By choosing a proper set of focal lengths for the cylindrical lenses (f_1 and f_2), the resulting image is similar to Fig. 29b.

Since the crystal elements act like piston phase modulators, the amplitude/phase dependence that is characteristic of the MLM is not present. Therefore, the transform pattern of the steered beam should be essentially identical to the transform pattern of the boresight beam.

7. CORRELATION PROPERTIES OF AN OPTICAL PHASED ARRAY

The correlation properties of an optical phased array will be discussed in terms of the operations required to correlate a pulse doppler waveform. For a pulse doppler transmission, a set of single frequency pulses is transmitted and the echo phases for one range bin (pulse width) are determined. For a constant velocity target in a noise-free environment, there exists a linear phase slope across the return echoes (corresponding to the constant doppler frequency shift). The function of the correlator is to determine the phase slope (and therefore the velocity of a target) when noise is present. The phase slope corresponding to a given velocity is assumed. The correlation of the return echoes with this linear phase slope is given by:

$$C(V) = \sum_{m=1}^{M} A_m \, \exp(j\varphi_m) \, \exp\left(-j \frac{4\pi V m \Delta t}{\lambda_t}\right) . \quad (27)$$

where A_m = the amplitude of the mth echo,

φ_m = the phase of the mth echo,

V = the assumed velocity of the target,

Δt = the time between successive pulses (1/PRF), and

λ_t = the wavelength of the transmitted waveform.

An electronic system performs this correlation in a brute force manner by first rotating the vectors of the returned pulses by the phase of the assumed linear slope and then performing a vector addition of all the pulses. This is then repeated for every velocity bin that is investigated.

Preceding page blank   - 69 -

Notice that Eq. (27) is similar in form to Eq. (8) which describes the transform pattern for a linear phased array antenna (ignoring a uniform phase term). If ΔX is associated with Δt, and ξ is associated with V, then Eq. (8) can be interpreted as a correlation function. The phase of the mth echo is impressed on the mth radiator, and the spatial spacing of the radiators corresponds to the temporal spacing of the radar pulses. The position along the ξ axis in the transform plane corresponds to the velocity of the target. The optical system not only performs the correlation instantaneously, but also the correlation is performed simultaneously for all velocities.

The resolution and ambiguities of the pulse doppler waveform are the same as those already calculated in Section 3 for the phased array.

This correlation property can also be explained in terms of optical beam steering. When a linear phase slope corresponding to a constant velocity target exists across the phased array, the beam is steered an amount proportional to the target velocity.

Ideally, the amplitude (A_m) and phase (φ_m) of each radar pulse should be included in the correlation calculations (as shown in Eq. (27)). However, as discussed in Section 2, the MLM and crystal modulators are pure phase modulators. Therefore, the amplitude of the input data is hard limited. This results in the appearance of spurious signals and also a degraded signal-to-noise ratio (Ref. 6). Several techniques for maintaining amplitude and phase information with the MLM abd crystal modulators have been proposed but not yet implemented.

8. ONE-DIMENSIONAL RADAR SIGNAL PROCESSING

A digital-optical hybrid correlator which has the capability of processing pulse doppler and wideband radar signals has been developed based on the correlation properties of the MLM phased array. This hybrid system retains the flexibility of the digital technology for signal storage and registration and the speed of the coherent optical technology for performing the correlation arithmetic. Use of digital shift registers for signal storage results in a system capable of operation at data rates from DC through the modulator response time.

PULSE DOPPLER WAVEFORMS

The use of the digital-optical hybrid correlator to process pulse doppler waveforms is shown in Fig. 31. As discussed in Section 7, a linear phase slope exists across the return echoes for a constant velocity target in a noise-free environment. When the phases for a set of 100 pulses are time ordered across the 100 MLM rows, the output beam is steered an amount that is a function of the target velocity. For a real-life environment, the output pattern corresponds to the correlation of the input waveform with all the possible phase slopes (velocities).

The optical configuration for pulse doppler signal processing is the same as the optical configuration for one-dimensional beam steering that was described in Section 5 (Fig. 13). A block diagram of the receiver for window mode processing is shown in Fig. 32. For a pulse doppler transmission, the frequency switch is kept at one frequency and a set of 100 pulses is transmitted. The phases of the echo pulses are calculated for one range bin (pulse width), and then the square roots of these values are determined (since the MLM phase obeys a square
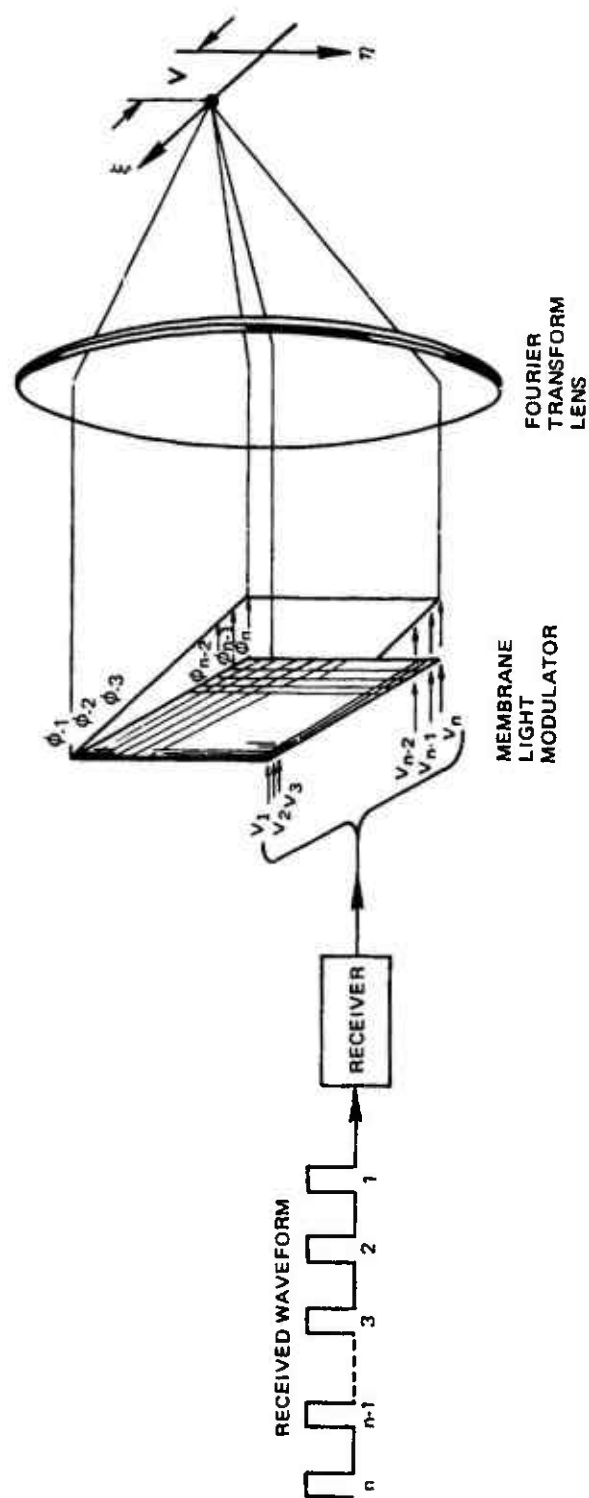
Fig. 31   PULSE DOPPLER SIGNAL PROCESSING WITH THE HYBRID CORRELATOR
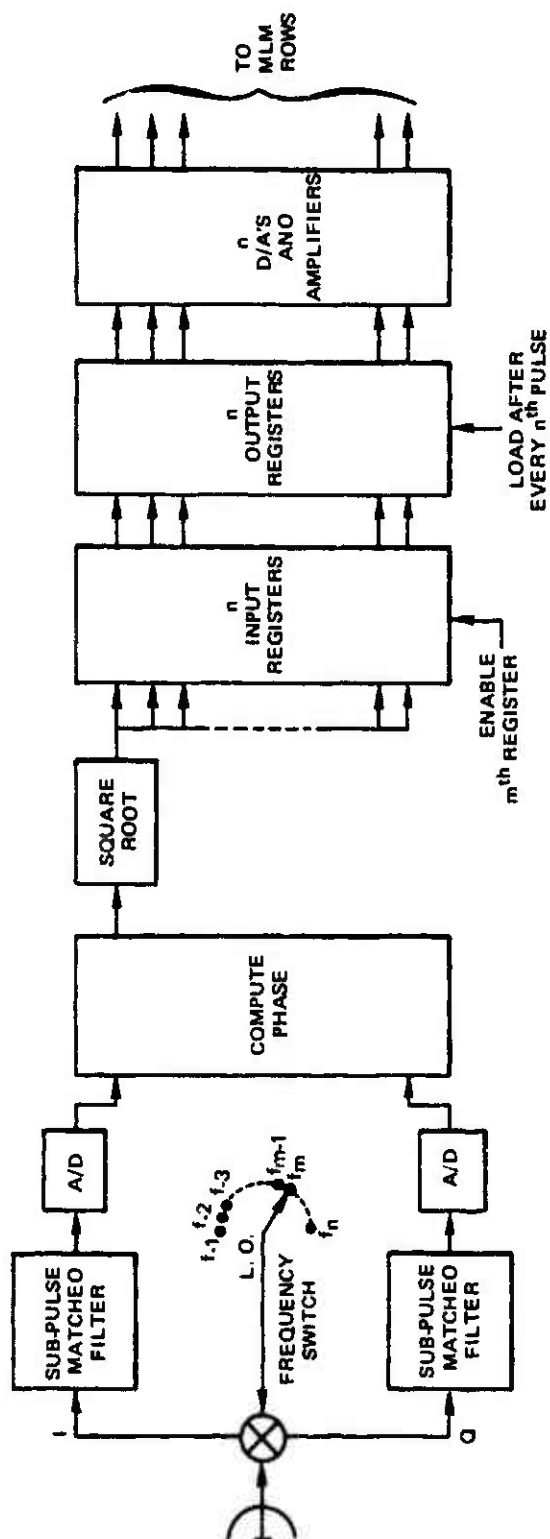
Fig. 32   BLOCK DIAGRAM OF THE RECEIVER FOR WINDOW MODE SIGNAL PROCESSING WITH THE HYBRID CORRELATOR

voltage law). These values are then loaded into the input registers and ordered according to the received time. After the phase values for all 100 pulses have been loaded into the input registers, they are transferred in parallel to the output registers, which are tied directly to the MLM rows via D/A converters and amplifiers.

The hybrid correlator has been used off-line to process window mode pulse doppler signals. For this case, the digital I and Q words are stored. The phase and MLM voltage values are then computed in non-real-time and stored on paper tape. The data can be read into the MLM registers using the paper tape reader of the hybrid correlator.

LINEAR-STEP FM WAVEFORMS

The hybrid correlator has also been used to process linear-step FM waveforms. In this mode, the 100 pulses are transmitted at different frequencies. The frequency of each successive pulse is a fixed frequency increment greater than the previous pulse. The receiver shown in Fig. 32 is used but now the frequency select switch is changed for each pulse. For a stationary point target in a noise-free environment, a linear phase slope across the return echoes exist that is a function of the target's position within the range cell. When this phase slope is impressed across the MLM, the output lobe position indicates the target's fine range. For a complex stationary target in a real-life environment, the output is the correlation of all phase slopes (fine ranges) with the input data. The resulting signature can be used to identify the target.

When this linear-step FM waveform is used for a moving target, the return phase is a function of both the target velocity and fine range. Since the doppler frequency is a function of the transmit frequency ($f_d = Vf_t/2C$), a constant-velocity point target will not generate a linear phase slope for a wide-bandwidth transmission.

The distortion can be compensated by appropriately adjusting the time of transmission of each pulse. For a linear-step FM waveform, the frequency of the nth pulse is given by:

$$f_n = [f_o + (n - 1) \Delta f],$$
(28)

where n $= 1, 2, \ldots, 100,$

f_o = the transmit frequency of the first pulse, and

Δf = the frequency increment between pulses.

To compensate for the wide bandwidth doppler distortion, the transmission time for the nth pulse is given by:

$$t_n = \left(\frac{f_o}{f_o + (n - 1) \Delta f} \right) n \Delta t$$

$$\approx \left(1 - \frac{(n - 1) \Delta f}{f_o} \right) n \Delta t,$$
(29)

where Δt = the pulse spacing at the frequency f_o.

REAL-TIME SEARCH MODE PROCESSOR

The high speed of the MLM allows it to be used as a real-time signal processor. A block diagram of the real-time receiver for the hybrid correlator is shown in Fig. 33. Associated with each row of the MLM is a separate phase detector, A/D converter, shift register delay line, D/A converter, and amplifier. The shift register delay lines for each channel are used for signal storage and registration so that at any given time the phase values across the MLM rows correspond to the phase values for one range cell. A simple change in the clock frequency allows the system to be operated at data rates from DC up to the frequency at which the modulator response time becomes a limiting factor.

Since the MLM can accept a new set of input data approximately every microsecond, a new set of output data is available every microsecond. A high-speed linear diode array is necessary in the putput plane in order to read the output at an equivalent rate. Associated with each diode would be a threshold detector and buffer register.
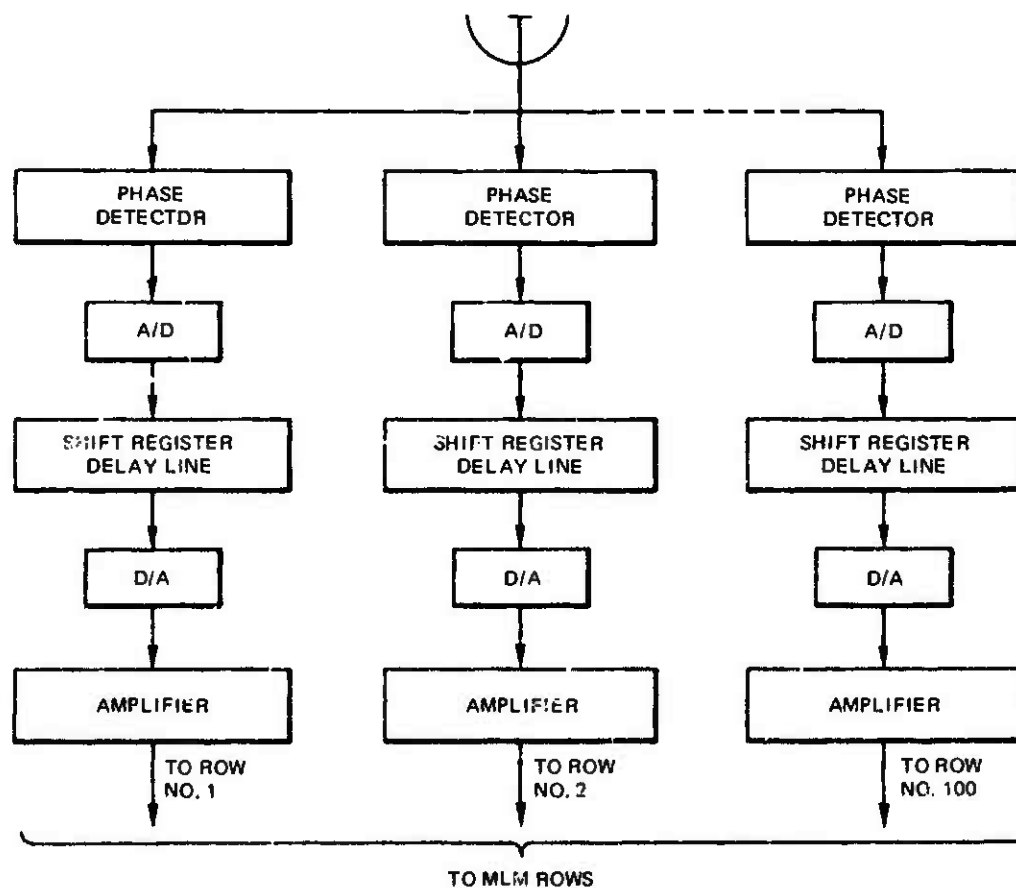
Fig. 33   BLOCK DIAGRAM OF A REAL-TIME RECEIVER FOR THE HYBRID CORRELATOR

9. TWO-DIMENSIONAL RADAR SIGNAL PROCESSING

Just as the optical system can be used to perform two-dimensional beam steering (Section 6), the hybrid correlator can also be used to perform two-dimensional correlation of radar signals. Consider a frequency diversity pulse doppler waveform consisting of 100 pulses where the frequency of the mth pulse is given by:

$$f_m = f_o + n(m) \, \Delta f \, . \tag{30}$$

In this case the frequency ordering is no longer linear (as was the case in linear-step FM discussed in Section 8). However, each frequency in the set of 100 pulses is different, so that the whole bandwidth is covered uniformly. For a point target in a noise-free environment, a linear phase slope with respect to frequency exists across the return echoes that is a function of the target's fine range. Also a linear phase slope with respect to time exists across the return echoes that is a function of the target's velocity (ignoring, for now, the doppler frequency dependence on transmit frequency). In other words, a two-dimensional phase slope exists across the frequency/time plane. The function of a correlator is to determine this two-dimensional phase slope and therefore the velocity and fine range of the target. The two-dimensional phase slope corresponding to a given velocity and fine range is assumed. The correlation of the return echoes with this phase slope is given by:

$$C(V, R) = \sum_{m=1}^{M} A_m \exp(j\varphi_m) \exp\left(-\frac{j4\pi \, V \, m\Delta t}{\lambda_t}\right) \exp\left(\frac{j4\pi \, n(m) \, R\Delta_t}{c}\right), \tag{31}$$

where A_m = the amplitude of the mth echo,

φ_m = the phase of the mth echo,

- 77 -

V = the assumed velocity of the target,

Δt = the time increment between pulses,

λ_t = the wavelength of the transmitted waveform,

R = the assumed fine range of the target,

Δf = the frequency increment, and

c = the velocity of light.

Notice that this equation is similar in form to Eq. (24), which describes the transform pattern of a thinned array. When the associations are made:

$$\Delta X \rightarrow \Delta t ,$$

$$\xi \rightarrow V ,$$

$$\Delta Y \rightarrow \Delta f , \text{ and}$$

$$\eta \rightarrow R , \tag{32}$$

Eq. (24) can be interpreted as a two-dimensional correlation function. The phase of the mth echo is impressed on the mth radiator, so that the spacing of the radiators in the X direction corresponds to the relative transmit time of the pulses and the spacing of the radiators in the Y direction corresponds to the relative frequency of the pulses. The position along the ξ axis in the transform plane corresponds to the velocity of the target, and the position along the η axis in the transform plane corresponds to the fine range of the target. The optical system not only performs the correlation instantaneously, but also the correlation is performed simultaneously for all velocities and fine ranges. Figure 34 depicts this two-dimensional signal processing capability of the hybrid correlator.

The doppler frequency dependence on transmit frequency can again be compensated for by appropriately altering the transmit time of the pulses. The new transmission time for the mth pulse is given by:

(a) TRANSMIT MASK (FOR 20 PULSES)
MATCHES TIME-FREQUENCY TRANSMIT CODE

(b) TWO-DIMENSIONAL STEERING

(c) OPTICAL SYSTEM
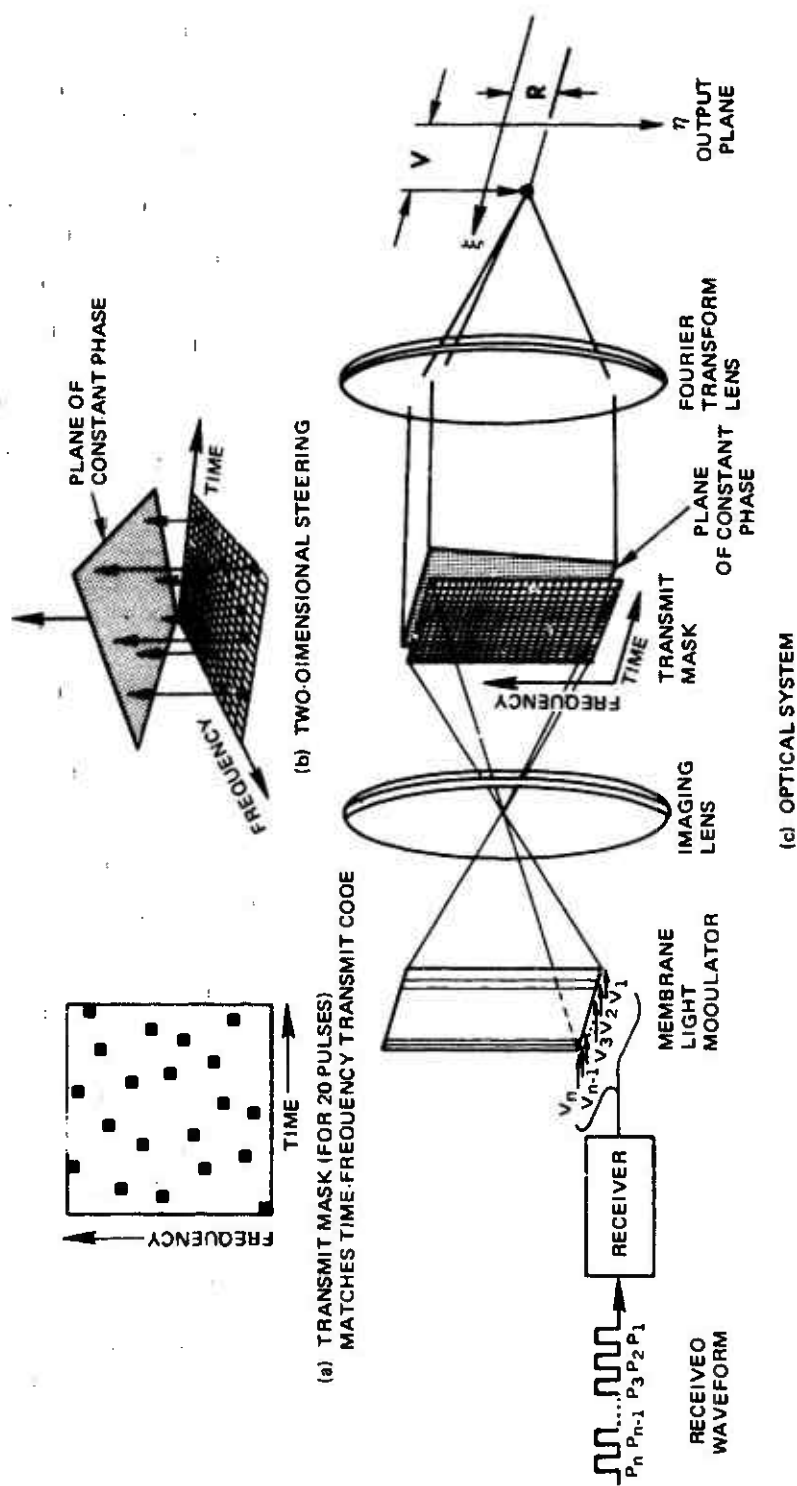
Fig. 34 TWO-DIMENSIONAL RADAR SIGNAL PROCESSING USING THE HYBRID
CORRELATOR

$$t_m = m \left(\frac{f_o}{f_o + n(m)\Delta f} \right) \Delta t_o , \tag{33}$$

where Δt_o = the time increment at f_o.

When the time-frequency code of the radar wave-
form is determined judiciously, the velocity and fine
range resolution of the full time-bandwidth can be main-
tained. This is analogous to the selection of an appro-
priate mask for two-dimensional beam steering which
maintains the resolution of the entire array. Also, the
sidelobes that are obtained from the two-dimensional
beam-steering masks are the sidelobes associated with
the ambiguity diagram of the radar waveform. Thus,
the "best" masks that were obtained for two-dimensional
beam steering will also be the best time-frequency code
for the radar waveforms. The successful two-dimensional
beam-steering results (Section 6) indicate the feasibility of
using the hybrid correlator for two-dimensional radar sig-
nal processing.

For window-mode processing, the receiver shown
in Fig. 32 is used again. Now, the frequency selector
is switched to the appropriate frequency for each pulse.

The ultimate capability of the hybrid correlator
would be to process two-dimensional waveforms in a
real-time search mode. Since the MLM can accept a
new set of input data every microsecond, a new set of
correlated data occurs every microsecond. The corre-
lator is now limited by the speed at which the two-
dimensional field of output data can be interrogated. A
suitable means is not currently available for interrogat-
ing the two-dimensional data plane at megahertz rates.
A high-speed two-dimensional array of photodiodes
followed by threshold circuits and amplifiers appears
to offer the most promise.

REFERENCES

1. L. E. Kinsler and A. R. Frey, Fundamentals of Acoustics, John Wiley and Sons, New York, 1950, p. 92.

2. F. R. Reizman, "Two-Dimensional Optical Phase Modulator Addressed by an Electron Beam," IEEE Transactions on Electron Devices (to be published).

3. J. F. Nye, Physical Properties of Crystals, Oxford University Press, 1964.

4. P. V. Lenzo, E. H. Turner, E. G. Spencer, and A. A. Ballman, "Electro-Optic Coefficients and Elastic-Wave Propagation in Single-Domain Ferroelectric Lithium Tantalate," Applied Physics Letters, Vol. 8, No. 4, 15 February 1966, pp. 81-82.

5. P. V. Lenzo, E. G. Spencer, and K. Nassau, "Electro-Optic Coefficients in Single-Domain Ferroelectric Lithium Niobate," Journal of the Optical Society of America, Vol. 56, No. 5, May 1966, pp. 633-635.

6. J. J. Jones, "Hard-Limiting of Two Signals in Random Noise," IEEE Transactions on Information Theory, January 1963, pp. 34-42.

7. F. D. Bloss, Optical Crystallography, Holt, Rinehart, and Winston, New York, 1961.

8. N. H. Hartshone and A. Stuart, Practical Optical Crystallography, American Elsevier Publishing Company, New York, 1964.

9. J. W. Goodman, Introduction to Fourier Optics, McGraw-Hill Book Company, New York, 1968.

10. M. Born and E. Wolf, Principles of Optics, Pergamon Press, New York, 1964, p. 441.

BIBLIOGRAPHY

1. D. G. Grant, R. A. Meyer, and D. N. Qualkinbush, "An Optical Phased Array Beam Steering Technique," Proceedings of the 1971 Electro-Optic System Design Conference, New York, September 1971.

2. R. A. Meyer, "Optical Beam Steering using a Multi-Channel Lithium Tantalate Crystal," Applied Optics, Vol. 11, No. 3, 1972, pp. 613-616.

3. K. Preston, "An Array Optical Spatial Phase Modulator," IEEE International Solid State Circuits Conference, Philadelphia, February 1969.

4. K. Preston, "The Membrane Light Modulator and its Application in Optical Computers," Optica Acta, Vol. 16, No. 5, 1969, pp. 579-585.

5. F. Reizman, "An Optical Spatial Phase Modulator Activated by Optical Signals," The 1969 Advisory Group on Aerospace Research and Development Symposium, Oslo, Norway, September 1969.

6. K. Preston, "A Coherent Optical Computer System using the Membrane Light Modulator," IEEE Transactions on Aerospace and Electronic Systems, Vol. AES-6, No. 4, July 1970, pp. 458-467.

ACKNOWLEDGMENTS

Preceding page blank

APPENDIX A

DEFLECTION CHARACTERISTICS OF THE MEMBRANE LIGHT MODULATOR

SUMMARY

A mathematical model for the deflection character-istics of the Membrane Light Modulator is described in this appendix. A power series solution has been obtained which describes the static deflections of the membrane as a func-tion of applied voltage for small deflections. The signifi-cant conclusions obtained from this analysis are:

1. Deflection is proportional to the square of the applied voltage (for small deflections only).

2. Maximum stable deflection is 44% of the initial separation and is independent of the dimen-sions.

3. If it is desired to utilize a 25% deflection, a further increase of only 10% in voltage will cause instability (beyond which the membrane will pull down onto the fixed electrode).

MATHEMATICAL MODEL

The cross-section of an MLM element is shown in Fig. A-1. The collodion membrane which is coated with a conducting-reflecting coating is stretched over a cylin-drical well of radius R_0 and depth D. The initial tension of the membrane is T. The element possesses circular symmetry about the z axis and therefore cylindrical coordinates are used.

When a voltage V is applied between the mem-brane and the electrode, the membrane deflects to a new

Preceding page blank
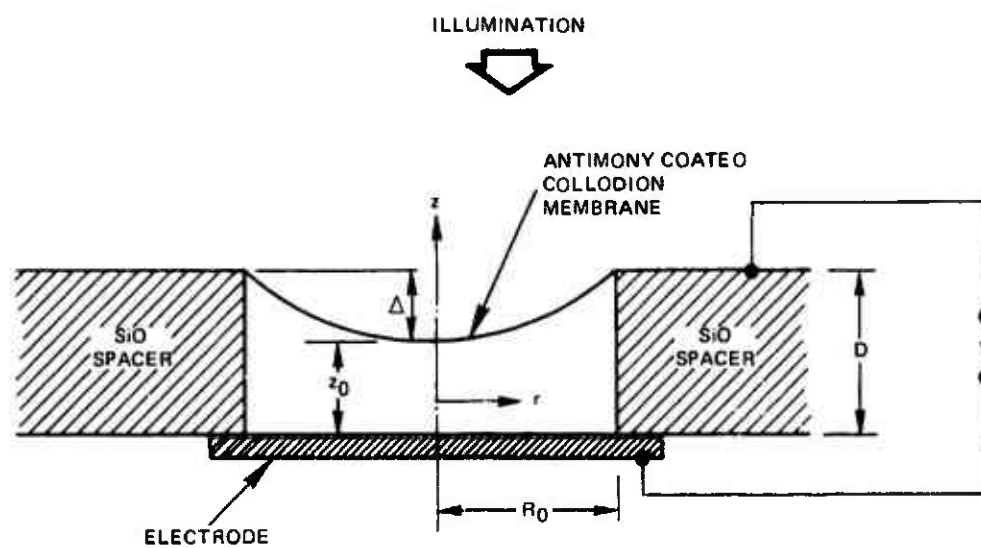
Fig. A-1   CROSS SECTION OF AN MLM ELEMENT

static position. The maximum deflection (Δ) occurs at the center of the element. We are interested in finding the deflection Δ as a function of the applied voltage V.

Four assumptions are made:

1. The membrane has negligible stiffness; i.e., only tension acting tangentially need be considered.

2. For the small D/R_0 ratios in the practical case, the tension T may be considered a constant.

3. For these small D/R_0 ratios, dz/dr is small compared to 1, permitting a simplified expression for the curvature.

4. Electrostatic fringing or end effects may be neglected.

From the "hoop-tension" formula in mechanics, a membrane is in equilibrium when the product of tension and curvature is equal to the radial pressure. The radial pressure in this case is given to a good approximation by the parallel plate capacitor expression, since electrostatic fluxlines are always normal to the electrodes. Therefore, at any point on the membrane, the electrostatic pressure is (in MKS practical units):

$$p = \frac{V^2 \epsilon}{2z^2} \quad \text{newtons per square meter,} \qquad (A-1)$$

where V = voltage applied between the membrane and the bottom electrode

  z = electrode separation in meters

  ϵ = permittivity = $\frac{1}{36\pi} \times 10^{-9}$ F/m.

- 89 -

The membrane possesses a double curvature. The total curvature in such a case is the sum of the curvature in orthogonal directions. In rectangular coordinates, curvature along the x direction is given by:

$$\text{curvature} = \frac{d^2z/dx^2}{\left[1 + (dz/dx)^2\right]^{3/2}} \qquad (A-2)$$

For a relatively flat surface, the denominator is approximately unity so that d^2z/dx^2 suffices. Thus, the total curvature for a surface that is curved with respect to y as well as x is simply:

$$\text{total curvature} = \left(\frac{\partial^2 z}{\partial x^2}\right) + \left(\frac{\partial^2 z}{\partial y^2}\right) \qquad (A-3)$$

The corresponding expression in cylindrical coordinates may be determined by noting that Eq. (A-3) is the Laplacian operator or ∇^2 in rectangular coordinates. Its equivalent in cylindrical coordinates is:

$$\text{curvature} = \frac{1}{r}\frac{\partial}{\partial r}\left(r\frac{\partial z}{\partial r}\right) + \frac{1}{r^2}\frac{\partial^2 z}{\partial \theta^2} \ . \qquad (A-4)$$

In our model, due to symmetry, there is no variation with θ. Hence,

$$\text{curvature} = \frac{1}{r}\frac{d}{dr}\left(r\frac{dz}{dr}\right) = \frac{d^2z}{dr^2} + \frac{1}{r}\frac{dz}{dr} \ . \qquad (A-5)$$

For a membrane tension of T N/m, the "hoop tension" equation becomes:

$$\frac{d^2z}{dr^2} + \frac{1}{r}\frac{dz}{dr} = \frac{V^2\epsilon}{2Tz^2} = \frac{K}{z^2} \ , \qquad (A-6)$$

where $K = V^2\epsilon/2T$.

- 90 -

SOLUTION

The solution of Eq. (A-6) will give the membrane deflection versus r for various values of K. This is a non-linear differential equation with no obvious closed form solution. The first five terms of the power series solution of Eq. (A-6) is:

$$z = a \left[1 + \frac{Kr^2}{4a^3} - \frac{1}{32}\left(\frac{Kr^2}{a^3}\right)^2 + \frac{1}{144}\left(\frac{Kr^2}{a^3}\right)^3 - \frac{1}{520}\left(\frac{Kr^2}{a^3}\right)^4 + \dots \right] . \quad (A-7)$$

The coefficient of the last term is approximate. There is no recognizable closed form which will give this succession of coefficients, an expected situation in view of the complexity of the differential equation. When the boundary condition that $z = z_0$ at $r = 0$ is inserted into Eq. (A-7), the arbitrary coefficient is found to be $a = z_0$ (where $z_0 = D - \Delta$).

What we are particularly interested in is not the equation for the full membrane, but rather the spacing at the center (z_0). We may therefore, insert into Eq. (A-7) the boundary condition $z = D$ at $r = R_0$:

$$D = z_0 \left[1 + \frac{KR_0^2}{4z_0^3} - \frac{1}{32}\left(\frac{KR_0^2}{z_0^3}\right)^2 + \frac{1}{144}\left(\frac{KR_0^2}{z_0^3}\right)^3 - \frac{1}{520}\left(\frac{KR_0^2}{z_0^3}\right)^4 + \dots \right) .$$

$$(A-8)$$

This, then is the final equation relating z_0 to K for a given R_0 and D.

NUMERICAL RESULTS

From Eq. (A-8), it is seen that the series (within the brackets) is fully determined by the value of KR_0^2/z_0^3. Hence, one approach to numerical results is to assume a value for KR_0^2/z_0^3, sum the terms in the series, and then

solve for z_o. From the assumed value of KR_o^2/z_o^3 and the solved value of z_o, K may now be determined. This process works well for small values of KR_o^2/z_o^3 (corresponding to a large z_o or small deflection) where the series converges rapidly. However, for larger deflections, five terms in the series are insufficient for accurate results and the method fails. Even if one were to expend the considerable labor necessary to obtain a few additional coefficients, it would still be impossible to determine the maximum stable deflection with any precision. Consequently, a computer numerical solution of Eq. (A-6) was sought, using the boundary condition $D = 1 \mu m$ and $R_o = 18.5 \mu m$.

The computer approach was as follows: A value of K is assumed, and a corresponding value for z_o is guessed. From symmetry, the first derivative of z at r = o is $z_o' = o$. From Eq. (A-7), the second derivative is $z_o'' = K/2z_o^2$. Using these initial values, the differential equation is solved numerically to give a value for z at $r = R = 18.5 \mu m$. If this value is other than $z = 1 \mu m$, a new value for z_o is guessed. Finally a value for z_o is obtained for which z = 1 at r = 18.5. This process is repeated for increasing values of K until a value for K is reached where the boundary condition is satisfied over an interval of z_o. At this point, the curve of deflection versus K is vertical and is, therefore, the limit of stability. For attempted solutions for greater values of K, it is found that z > 1 at r = 18.5 regardless of the choice of z_o. A plot of deflection (Δ) is shown in Fig. A-2.

Equation (A-8) may be rewritten in the following form:

$$\frac{D}{z_o} = 1 + \frac{KR_o^2}{4\left(\frac{z_o}{D}\right)^3 D^3} - \ldots\ldots\ldots \qquad (A-9)$$
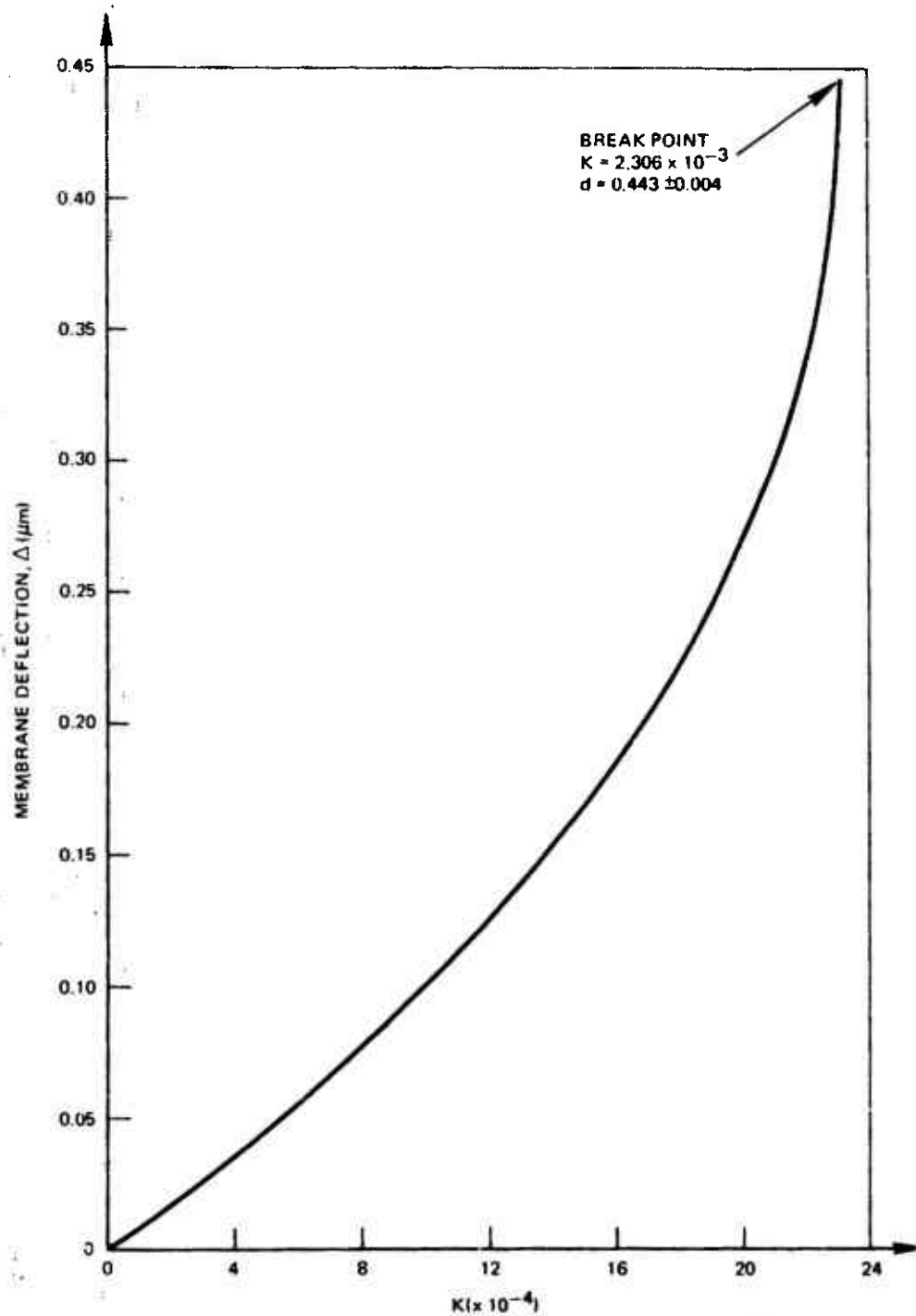
Fig. A-2   MEMBRANE DEFLECTION VERSUS K $(K = V^2 \epsilon / 2T)$

It is evident that the ratio z_0/D (and, therefore, the fractional deflection Δ/D) is completely determined by KR_0^2/D^3. Therefore, the plot of Fig. A-2 is valid for other values of R_0 and D (provided the assumptions are still satisfied) if the ordinate is now considered to be Δ/D and the abscissa $K(R/18.5)^2/D^3$.

APPENDIX B

HYBRID CORRELATOR ELECTRONICS

A block diagram of the Hybrid Correlator electronics has been described in Section 4 (Fig. 12). A more detailed description of some of the components in this block diagram will be given in this appendix including the protection electronics that were fabricated to keep the MLM elements from bottoming out. The modifications of the MLM electronics required for beam steering with the crystal will also be discussed. Finally, a description of the scanning mirror readout system will be given.

MLM BEAM-STEERING ELECTRONICS

A linear phase slope must be impressed across the MLM rows in order to steer the beam of this phased array antenna in one dimension. The Beam Position Generator (BPG) or a digital computer can be used to generate the appropriate voltages for each row of the MLM in order to obtain these linear phase slopes. The MLM phase dependence on the square of the applied voltage must be considered in making these calculations.

An M-460 digital computer can be used to generate the voltages required to steer the beam into the 100 Rayleigh resolvable beam positions of the MLM array. The voltage words are loaded sequentially into the input registers of the correlator electronics in the following manner. First a data request signal is sent to the computer (via the computer control electronics in Fig. 12). When ready, the computer returns a data acknowledge pulse to the computer control box and data for the first row of the MLM to the input register. The data acknowledge pulse is used to strobe the data into the registers. After the 100th data request and data acknowledge, an "external function" pulse is sent by the computer which is used to transfer the data into the storage register and clear the input register.

- 95 -

An interrupt line, an interrupt acknowledge line, and a number of data lines are also connected to the computer for the purpose of communicating with the computer. The data lines are set to a desired code (via front panel toggle switches) which will tell the computer the desired transmission mode.

As discussed in Section 8, the digital computer is used off-line to determine the phases (and also the required MLM voltages) of the radar pulses. Radar data from the computer can be accepted continuously. With a computer output rate of one word every 50 μs, it will take 5 ms to load the MLM for one set of data. A "stop" switch is also available which allows a set of data to be held on the MLM for detailed study.

The data generated by the M-460 can be recorded on 7-level paper tape. The first 6 bits are used for the MLM voltage data and bit 7 is used for the load pulse (external function of computer). 100 lines of data on the paper tape are required corresponding to the 100 rows of the MLM. Bit 7 is punched in line 101. This bit is used to load the data into the output register (and clear the input register) and also can be used to stop the tape reader after each block of data. The other 6 bits in this line are used as a code for the next set of data.

The control logic for the paper tape reader was built to allow a great deal of flexibility in the mode of operation. The modes that are used most often are listed below:

1. Tape Run. In the tape run mode, the reader runs continuously at its maximum speed of 625 lines per second (which results in approximately 6 blocks of data per second). It can be made to stop after any of the blocks of data or at any of the codes. (The desired code is selected via toggle switches on the front panel.)

2. <u>Block Rate Control</u>. The rate at which blocks
are read by the tape reader can be controlled in the Block
Rate Control Mode. The block rate can be varied from 6
blocks/second to 1 block every 10 seconds. In this mode
the 100 lines of a block are read at a 625 line per second
rate and then the reader stops at the end of the block for
the desired length of time before reading the next block of
data. This block reading can be stopped after any block
or at any of the code words.

3. <u>Single Block Load</u>. The "momentary" switch
allows single blocks to be loaded.

As discussed in Section 6, a PL/I computer pro-
gram has been written (for use on the IBM 360/91) to gen-
erate the voltages required for steering the beam from
the thinned MLM arrays in two-dimensions. The output
from this computer program is punched on paper tape in
a format which is compatible with the paper tape reader.

In order to provide a fast beam-stepping mode, a
special purpose digital package, called the Beam Position
Generator (BPG) in Fig. 12, has been fabricated which can
be used to load data into the input registers in a quasi-
parallel mode. For simplicity in the digital design of the
BPG, the MLM is considered to have 128 resolvable beam
positions. These 128 positions are defined as the unit
beam positions and are further divided into fractional
positions of $1/2$, $1/4$, and $1/8$. As shown in Fig. B-1, the
phase of all of the rows can be determined by adding the
appropriate offset to the phases of the first 8 rows. The
phase increment ($\Delta\varphi$) is a function of the desired beam
position. Using this technique to generate the phase slope,
the input register is loaded in 13 parallel groups. Each
group contains 8 voltage words (except for the last group
which contains 4) which are loaded sequentially into the
input registers. In this mode only 8 clock pulses are re-
quired to load the input registers instead of the 100 clock
pulses required in a purely sequential operation. The

- 97 -
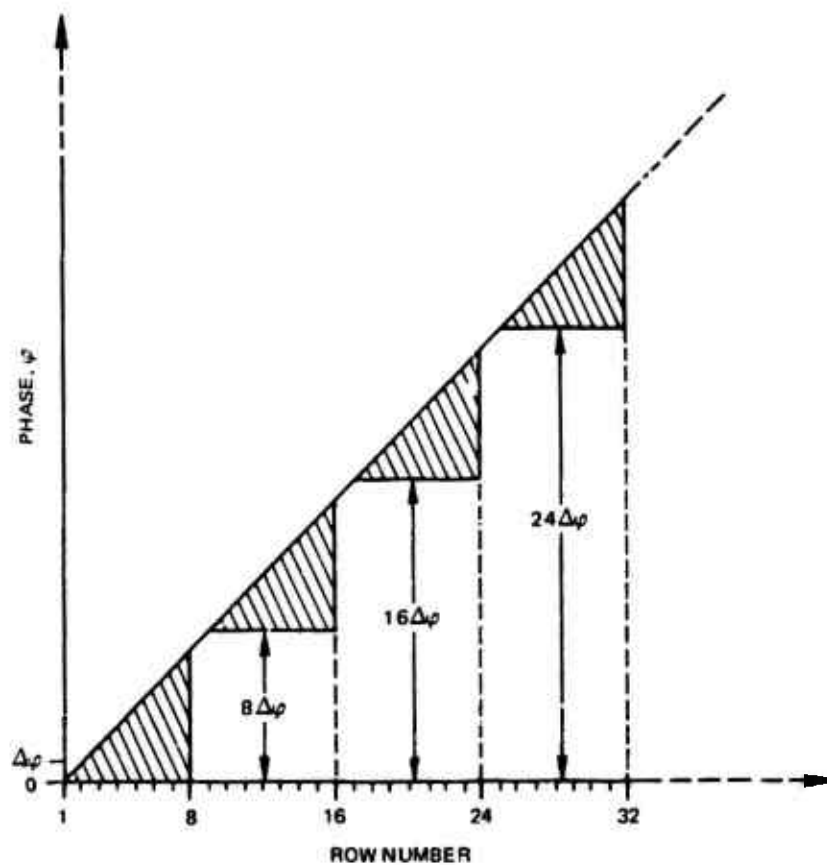
Fig. B-1   LINEAR PHASE SLOPE REQUIRED TO BEAM STEER
IN ONE DIMENSION WITH THE MLM

stepping time from one beam position to the next is limited by the digital logic to around $2\ \mu$s. The price for this speed capability is the requirement for 13 square root coders and 13 sets of output data from the BPG.

The BPG is useful for evaluating the MLM system without the need of the computer. It has several modes of operation:

1. <u>Free-Running</u>. The beam from the MLM is stepped continuously through all the beam positions in full or fractional steps. The stepping speed is controlled by means of the basic clock frequency.

2. <u>Selected Beam Position</u>. The simulator runs until it reaches a selected beam position and then stops. The desired beam position number is selected by means of toggle switches.

3. <u>Toggle Mode</u>. This is a high speed mode used to test the frequency response of the MLM which by-passes the $2\ \mu$s per step limitation in the free-running mode. The selected beam position is stored in the input register. The output register then rapidly alternates between this selected beam position and zero at each clock pulse.

4. <u>Noise and Offset Mode</u>. This mode allows digital noise (from an external source) or a uniform phase offset to be added sequentially to the simulator-generated phase words. In order to obtain noise that is independent row to row, the levels for each row must be determined sequentially. This requires 100 clock pulses which results in a low-speed operation.

MLM PROTECTION CIRCUITS

As described in Appendix A, when overvoltages are applied to the modulator elements, they bottom out. The

collodion membrane adheres to the SiO protective layer over the electrode structure. A voltage clamp circuit has been fabricated which prohibits the outputs from any of the MLM amplifiers from exceeding a certain threshold value (usually set just above the 2π phase voltage). Any excess current due to an amplifier failure or a turn-on or turn-off transient is drained off by this clamp circuit.

The modulator elements were also observed to bottom when exposed to relatively low voltages for a long period of time. A special circuit has been built to prevent a voltage from staying on an element for longer than 10 seconds. If a load pulse does not occur at the output register every 10 seconds or less, this circuit automatically resets the output registers to a zero level. This circuit works independent of the mode of operation of the electronics (i.e., computer, paper tape, etc.). A switch allows this circuit to be disconnected during the optical alignment procedure.

CRYSTAL BEAM-STEERING ELECTRONICS

The paper tape mode of the MLM electronics is used to beam steer with the crystal. As discussed in Section 5, a PL/I computer program has been written (for use on the IBM 360/91) which generates the voltages required to steer the beam of the crystal array. This program includes the offset phases required to compensate for the phase distortion across the crystal surface. The output of this program is punched on paper tape in a format which is compatible with the paper tape reader of the hybrid correlator. Since there are only 46 crystal elements, only the first 46 input and output registers of the hybrid correlator are used.

A potentiometer is used at the output of each of the MLM amplifiers in order to compensate for the different 2π phase voltages of the MLM (83 volts) and the

crystal (around 32 volts). The phase modulation sensitivity of the individual crystal elements is not exactly the same and therefore these potentiometers can also be used to adjust the outputs to the different 2π voltages of each element (which range from 30 to 33 volts).

SCANNING MIRROR READOUT SYSTEM

The readout system used to read the data from the output plane of the hybrid correlator is shown in Fig. B-2. The scanning mirror sweeps the area of interest in the readout plane across the face of a photomultiplier tube. Thus the current amplitude output of the photomultiplier as a function of time corresponds to the intensity of the light in the readout plane as a function of distance along the scan interval. The output from the photomultiplier is displayed on an oscilloscope.

A projection lens is used to focus the readout data plane via the scanning and fixed mirrors onto the slit in front of the photomultiplier tube. Due to the small size of the scanning mirror ($\frac{1}{4}$ by $\frac{1}{4}$ inch) it was necessary to use a short focal length projection lens. Since the image is many focal lengths away from the lens, the readout plane is approximately in the back focal plane of the projection lens. Therefore, in the front focal plane is the Fourier transform of the readout data plane (which is just a scaled image of the masked modulator). The size of this image is approximately the ratio of the focal lengths of the projection lens and the transform lens (f_2/f_1). The scanning mirror is placed in this plane. Since the image is smaller than the size of the mirror, all the orders that are passed through the projection lens can be scanned past the photomultiplier. The fixed mirror is used only as a matter of convenience to allow the photomultiplier to be mounted in an uncluttered location.

The scanner utilizes the model G-125 galvanometer scanning mirror driven by the AX-100 driver amplifier

- 101 -
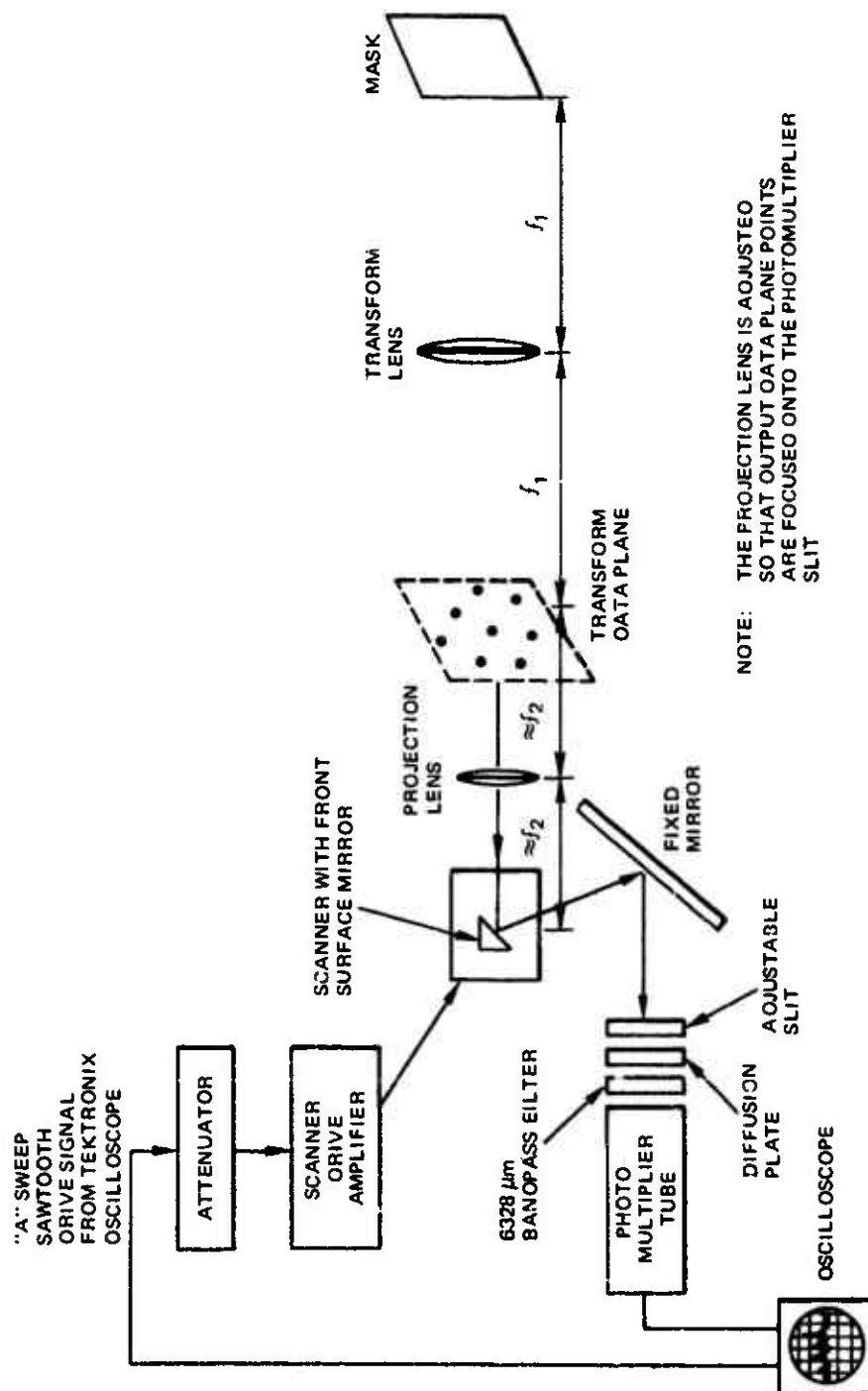
Fig. B-2   SCANNING MIRROR READOUT SYSTEM

manufactured by General Scanning, Inc. The galvanometer mirror can scan up to 10° maximum peak-to-peak deflection and has a resonant frequency of approximately 1400 Hz. A linear scan was obtained by using the sawtooth output from a Tektronix oscilloscope as a signal source for the driver amplifier. Scan frequencies as high as 100 Hz have been used.

APPENDIX C

ELECTRO-OPTIC PROPERTIES OF THE LITHIUM
TANTALATE MODULATOR

It has been shown by many authors (Refs 3, 7, and 8) that the relative optical impermeability tensor (and therefore the refractive index) of certain crystals is a function of the applied electric field. The impermeability tensor β_{ik} for a clamp crystal (clamping is necessary in order to eliminate the effect due to piezoelectricity and photoelasticity) can be described by the tensor equation:

$$\beta_{ik} = \beta_{ik}^{O} + r_{ikj}\, E_j + \rho_{ikjm}\, E_j\, E_m \qquad \text{(C-1)}$$

$$(i,\ j,\ k,\ m = 1,\ 2,\ 3)$$

where β_{ik}^{O} = tensor describing the relative impermeability for zero field,

E_j = tensor describing the applied electric field ($\vec{E}$),

r_{ikj} = tensor of rank three whose 27 components are the linear electro-optic coefficients ("Pockels" effect),

ρ_{ikjm} = tensor of rank four whose components are the quadratic electro-optic coefficients ("Kerr" effect).

By convention, $\hat{X}_3$ is chosen parallel to the $\hat{c}$ axis (optic axis), $\hat{X}_1$ is parallel to the $\hat{a}$ axis, and $\hat{X}_2$ is parallel to the $\hat{b}$ axis.

For small applied fields (such as those used in this experiment), the Kerr effect is negligible with respect

Preceding page blank

- 105 -

to the Pockels effect. The 27 components of the r_{ikj} tensor can be reduced to 18 by using symmetry arguments. The resulting equation is customarily written in the following manner:

$$
\begin{bmatrix}
\beta_{11} & - & \beta_1^o \\
\beta_{22} & - & \beta_2^o \\
\beta_{33} & - & \beta_3^o \\
 & \beta_{23} & \\
 & \beta_{31} & \\
 & \beta_{12} &
\end{bmatrix}
=
\begin{bmatrix}
r_{11} & r_{12} & r_{13} \\
r_{21} & r_{22} & r_{23} \\
r_{31} & r_{32} & r_{33} \\
r_{41} & r_{42} & r_{43} \\
r_{51} & r_{52} & r_{53} \\
r_{61} & r_{62} & r_{63}
\end{bmatrix}
\begin{bmatrix}
E_1 \\
E_2 \\
E_3
\end{bmatrix}
\qquad \text{(C-2)}
$$

where the electro-optic coefficients r_{ik} are now represented by a 3×6 matrix.

Since lithium tantalate is a trigonal crystal belonging to the 3m point group, it is optically uniaxial (when no field is present) and therefore $\beta_1^o = \beta_2^o$. Also, the r_{ik} matrix reduces to (Ref. 5):

$$
r_{ik} =
\begin{bmatrix}
0 & -r_{22} & r_{13} \\
0 & r_{22} & r_{13} \\
0 & 0 & r_{33} \\
0 & r_{51} & 0 \\
r_{51} & 0 & 0 \\
-r_{22} & 0 & 0
\end{bmatrix},
\qquad \text{(C-3)}
$$

where $r_{22} = -r_{12} = -r_{61}$; $r_{51} = r_{42}$; and $r_{13} = r_{23}$.

The impermeability matrix is found by substituting Eq. (C-3) into Eq. (C-2):

$$\beta = \begin{bmatrix} \beta_1^o - r_{22}E_2 + r_{13}E_3 & -r_{22}E_1 & r_{51}E_1 \\ -r_{22}E_1 & \beta_1^o + r_{22}E_2 + r_{13}E_3 & r_{51}E_2 \\ r_{51}E_1 & r_{51}E_2 & \beta_3^o + r_{33}E_3 \end{bmatrix} .$$

$$(C-4)$$

(U)   When the electric field is applied parallel to the $\hat{X}_3$ axis ($E_1 = E_2 = 0$), the impermeability matrix reduces to:

$$\beta_3' = \begin{bmatrix} \beta_1^o + r_{13}E_3 & 0 & 0 \\ 0 & \beta_1^o + r_{13}E_3 & 0 \\ 0 & 0 & \beta_3^o + r_{33}E_3 \end{bmatrix} .$$

$$(C-5)$$

The β ellipsoid ($\beta_{ij} X_i X_j = 1$) is described by:

$$(\beta_1^o + r_{13}E_3) X_1^2 + (\beta_1^o + r_{13}E_3) X_2^2$$
$$(C-6)$$
$$+ (\beta_3^o + r_{33}E_3) X_3^2 = 1 .$$

Notice that this is still in principle axis form which means that a field applied parallel to the $\hat{X}_3$ axis does not rotate the principle axes.   The effect of the field is to change the length of the axes.   Since the coefficients of the X_1^2 and X_2^2 terms are equal ($\beta_1^o + r_{13}E_3$), the crystal remains uniaxial.

For light polarized in the $\hat{X}_3$ direction and propagating in the X_2 direction, the phase modulation ($\Delta\varphi$) relative to a crystal of the same length but with zero applied field is:

- 107 -

$$_3\angle\varphi_3 = \frac{2\pi\, \ell_2}{\lambda}\ _3\Delta n_3 \quad , \tag{C-7}$$

where ℓ_2 = length of crystal in the $\hat{X}_3$ direction,

$_3\Delta n_3$ = change of index of refraction in the $\hat{X}_3$ direction due to the applied field (E_3)

$= n_3' - n_3,$

λ = wavelength of the illuminating beam.

The impermeability of a crystal is related to the index of refraction by

$$\beta = 1/n^2 \quad . \tag{C-8}$$

Therefore:

$$_3\Delta\beta_3 = {}_3\beta'_3 - {}_3\beta^0_3 = r_{33}E_3$$

$$= \frac{1}{(n_3')^2} - \frac{1}{(n_3)^2} \quad . \tag{C-9}$$

Rearranging Eq. (C-9) yields:

$$r_{33}E_3 = \frac{(n_3 - n_3')\,(n_3 + n_3')}{(n_3')^2\,(n_3)^2} \quad . \tag{C-10}$$

For $\dfrac{\Delta n}{n_3} \ll 1$, $n_3 \approx n_3'$ and Eq. (C-10) reduces to:

$$_3\Delta n_3 = \frac{-n_3^3\, r_{33}E_3}{2} \quad . \tag{C-11}$$

Substituting into Eq. (C-7) and letting $E_3 = V_3/\ell_3$, the phase modulation due to an applied field parallel to the $\hat{X}_3$ direction of light polarized parallel to the $\hat{X}_3$ direction and propagating in the $\hat{X}_2$ direction is:

$$_3\Delta\varphi_3 = \frac{-\pi\, \ell_2\, n_3^3\, r_{33}\, V_3}{\lambda \ell_3} \quad . \tag{C-12}$$

Similarly, for light polarized parallel to the $\hat{X}_1$ direction and propagating in the $\hat{X}_2$ direction, the phase modulation due to an applied field parallel to the $\hat{X}_3$ direction can be shown to be:

$$_1\Delta\varphi_3 = \frac{-\pi\, \ell_2\, n_1^3\, r_{13}\, V_3}{\lambda \ell_3} \quad . \tag{C-13}$$

The $\hat{X}_3$ and $\hat{X}_1$ directions represent the allowed directions of polarization in the crystal for light propagating in the $\hat{X}_2$ direction. When light is polarized at an angle with respect to these axes, the light (as far as the crystal is concerned) breaks up into $\hat{X}_3$ and $\hat{X}_1$ components. The phase modulation through the crystal for the $\hat{X}_3$ component is given by Eq. (C-12), and for the $\hat{X}_1$ component by Eq. (C-13). The relative phase difference between these components at the exit surface of the crystal is given by:

$$\Delta\varphi = {}_3\Delta\varphi_3 - {}_1\Delta\varphi_3$$

$$= \frac{-\pi\, \ell_2\, V_3}{\lambda \ell_3} \left(r_{33} n_3^3 - r_{13} n_1^3 \right) . \tag{C-14}$$

This, in general, results in an elliptically polarized beam.

APPENDIX D

OPTICAL PHASED ARRAY TRANSFORM PATTERNS

The equations describing the Fourier transform patterns of optical phased arrays will be discussed tutorially in this appendix. The reader is directed to Ref. 9 for a description of the Fourier transform properties of a lens and to Ref. 10 for a discussion of optical diffraction theory.

When an object is placed in the front focal plane or (X, Y) space of a perfect lens, its spatial Fourier transform exists in the back focal plane or (ξ, η) space and is described by the following equation (Ref. 9):

$$U(\xi, \eta) = \int_{-\infty}^{+\infty} \int_{-\infty}^{+\infty} U(X, Y) \exp[-j \frac{2\pi}{\lambda f} (X\xi + Y\eta)] \, dx \, dy , \quad \text{(D-1)}$$

where $U(X, Y)$ = the complex light distribution in the input plane,

$U(\xi, \eta)$ = the complex light distribution in the transform plane,

λ = the wavelength of the coherent illumination, and

f = the focal length of the lens.

Typically the input function is described by an amplitude term, $A(X, Y)$, and a phase term, $\exp[j\varphi(X, Y)]$, such that:

$$U(X, Y) = A(X, Y) \exp[j\varphi(X, Y)] . \quad \text{(D-2)}$$

Consider first a linear array of coherent isotropic light sources which are equally spaced along the X axis (as shown in Fig. 8). Equation D-1 reduces to one dimension and can be written in the series form:

$$U_a(\xi, \eta) = \sum_{m=1}^{M} A_m \exp(j\varphi_m) \exp\left[-j \frac{2\pi}{\lambda f} \left(m - \frac{M+1}{2}\right) \Delta X \xi\right], \quad \text{(D-3)}$$

where M = the number of point radiators,

A_m = the amplitude of the mth radiator,

φ_m = the relative phase of the mth radiator, and

ΔX = the center spacing of the elements.

When the radiators are of the same amplitude and phase (i.e., $A_m = A$ and $\varphi_m = 0$), Eq. (D-3) reduces to:

$$U_a(\xi) = \sum_{m=1}^{M} A \exp\left[-j \frac{2\pi}{\lambda f} \left(m - \frac{M+1}{2}\right) \Delta X \xi\right]. \quad \text{(D-4)}$$

Equation (D-4) can be rearranged into the form:

$$U_a(\xi) = A \exp\left[+j \frac{\pi}{\lambda f} (M+1) \Delta X \xi\right] \left[\sum_{m=0}^{M} Z^m - 1\right], \quad \text{(D-5)}$$

where:

$$Z = \exp\left[-j \frac{2\pi}{\lambda f} (\Delta X \xi)\right]. \quad \text{(D-6)}$$

The sum in the right-hand brackets of Eq. (D-5) is in the form of a geometric series whose solution is given by:

$$\sum_{m=0}^{M} Z^m = \frac{1 - Z^{M+1}}{1 - Z}. \quad \text{(D-7)}$$

Substituting Eqs. (D-6) and (D-7) into (D-5) yields:

$$U_a(\xi) = A \left[\frac{\exp[j(M\pi \Delta X \xi)/\lambda f] - \exp[-j(M\pi \Delta X \xi)/\lambda f]}{\exp(j\pi \Delta X \xi/\lambda f) - \exp(-j\pi \Delta X \xi/\lambda f)}\right]. \quad \text{(D-8)}$$

Using Euler's equation, the equation describing
the transform pattern due to a one-dimensional array of
isotropic radiators is

$$U_a(\xi) = A \frac{\sin [(M\pi \Delta X \xi)/\lambda f]}{\sin [(\pi \Delta X \xi)/\lambda f]} \quad . \tag{D-9}$$

The power in the transform plane can be found
from Eq. (D-9):

$$P_a(\xi) = |U_a(\xi)|^2 = U_a(\xi) \, U_a^*(\xi)$$

$$= A^2 \frac{\sin^2 [(M\pi \Delta X \xi)/\lambda f]}{\sin^2 [(\pi \Delta X \xi)/\lambda f]} \quad . \tag{D-10}$$

This equation describes a one-dimensional array
of grating lobes which occur whenever both the numerator
and denominator of this equation go to zero simultaneously.
This occurs whenever:

$$\frac{\pi \Delta X \xi_p}{\lambda f} = K\pi \, , \tag{D-11}$$

where K = 0, ± 1, ± 2, ... Rearranging this equation,
the location of the grating lobes is described by:

$$\xi_p = \frac{K\lambda f}{\Delta X} \quad . \tag{D-12}$$

The relative power at the peaks can be found by substitut-
ing Eq. (D-12) into (D-10):

$$P_a(\xi_p) = M^2 A^2 \, . \tag{D-13}$$

The first null of Eq. (D-10) occurs at:

$$(M\pi \Delta X \xi)/\lambda f = \pi \, , \tag{D-14}$$

and therefore the width of the grating lobes (from the peak to the first null) is:

$$\Delta\xi = \frac{\lambda f}{M\Delta X} \ .$$

(D-15)

There are M - 1 equally spaced nulls between the grating lobes, occurring whenever:

$$(M\pi\Delta X\xi)/\lambda f = n\pi$$

(D-16)

where $n = \pm 1, \pm 2, \ldots, M-1$; therefore, there are M - 2 sidelobes between the grating lobes.

The peaks in the transform pattern can be steered along the ξ axis by applying a linear phase slope across the array. For a linear phase slope of p cycles across the array, the phase of the mth element is defined by:

$$\varphi_m = \frac{2\pi m}{M} \ p \ .$$

(D-17)

Inserting this into Eq. (D-3), the transform pattern of the array is now described by:

$$U_a(\xi,\eta) = A \sum_{m=1}^{M} \exp(j\ \frac{2\pi mp}{M}) \exp[-j\ \frac{2\pi}{\lambda f} (m - \frac{M+1}{2})\Delta X\xi] \ .$$

(D-18)

Using a similar analysis as given above, Eq. (D-18) reduces to:

$$U_a(\xi) = A\ \frac{\sin\ [(M\pi\Delta X\xi)/\lambda f - \pi p]}{\sin\ [(\pi\Delta X\xi)/\lambda f - \pi p/M]} \ .$$

(D-19)

This equation has a peak whenever:

$$\xi = (K + \frac{p}{M})\ \frac{\lambda f}{\Delta X} \ ,$$

(D-20)

where $K = 0, \pm 1, \pm 2, \ldots$

- 114 -

This pattern has the same shape as Eq. (D-9) except that now the peaks are shifted along the ξ axis by $p(\frac{\lambda f}{M\Delta X})$. Therefore, the location of the peaks on the ξ axis is proportional to the phase slope across the array.

Using the Rayleigh resolution criteria (that the peak of one beam be in the null of an adjacent beam), it can be shown from Eqs. (D-15) and (D-12) that there are M resolvable beam positions between the ambiguities.

When the input function is a two-dimensional orthogonal periodic array of isotropic radiators (as shown in Fig. 10), Eq. (D-1) can be written in the series form (ignoring a constand phase term):

$$U_a(\xi, \eta) = \sum_{n=1}^{N} \sum_{m=1}^{M} A(m, n) \exp[j\varphi(m, n)] \exp[-j\frac{2\pi}{\lambda f}(m\Delta X\xi + n\Delta Y\eta)] ,$$

$$(D-21)$$

where M = the number of radiators in the X direction,

N = the number of radiators in the Y direction,

ΔX = the spacing of the radiators in the X direction, and

ΔY = the spacing of the radiators in the Y direction.

Using a method similar to that used to obtain Eq. (D-9) from Eq. (D-3), the pattern in the transform plane for this two-dimensional array is found to be

$$U_a(\xi, \eta) = A \left[\frac{\sin[(M\pi\Delta X\xi)/\lambda f]}{\sin[(\pi\Delta X\xi)/\lambda f]} \right] \left[\frac{\sin[(N\pi\Delta Y\eta)/\lambda f]}{\sin[(\pi\Delta Y\eta)/\lambda f]} \right] \quad (D-22)$$

This equation describes a two-dimensional orthogonal periodic array of grating lobes whose peaks occur whenever:

$$\xi = \frac{K\lambda f}{\Delta X} \quad \text{and}$$

$$\eta = \frac{L\lambda f}{\Delta Y} \; , \tag{D-23}$$

where $K = 0, \pm 1, \pm 2, \ldots ,$ and

$L = 0, \pm 1, \pm 2, \ldots .$

The widths of these grating lobes in the ξ and η directions are:

$$\Delta \xi = \frac{\lambda f}{M \Delta X} \quad \text{and}$$

$$\Delta \eta = \frac{\lambda f}{N \Delta Y} \; . \tag{D-24}$$

The relative power of the peaks is proportional to $M^2 N^2 A^2$.

The peaks in the transform pattern can be steered in two dimensions by applying a two-dimensional phase slope across the array. Consider the following two-dimensional phase slope where the phase of the (m, n) element is described by:

$$\varphi_{mn} = \left(\frac{2\pi m}{M} \right) p + \left(\frac{2\pi n}{N} \right) q \; . \tag{D-25}$$

The plane of constant phase is tilted such that there are p complete cycles of phase across the array in the X direction and q complete cycles of phase across the array in the Y direction. Substituting Eq. (D-25) into Eq. (D-21), and assuming $A(m, n) = A$:

$$U_a(\xi, \eta) = A \sum_{n=1}^{N} \sum_{m=1}^{M} \exp[j \, 2\pi(\frac{mp}{M} + \frac{nq}{N})] \exp[-j \frac{2\pi}{\lambda f} (m\Delta X \xi + n\Delta Y \eta)] \; . \tag{D-26}$$

Again using the same analysis as before, the pattern in the transform plane is described by:

$$U_a(\xi,\eta) = A \left[\frac{\sin\left[(M\pi\Delta X\xi)/\lambda f - \pi p\right]}{\sin\left[(\pi\Delta X\xi)/\lambda f - \pi p/M\right]} \right]\left[\frac{\sin\left[(N\pi\Delta Y\eta)/\lambda f - \pi q\right]}{\sin\left[(\pi\Delta Y\eta)/\lambda f - \pi q/N\right]} \right] \quad (D-27)$$

This equation is similar to Eq. (D-22) except that the peaks are shifted along the ξ axis by $p(\lambda f/M\Delta X)$, and along the η axis by $q(\lambda f/N\Delta Y)$. Thus the position of the grating lobes is a function of the two-dimensional phase slope across the array.

Again using the Rayleigh resolution criteria, Eqs. (D-23) and (D-24) can be used to show that there are M resolvable beam positions between the grating lobes in the ξ direction and N resolvable beam positions in the η direction for a total of M x N grating lobes in the two-dimensional area between the grating lobes.

So far the discussion has been limited to arrays of isotropic radiators. In actuality, most radiators are directional and therefore the equations described so far must be modified by the "antenna pattern" of the individual radiators. When the radiators have identical transform patterns, the transform pattern for the array is described by the equation:

$$U(\xi,\eta) = U_e(\xi,\eta)\, U_a(\xi,\eta)\,, \quad (D-28)$$

where $U(\xi,\eta)$ = the transform pattern for an array of nonisotropic radiators,

$U_a(\xi,\eta)$ = the transform pattern of the array when isotropic radiators are assumed, and

$U_e(\xi,\eta)$ = the transform pattern of the individual radiator elements.

When 0 volts is applied to the masked Membrane Light Modulator elements, the elements appear as uniformly illuminated circular apertures. As shown in Ref. 10, the transform pattern of a uniformly illuminated circular aperture is the familiar Airy disk which is described by the Bessel function:

$$U_e(\rho,\varphi) = \frac{1}{2\pi} \left[\frac{J_1(\frac{2\pi\rho R}{\lambda f})}{(\frac{2\pi\rho R}{\lambda f})} \right] \qquad (D-29)$$

where R = the radius of the mask apertures (20 μm), and

$$\rho = \frac{2\pi}{\lambda f} (\xi^2 + \eta^2)^{\frac{1}{2}} .$$

The first zero of this element pattern occurs at

$$\frac{2\pi\rho R}{\lambda f} = 1.22\pi , \text{ or}$$

$$\rho = \frac{0.61\lambda f}{R} . \qquad (D-30)$$

The transform pattern of the MLM array is found by substituting Eqs. (D-29) and (D-22) into Eq. (D-28) (remembering that for the MLM, $\Delta X = \Delta Y$ and $M = N$):

$$U(\xi,\eta) = C \left[\frac{J_1(\frac{2\pi\rho R}{\lambda f})}{(\frac{2\pi\rho R}{\lambda f})} \right] \left[\frac{\sin[(M\pi\Delta X\xi)/\lambda f]}{\sin[(\pi\Delta X\xi)/\lambda f]} \right] \left[\frac{\sin[(M\pi\Delta X\eta)/\lambda f]}{\sin[(\pi\Delta X\eta)/\lambda f]} \right] \qquad (D-31)$$

From Eq. (D-30) and (D-23), it can be shown that along the ξ axis there are seven grating lobes under the main lobe of the element pattern.

When voltages are applied to the modulator elements, they deflect as paraboloids. The circular mask apertures are now considered to be illuminated by a parabolic wavefront. The phase across the elements is circularly symmetric and is described by (Eq. 1, Section 2):

$$\varphi(r) = \varphi_0 [1 - (\frac{r}{R_0})^2] ,$$

where φ_0 = the peak phase at $r = 0$, and

R_0 = the radius of the modulator elements.

The transform pattern for the masked modulator elements is now described by

$$U_e(\rho) = \int_0^R \int_0^{2\pi} \exp\left(-j\varphi_0 [1 - (\frac{r}{R_0})^2]\right) \exp(-j \frac{2\pi}{\lambda f} \rho r \sin \theta) \, r \, dr \, d\theta . \quad \text{(D-32)}$$

Equation (D-32) can be reduced to:

$$U_e(\rho) = \frac{1}{2\pi} \exp(-j\varphi_0) \int_0^R \exp[+j\varphi_0 (\frac{r}{R_0})^2] \, J_0(\frac{2\pi\rho r}{\lambda f}) \, r \, dr . \quad \text{(D-33)}$$

This equation has not been solved in closed form. However, the theoretical variation of intensity at boresight ($\rho = 0$) as a function of the peak phase can be determined. The light amplitude on boresight is given by:

$$U_e(0) = \frac{1}{2\pi} \exp(-j\varphi_0) \int_0^R \exp[+j\varphi_0 (\frac{r}{R_0})^2] \, r \, dr$$

$$= \frac{1}{2\pi} [\exp(-j\varphi_0)] \left(\frac{jR_0^2}{\varphi_0}\right) \left(\exp[j\varphi_0 (\frac{R}{R_0})^2] - 1\right) . \quad \text{(D-34)}$$

From Eq. (D-34), the power at boresight can be shown to be:

$$P(0) = U(0) U^{*}(0)$$

$$= C \left[\frac{\pi R_o^2}{\varphi_o}\right]^2 [1 - \cos \varphi_o \left(\frac{R}{R_o}\right)^2]$$ (D-35)

Equation (D-35) is plotted in Fig. 18 for $R_o = 50 \, \mu m$ and $R = 20 \, \mu m$.

The multi-channel crystal phase modulator can be considered as a linear array of rectangular apertures. As shown in Ref. 10, the transform pattern of a uniformly illuminated rectangular aperture is described by:

$$U_e(\xi, \eta) = ab \left[\frac{\sin\left(\frac{\pi a \xi}{\lambda f}\right)}{\left(\frac{\pi a \xi}{\lambda f}\right)}\right] \left[\frac{\sin\left(\frac{\pi b \eta}{\lambda f}\right)}{\left(\frac{\pi b \eta}{\lambda f}\right)}\right],$$ (D-36)

where a = the width of the rectangular aperture parallel to the X axis, and

b = the width parallel to the Y axis.

Substituting Eqs. (D-36) and (D-9) into Eq. (D-28), the transform pattern for the crystal is described by:

$$U(\xi, \eta) = Aab \left[\frac{\sin(\pi a \xi/\lambda f)}{(\pi a \xi/\lambda f)}\right] \left[\frac{\sin(\pi b \eta/\lambda f)}{(\pi b \eta/\lambda f)}\right] \left[\frac{\sin(M\pi \Delta X \xi/\lambda f)}{\sin(\pi \Delta X \xi/\lambda f)}\right].$$ (D-37)

For the present crystal mask, $a = b = \Delta X/5$. From Eq. (D-37) it can be shown that along the ξ axis there are nine grating lobes under the main lobe of the element pattern.

APPENDIX E

THE EFFECT OF A SMALL MAGNIFICATION CHANGE ON THE FOCUS POSITION FOR A LENS NEAR UNITY MAGNIFICATION

It will be shown in this appendix that the total object plus image distance for a lens can be considered constant when the lens is used near unity magnification. The procedure required for aligning the transmit mask and imaging lens is greatly simplified by this fact because once the image is approximately at unity magnification, the transmit mask no longer has to be moved (along the optical axis) and the exact magnification can be obtained by moving just the imaging lens.

The simple lens equation is:

$$\frac{1}{f} = \frac{1}{p} + \frac{1}{q} , \qquad (E-1)$$

where p = object distance,

q = image distance, and

f = focal length.

If we let the object plus image distance equal S, and the magnification equal m:

$$S = p + q , \qquad (E-2)$$

$$m = q/p . \qquad (E-3)$$

Inserting Eqs. (E-2) and (E-3) into Eq. (E-1) and rearranging yields:

$$S = f\frac{(m+1)^2}{m} . \qquad (E-4)$$

The minimum of this function can be determined by setting $dS/dm = 0$ and is found to occur at $m = 1$. Since the slope is zero at this point, the value of S around this point is fairly constant for small changes of m. Therefore small changes in the magnification around unity magnification can be made without a change in the image-plus-object distance.

The range of magnification over which this approximation is valid for the MLM system is calculated as follows. Assume that a change in the magnification of Δm results in a change of the object plus image distance of ΔS (and vice versa). Equation (E-4) becomes:

$$(S + \Delta S) = \frac{f(m+\Delta m+1)^2}{m+\Delta m}$$

$$= f(m+\Delta m + 2 + \frac{1}{m+\Delta m})$$

$$\approx f(m+\Delta m + 2 + m-\Delta m + \Delta m^2)$$

$$\approx f(2m+2 + \Delta m^2).$$

At $m = 1$, $S = 4f$, so that:

$$4f + \Delta S \approx f(4 + \Delta m^2), \text{ or}$$

$$\Delta S \approx f\Delta m^2 \tag{E-5}$$

The depth of focus for a diffraction limited lens in a coherent system when the image is in the focal plane, is given as (Ref. 10):

$$\Delta S \approx \pm 2 \left(\frac{f}{d}\right)^2 \lambda.$$

For the MLM, the image is at $2f$ and this changes to

$$\Delta S \approx \pm 8 \left(\frac{f}{d}\right)^2 \lambda. \tag{E-6}$$

Since the f number of the imaging lens is $f/4.8$, and the illuminating wavelength is $\lambda = 6328$ Å, Eq. (E-6) becomes:

$$\Delta S \approx 0.12 \text{ mm} .$$

Therefore, the percentage change in magnification that can be made without going out of focus is (from Eq. (E-5) with $f = 150$ mm):

$$\Delta m^2 = \frac{0.12 \text{ mm}}{150 \text{ mm}} = 8 \times 10^{-4}$$

$$\Delta m \approx \pm 0.03$$

or $\quad \Delta m \approx 3\%$.

In practice, it was found that when the image was within approximately 1% of the correct magnification, the transmit mask position remained constant.

APPENDIX F

SELECTION OF THE ELEMENT LOCATIONS FOR THE THINNED MLM ARRAYS

Since the elements along each row of the MLM array are controlled by a single electrode, the phase of each of these elements is the same. Phase slopes parallel to the electrode structure are required in order to perform two-dimensional beam steering, and therefore only one element from each row can be used. A mask is used to block the light from all but the appropriate element.

The criteria to be used for selecting the location of the elements in the thinned array are:

1. The resolution in the transform pattern of the entire 100 x 100 array should be maintained.

2. The sidelobe levels in the transform pattern should be as low as possible.

If independent access could be made to each element in the 100 x 100 array, the beam could be steered into 10 000 resolvable positions (in a 100 x 100 array) using the Rayleigh resolution criteria which requires that the peak of one beam occur in the null of an adjacent beam. When the locations of the thinned array elements are chosen judiciously, this resolution of the whole array is maintained. When only 100 elements are used, there will not necessarily be distinct nulls associated with the main lobe and therefore some other resolution criteria is required. The intensity at the crossing point for two adjacent Rayleigh beam positions is approximately 4 dB down from the intensity at the peak, and therefore, a 4-dB beamwidth will be used as the "Rayleigh" resolution criteria for the thinned array.

Preceding page blank   - 125 -

In order to simplify the following discussion, the
nomenclature shown in Fig. 10 will be used. For the MLM
array, Y corresponds to the direction parallel to the elec-
trode structure (and therefore X is perpendicular to elec-
trodes). Also, M = N = 100 and $\Delta X = \Delta Y = 50~\mu m$. In the
transform plane, ξ is the direction for one-dimensional
beam steering using the whole 100 x 100 MLM array. For
simplicity, isotropic radiators will be assumed.

In order to avoid the observation of false beam posi-
tions, it is necessary to minimize the peak power in lobes
other than the main grating lobes. The minimum sidelobe
level that can be achieved is limited by the requirement
that only one element occur on each electrode. The trans-
form pattern along the ξ axis is described by a $(\sin \xi)/\xi$ dis-
tribution in the vicinity of the main grating lobe. The peak
intensity of the first sidelobe for this distribution is 13 dB
down from the peak intensity of the main lobe. The goal
therefore is to keep the peak intensity at any other point
in the area between the grating lobes below this -13 dB
level.

So far, no restriction has been made on the loca-
tion of the elements in the Y direction. Let's consider
what would happen if the Y location for each row were
the same. This results in just a linear array in the X
direction. The resolution of the 100 x 100 array is main-
tained in the ξ direction but there is no resolution in the
η direction. In order to maintain the resolution of the
whole array, the width of the lobe along the η axis
should be the same as along the ξ axis. If the require-
ment is imposed that every column contain one element
(as well as every row), then the transform pattern (in the
vicinity of the main lobe) along the η axis is a $(\sin \eta)/\eta$
distribution (same as along the ξ axis) and therefore
the width of the main grating lobe along the ξ and η
axes satisfy the resolution criteria. This does not mean
however that the resolution of the array is necessarily
maintained in all directions. A good example of this is

the case where the 100 elements are chosen along the diagonal of the 100 x 100 array (which again reduces to a linear array). The width of the lobe along the ξ and η axes is correct, but there is no resolution along the $\xi = \eta$ line and therefore there are only 100 resolvable positions (in the direction of the line $\xi = -\eta$).

Probably the simplest arrangement of the thinned array elements would be a set of straight lines. The transform pattern of the thinned array can be determined by multiplying the transform patterns of these straight lines (or linear arrays). It can be shown that for linear slopes at the input, the power between the grating lobes is concentrated in line patterns (the line patterns of the linear arrays). Thus, it is difficult to obtain low sidelobes using straight line patterns. In order to obtain low peak sidelobes, it is necessary to spread this power as uniformly as possible over the areas between the grating lobes.

A "random" orientation of the elements is required in order to obtain this "thumbtack" response. In choosing a pseudo-random orientation for the 100 elements, the elements are still restricted to one element for each row and column in order to maintain the resolution along the ξ and η axes.

A computer program has been written that calculates the power at any point in the transform pattern for a thinned two-dimensional array. Since the power in the transform plane is symmetrical about the origin, the power is computed over only half the unambiguous transform area. The number of points at which a calculation should be made is a function of the highest spatial frequency component (or smallest sidelobe width) that is expected in the transform pattern. It can be shown that a total of 80 000 points satisfy the Nyquist sampling criteria.

The computer program itself can be used to perform some of the analysis of the transform pattern.

Threshold levels can be set on the output data. A plot of
the power in the tra..sform plane can be obtained. (A one-
digit code corresponding to the relative power is printed
at each sample point which crosses the threshold level.)
The (ξ, η) coordinates of the sample points which cross
the threshold and the relative power at the points can also
be printed on a separate sheet.

The amount of computer time required to calculate
the power at the 80 000 sample points (using the IBM 360/
91) is approximately 3 minutes (a cost of around $50).
The threshold level determines the number of points to be
plotted. An additional 2 minutes of computer time and
1 hour of plotting time is required for a typical plot with
the threshold set at -15 dB, resulting in a total cost of
around $90. Although the computer plot represented an
ideal method for displaying the data, only a few were
made because of the high cost. Since the peak sidelobes
were typically around -10 dB, the threshold was set at
around -11 dB and the (ξ, η) coordinates and power of the
points which crossed the threshold were printed out.
These points (typically 10 to 20 points) were then plotted
by hand.

Several pseudo-random input patterns have been
generated. For each of these input patterns, the power
in the transform plane was calculated. The best of these
patterns still had several sidelobes which were only 10
dB down from the main grating lobes.

A limited effort was made to "optimize" the loca-
tions in the input plane in order to eliminate the high lobes
in the transform patterns. A high sidelobe in the 2-D
transform plane is an indication that a particular spatial
frequency in a given direction has a predominate compo-
nent in the input pattern. The particular frequency and
direction can be determined from the (ξ, η) coordinates
of the lobe. When the input plane was inspected, a pre-
dominance of this frequency was observed. The locations

of the elements in the input pattern were adjusted in order
to reduce the predominance of this frequency. Typically,
this resulted in the position change of around 10 elements.
The transform pattern for this new input pattern was then
computed. As expected, the original lobe was always
eliminated. However, each time this was tried, several
new sidelobes would pop up. This "optimization" proce-
dure was attempted on three different patterns and each
time the original pattern had fewer high sidelobes.